THEORY OF ELECTRON TRANSPORT THROUGH SINGLE MOLECULES

Alaa Ahmed Dihe AL-Jobory

PhD Thesis in Nanoelectronics

Department of Physics, Lancaster University, UK

This Thesis is submitted in partial fulfilment of the requirements for degree of Doctor of Philosophy

September 2017

Declaration

I hereby declare that the thesis is my own work and effort and has not been submitted in substantially the same form for the award of a higher degree elsewhere. Other sources of information have been used, they have been acknowledged. This thesis documents work carried out between February 2014 and September 2017 at Lancaster University, UK, under the supervision of Prof. Colin J. Lambert and funded by Ministry of Higher Education and Scientific Research of Iraq in partnership with University of Anbar, Iraq.

Alaa A. Al-Jobory
2017

TO MY PARENTS, MY FAMILY, MY BROTHERS AND MY SISTERS

Abstract

The theoretical work carried out in this thesis presents the electrical properties of two different types of two terminal nanojunctions: one dealing with gold electrodes which form gold|molecule|gold structures and the other has carbon nanotube (CNT) electrodes forming CNT|molecule|CNT junctions. The theoretical tools employed are firstly, density functional theory (DFT). Chapter 2 presents an introduction to the theoretical concept of DFT and in this work the implemented version used, namely the SIESTA code. The second tool is the quantum transport code GOLLUM. To introduce this technique in Chapter 3, I present solutions of Green's functions for infinite and semi-infinite chains and the transmission coefficient equation which forms the theoretical basis of this code.

The first topic I investigate is quantum interference based connectivity dependence in a series of molecular wires. Two isomeric series have been obtained with 4-ethynylpyridine units linked to the core either at *para-para* positions or *meta-meta* positions. A combined experimental and computational study is described, in which my work provides the theoretical understanding of the experiment. The conductance of these molecules is measured using a mechanically controlled break junction and density functional theory calculations, demonstrates consistently higher conductance in the *para* series compared to the *meta* series: this is in agreement with increased conjugation of the π–system in the *para* series. Within the *para* series conductance increases in the order of decreasing heteroaromaticity (dibenzothiophene < carbazole < dibenzofuran). However, the sequence is very different in the *meta* series, where dibenzothiophene ≈ dibenzofuran < carbazole. Excellent agreement between theoretical and experimental conductance values is obtained. This study is presented in chapter 4 and establishes that

both quantum interference and heteroaromaticity in the molecular core units play important and inter-related roles in determining the conductance of single molecular junction.

Secondly, the electrical properties (band structure, open channel and transmission coefficient) was studied for different types of carbon nanotubes which act as electrodes, and two asymmetric molecules attached to the carbon nanotubes to form a nanojunction. There are two strategies used in this study: first the established DFT method and the second a parametrized tight binding approach. A four-orbital tight binding model (sp3) is used to construct the Hamiltonian and using Gollum to calculate transmission coefficients I find very good agreement with the transmission coefficient calculated by a DFT Hamiltonian. However, the tight binding approach is limited to carbon atoms only, at least in this work but it offers a more efficient calculation method and opens up the possibility to study the how different orbitals control transport and quantum interference. Also in chapter 5 using the DFT method, I compute the transmission coefficient and then IV curves to investigate rectification.

In the chapter 6, I present a theoretical study of the conductance perpendicular to the plane of a series of polycyclic aromatic hydrocarbons. The smaller members of the oligoacenes up to and including anthracene are found to be insulators or semi-conductors but those with eighteen carbon atoms (tetracene) and over are found to be conductors which is in stark contrast to previous calculation of in- plane conductance and experiment which generally predict them to be insulators or semiconductors. The number of open conductance channels increases as the number of aromatic rings increases for the variants studied and these trends are found to persist for more complex geometries. Features in the electrical conductance around the Fermi energy suggest possible candidates for future thermoelectric devices.

Acknowledgements

I would like to express the deepest appreciation to my supervisor, Professor Colin J. Lambert, who has the attitude and the substance of a genius he continually and convincingly adds a special flavor and spirit of adventure in regard to research by intensive fruitful discussion and excitement in regard to teaching over these years. I would like to thank my co-supervisor Dr. Iain Grace and Dr. Steve Bailey, Dr. Hatef Sadeghi, Dr. Sara and Dr. David for their encouraged me and continues support.

I would like also to thank my sponsor, the Ministry of Higher Education of Iraq and my University in Iraq Anbar University, for given me this great opportunity to study a Ph.D. in the United Kingdom.

I would like to thank the collaborating experimental groups of Department of Chemistry, Markus Gantenbein, Professor Martin R. Bryce in the Durham University, for their successful experiments. I would like to thank all my friends and colleagues in Colin’s group, especially Ali, Zain, Mohammed and Mohsin.

Last but not the least, I would like to thank my family: my father, my brothers and sisters and not forget to thank my wife and my kids.

List of publication during my PhD study

1- Ismael, A. K., **Al-Jobory, A.,** Grace, I., & Lambert, C. J. (2017). Discriminating single-molecule sensing by crown-ether-based molecular junctions. The Journal of Chemical Physics, 146(6), 064704.

2- Gantenbein, M., Wang, L., **Al-jobory, A. A.,** Ismael, A. K., Lambert, C. J., Hong, W., & Bryce, M. R. (2017). Quantum interference and heteroaromaticity of para- and meta-linked bridged biphenyl units in single molecular conductance measurements. Scientific Reports, 7.

3- Modelling crown Ether molecular wires from experiment (to be submitted)

4- Carbon Nanotube based single molecule devices (to be submitted)

5- A comprehensive study of the electrical conductivity through flat stacked polycyclic aromatic hydrocarbons. (to be submitted)

6- Thermopower in endohedral fullerenes - Sc3C2@C82

Contents

Introduction..10

1.1. Molecular electronics 10

1.2 Thesis Outline 12

Reference 13

Chapter 2 18

2. Density Functional Theory 18

2.1 Introduction 18

2.2 The Schrödinger Equation and Variational Principle 19

2.3 The Hohenberg-Kohn Theorems 22

2.4 The Kohn-Sham Theorems 24

2.5 The Exchange Correlation Functionals 25

2.5.1 Local Density Approximation 26

2.5.2 Generalized Gradient Approximation 26

2.6 Pseudopotentials 27

2.7 Basis Sets 28

References...31

Chapter 3 35

3. Single Particle Transport 35

3.1 The Landauer Formula 36

3.2 One-Dimension...39

3.2.1 Perfect One-Dimensional Lattice 39

3.2.2 One-Dimensional Scattering 42

3.3 Generalization of the Scattering Formalism.................................47

3.3.1 Hamiltonian and Green's Function of the Leads 47

Reference 57

Chapter 4 59

4.1 Quantum interference and heteroaromaticity of para- and meta-linked bridged biphenyl units in single molecular conductance measurements .59

4.2 Introduction...59

4.3 Results 64
4.4 Theory and Simulations...73
4.5 Binding Energy...74
4.6 Discussion..88
4.7 Analytical formula *G* of fluorene core 89

4.9 Conclusion 93

References...94

Chapter 5...99

Carbon Nanotube based single molecule devices 99
5.1 introduction...99
5.2 Carbon Nanotube 99

5.2.1 Chirality a concept to describe nanotubes.......................100
5.2.2 The CNT lattice 101
5.2.3 The Tight Binding Model...104
5.3 Numerical simulations..107

5.3.1 Four orbital tight binding calculation................................107
5.3.2 DFT calculations 113
5.4 Calculation of Electronic Properties.....................................114

5.4.1 CNT (n, m) 114
5.4.2 Binding Energy..116
5.4.3 Transmission coefficient 121
5.4.4 Current rectification..124
5.4.6 Conclusions 132
References 133
Chapter 6...136

A comprehensive study of the electrical conductivity through flat stacked polycyclic aromatic hydrocarbons..136

6.1 Introduction 136
6.2 Computational Details 138
6.3 Result 140
6.3.1 Number of open transmission channels 140
6.3.2 Band Structure 145
6.3.3 Eigenvalues..148
6.4 Analytical formula 153

Conclusion 154

References..155

Chapter 7..157

7.1 Conclusion 157

7.2 Future Work..159

References..160

Chapter 1

Introduction

1.1. Molecular electronics

The idea of using single molecules as building blocks to design and fabricate molecular electronic components has been around for more than 40 years [1], but only recently it has attracted huge scientific interest to explore their unique properties and opportunities. Molecular electronics including self-assembled monolayers [2] and single-molecule junctions [3] are of interest not only for their potential to deliver logic gates [4-5], sensors[6-7], and memories [8] with ultralow power requirements and sub-10-nm device footprints, but also for their ability to probe room-temperature quantum properties at a molecular scale such as quantum interference [9] and thermoelectricity [10,11]. Single molecular electronics has gained intensive attention since the first molecular rectifier was proposed by Aviram and Ratner in 1974.[12] By manipulating their chemical structure, a diverse range of molecules have been investigated, which function as basic electronic elementary devices, such as rectifiers,[13–16] conducting wires,[17–21] and negative differential resistance devices,[22–24]. The ability to use specific intermolecular interactions to assemble molecular devices appropriately is another critical challenge for molecular electronics. [25] Therefore, a quantitative understanding of the electron transport between adjacent molecules is an essential pre-requisite.

Most studies - both theoretical and experimental - focus on simple electrode molecule-electrode systems, which will be discussed in this thesis. Experimentally, the systems can be studied using Scanning Tunneling Microscopy Break Junctions (STM-BJ) [26-28] and Mechanically Controllable Break Junctions MCBJ [29,30]. Recently, more scalable techniques for contacting single molecules have been developed, including graphene-based junctions [31-34], silicene-based junctions [35] and CMOS-compatible electrodes, such as Pt and Pd [36]. However as anticipated many years ago [37] structural defects in 2d hexagonal materials [38] mean that their use as electrodes is still in its infancy and for the moment gold break junctions remain the contacting method of choice. Within such constraints, several methods of controlling electron transport have been developed, including mechanical gating [39, 40] and electrochemical gating [41,42]. In this thesis, I shall investigate an alternative method of control, based on utilising heteroaromaticity within molecular cores.

The realization of single-molecule electronic devices is challenging in several ways. First, the typical length of molecules used in the research field is in the order of 1–2 nm. In addition, electrodes, typically made of noble metals, separated by 1–2 nm is beyond the limits of classical top-down lithographic techniques. Second, due to the tiny dimensions of the molecule, it is typically impractical to place the molecule in the nanogap by direct manipulation. Instead, chemical interaction between the molecule and the electrode is needed for positioning of a molecule in the gap between the electrodes. Third, since the electrodes are typically much larger than the molecules, it is an additional challenge to make sure that only a single molecule is placed in each functional device. In addition to these three basic challenges, other challenges such as device stability, uniformity, yield, and scalability are equally important. [44].

1.2 Thesis Outline

My aim in this thesis is to review the theoretical techniques to treat electron transport in molecular scale junctions. The theoretical approach includes two main techniques, Density Functional Theory (Ch. 2), which is implemented in the SIESTA code [43] and the non- equilibrium Greens function formalism of transport theory (Ch. 3). Both of these methods are used to extensively study a family of molecules, where the heteroaromaticity in the molecular core units is modified. In this case the molecules are attached to gold leads and the connectivity is also studied by investigating para- para and meta-meta coupling. Furthermore. An analytical formula to explain the behaviour of these molecules is also presented in chapter 4.

The electrical conductance, IV characteristics and rectification ratio for asymmetric molecules attached to carbon nanotubes are presented in chapter 5. These calculations were performed using two different methods; the first is a four orbital tight binding molecule and the second the DFT quantum transport approach. To show the nature of the transport remains quantum tunnelling in this strongly bound system the beta factor was calculated for different length phenyl based molecules. Finally, Chapter 6 presents a theoretical study of the conductance perpendicular to the plane (z-direction) of a series of polycyclic aromatic hydrocarbons of different size and shape. Again, using a simple tight binding method and DFT the suitability to use these structures as molecular wires is investigated.

Reference

[1] “Visions for a molecular future,” Nature Nanotechnology, vol. 8, no. 6, pp. 385–389, 2013.

[2] J. L. Christopher, L. A. Estroff, J. K. Kriebel, R. G. Nuzzo, and G. M. Whitesides, “Self-assembled monolayers of thiolates on metals as a form of nanotechnology,” Chemical Reviews, vol. 105, no. 4, pp. 1103–1170, 2005. PMID: 15826011.

[3] S. V. Aradhya and L. Venkataraman, “Single-molecule junctions beyond electronic transport,” Nature Nanotechnology, vol. 8, no. 6, pp. 399–410, 2013.

[4] S. Sangtarash, C. Huang, H. Sadeghi, G. Sorohhov, J. Hauser, T. Wandlowski, W. Hong,S. Decurtins, S.-X. Liu, and C. J. Lambert, “Searching the Hearts of Graphene-like Molecules for Simplicity, Sensitivity, and Logic,” Journal of the American Chemical Society, vol. 137, no. 35, pp. 11425–11431, 2015.

[5] Yan Geng, Sara Sangtarash, Cancan Huang, Hatef Sadeghi, Yongchun Fu, Wenjing Hong, Thomas Wandlowski, Silvio Decurtins, Colin J Lambert, Shi-Xia Liu, “Magic ratios for connectivity-driven electrical conductance of graphene-like molecules,” Journal of the American Chemical Society 137 (13), 4469-4476 (2015)

[6] H. Sadeghi, L. Algaragholy, T. Pope, S. Bailey, D. Visontai, D. Manrique, J. Ferrer, V. Garcia-Suarez, S. Sangtarash, and C. J. Lambert, “Graphene sculpturene nanopores for DNA nucleobase sensing,” Journal of Physical Chemistry B, vol. 118, no. 24, pp. 6908–6914, 2014.

[7] H Sadeghi, S Bailey, CJ Lambert, “Silicene-based DNA nucleobase sensing,” Applied Physics Letters 104 (10), 103104, 2014.

[8] T. Prodromakis, C. Toumazou, and L. Chua, “Two centuries of memristors,” Nature Materials, vol. 11, no. 6, pp. 478–481, 2012.

[9] C. J. Lambert, “Basic concepts of quantum interference and electron transport in singlemolecule electronics,” Chem. Soc. Rev., vol. 44, pp. 875–888, 2015.

[10] H. Sadeghi, S. Sangtarash, and C. J. Lambert, “Oligoyne molecular junctions for efficient room temperature thermoelectric power generation,” Nano letters, vol. 15, no. 11, pp. 7467–7472, 2015.

[11] Sadeghi, H.; S. Sangtarash, S.; Lambert, C. J., “Enhanced Thermoelectric Efficiency of Porous Silicene Nanoribbons,” Scientific Reports 5, 9514 (2015)

[12] A. Aviram, M. A. Ratner, Chem. Phys. Lett. 1974, 29, 277 – 283.

[13] A. Batra, P. Darancet, Q. Chen, J. S. Meisner, J. R. Widawsky, J. B. Neaton, C. Nuckolls, L. Venkataraman, Nano Lett. 2013, 13, 6233 –6237.

[14] Zhao, Jin, et al. "Single C 59 N molecule as a molecular rectifier." Physical review letters 95.4 (2005): 045502.

[15] Lei, Shulai, et al. "Orbital-selective single molecule rectifier on graphene-covered Ru (0001) Surface." Applied Physics Letters 102.16 (2013): 163506..

[16] Wang, Bing, et al. "Conduction Mechanism of Aviram− Ratner Rectifiers with Single Pyridine− σ− C60 Oligomers." The Journal of Physical Chemistry B 110.48 (2006): 24505-24512..

[17] Lafferentz, Leif, et al. "Conductance of a single conjugated polymer as a continuous function of its length." Science 323.5918 (2009): 1193-1197..

[18] Choi, Seong Ho, BongSoo Kim, and C. Daniel Frisbie. "Electrical resistance of long conjugated molecular wires." Science 320.5882 (2008): 1482-1486.

[19] Zhao, Xiaotao, et al. "Oligo (aryleneethynylene) s with terminal pyridyl groups: synthesis and length dependence of the tunnelling to hopping transition in single-molecule conductances." Chemistry of materials. 25.21 (2013): 4340-4347.

[20] Davis, William B., et al. "Molecular-wire behaviour in p-phenylenevinylene oligomers." Nature 396.6706 (1998): 60-63.

[21] Kaliginedi, Veerabhadrarao, et al. "Correlations between molecular structure and single-junction conductance: a case study with oligo (phenylene-ethynylene)-type wires." Journal of the American Chemical Society 134.11 (2012): 5262-5275.

[22] Chen, J., et al. "Room-temperature negative differential resistance in nanoscale molecular junctions." Applied physics letters 77.8 (2000): 1224-1226.

[23] Guisinger, Nathan P., et al. "Room temperature negative differential resistance through individual organic molecules on silicon surfaces." Nano Letters 4.1 (2004): 55-59.

[24] Chen, J., et al. "Large on-off ratios and negative differential resistance in a molecular electronic device." science 286.5444 (1999): 1550-1552..

[25] Pijper, Thomas C., et al. "Reversible light induced conductance switching of asymmetric diarylethenes on gold: surface and electronic studies." Nanoscale 5.19 (2013): 9277-9282.

[26] Li, Chen, et al. "Charge transport in single Au vertical bar alkanedithiol vertical bar Au junctions: Coordination geometries and conformational degrees of freedom." Journal of the American Chemical Society 130.1 (2008): 318-326..

[27] Xu, Bingqian, and Nongjian J. Tao. "Measurement of single-molecule resistance by repeated formation of molecular junctions." Science 301.5637 (2003): 1221-1223.

[28] GJ Ashwell, B Urasinska, C Wang, MR Bryce, I Grace, CJ Lambert, “Single-molecule electrical studies on a 7 nm long molecular wire” Chemical Communications, 4706-4708 2006

[29] Huber, R.; Gonzalez, M. T.; Wu, S.; Langer, M.; Grunder, S.; Horhoiu, V.; Mayor, M.; Bryce, M. R.; Wang, C. S.; Jitchati, R.; Schonenberger, C.; Calame, M. J. Am. Chem. Soc. 2008, 130, 1080-1084.

[30] Hong, W.; Manrique, D. Z.; Moreno-Garca, P.; Gulcur, M.; Mishchenko, A.; Lambert, C. J.; Bryce, M. R.; Wandlowski, T. J. Am. Chem. Soc. 2011, 134, 2292-2304.

[31] H Sadeghi, JA Mol, CS Lau, GAD Briggs, J Warner, CJ Lambert, "Conductance enlargement in picoscale electroburnt graphene nanojunctions," Proceedings of the National Academy of Sciences 112 (9), 2658-2663, 2015

[32] JA Mol, CS Lau, WJM Lewis, H Sadeghi, C Roche, A Cnossen, JH Warner, C.J. Lambert, H.L. Anderson and G.A.D. Briggs, "Graphene-porphyrin single-molecule transistors," Nanoscale 7 (31), 13181-13185, 2015

[33] XH Zheng, GR Zhang, Z Zeng, VM García-Suárez, CJ Lambert, "Effects of antidots on the transport properties of graphene nanoribbons," Physical Review B 80 (7), 075413, 2009

[34] H Sadeghi, S Sangtarash, CJ Lambert, "Enhancing the thermoelectric figure of merit in engineered graphene nanoribbons" Beilstein journal of nanotechnology 6, 1176 2015

[35] H Sadeghi, S Bailey, CJ Lambert, "Silicene-based DNA nucleobase sensing," Applied Physics Letters 104 (10), 103104 2014

[36] VM García-Suárez, AR Rocha, SW Bailey, CJ Lambert, S Sanvito, J Ferrer, "Single-channel conductance of H 2 molecules attached to platinum or palladium electrodes," Physical Review B 72 (4), 045437, 2005

[37] CJ Lambert, DL Weaire, "Theory of the arrangement of cells in a network" Metallography 14 (4), 307-318 1981

[38] Detailed Atomic Structure of Defects in 2D Materials: From Graphene to Transition Metal Dichalcogenides, JH Warner, Microscopy and Microanalysis 21, 573 2015

[39] CM Finch, S Sirichantaropass, SW Bailey, IM Grace, VM Garcia-Suarez, C J Lambert, "Conformation dependence of molecular conductance: chemistry versus geometry," Journal of Physics: Condensed Matter 20 (2), 022203 2007

[40] Laura Rincón-García, Ali K Ismael, Charalambos Evangeli, Iain Grace, Gabino Rubio-Bollinger, Kyriakos Porfyrakis, Nicolás Agraït, Colin J Lambert "Molecular design and control of fullerene-based bi-thermoelectric materials" Nature materials 15 (3), 289-293 (2016)

[41] Yonghai Li, Masoud Baghernejad, Al-Galiby Qusiy, David Zsolt Manrique, Guanxin Zhang, Joseph Hamill, Yongchun Fu, Peter Broekmann, Wenjing Hong, Thomas Wandlowski, Deqing Zhang, Colin Lambert, "Three-State Single-Molecule Naphthalenediimide Switch: Integration of a Pendant Redox Unit for Conductance Tuning" Angewandte Chemie International Edition 54 (46), 13586-13589 2015

[42] VM García-Suárez, CJ Lambert, DZ Manrique, T Wandlowski, "Redox control of thermopower and figure of merit in phase-coherent molecular wires," Nanotechnology 25 (20), 205402 2014

[43] Josie M Soler, Emilio Artacho, Julian D Gale, Alberto Garcia, Javier Junquera, Pablo Ordejon, and Daniel Snchez-Portal. The SIESTA method for ab initio order-N materials simulation. Journal of Physics: Condensed Matter, 14(11):2745-2779 (2002)

[44] Moth-Poulsen, Kasper, ed. Handbook of single-molecule electronics. CRC Press, 2016.

Chapter 2

2. Density Functional Theory

2.1 Introduction

In order to understand the behavior of molecular electronic devices it is necessary to possess a reliable source of structural and electronic information. In this chapter I will give a brief summary of density functional theory (DFT) and the SIESTA (Spanish Initiative for Electronic Simulations with Thousands of Atoms) code [1], which I have used extensively throughout my PhD studies as a theoretical tool to investigate the structures of molecules, charge densities and band structures both qualitatively and quantitatively. SIESTA is a set of methods and a complete software package that can be used to perform DFT calculations on a considerable number of atoms (~1000) within hours, days or weeks.

The fundamental assertion of density functional theory is that any physical property of a complex system, consisting of many interacting particles, can be expressed as a functional of the ground-state density of the system. The proof of the existence of such a functional was first presented by Hohenberg and Kohn [2] in 1964. The proof is surprisingly simple, but it does not provide us with any hint of the actual form of the functional. Despite this, an ansatz proposed by Kohn and Sham [3] opened the door to applications for realistic physical systems. Density functional theory has since become a standard tool in theoretical physics and molecular chemistry.

This chapter is going to present a short overview of the foundations and numerical applications of DFT. The literature is quite broad and deals with the subject with considerably more detail [4-7]. I will begin by posing the general many body problem and the possible solution to it via the Hartree-Fock method and then I'll show the Hohenberg-Kohn theorems and the Kohn-Sham ansatz. Secondly, I sum up the most widely used functionals of the exchange and correlation energy, which are of paramount importance in practical numerical calculations. Finally, I will deal with localized basis sets and pseudo-atomic orbitals which define the Hilbert space of the numerical calculations presented in this thesis.

2.2 The Schrödinger Equation and Variational Principle

Any given non-relativistic many particles system can be described by the time independent, non-relativistic Schrödinger equation:

$$H\Psi_i(\vec{r}_1,\vec{r}_2..\vec{r}_N,\vec{R}_1,\vec{R}_2..\vec{R}_M) = E_i\Psi_i(\vec{r}_1,\vec{r}_2..\vec{r}_N,\vec{R}_1,\vec{R}_2..\vec{R}_M) \qquad 2.1$$

Here H represents the Hamiltonian operator of a system consisting of N-electrons and M-nuclei which describes the interaction of particles with each other, where Ψ_i is the wavefunction of the i^{th} state of the system and E_i is the numerical value of the energy of the state described by Ψ_i. The Hamiltonian operator of such a system can be written as a sum of five terms given by [2, 3, 8-12]:

$$H = \overbrace{-\frac{\hbar^2}{2m_e}\sum_{i=1}^{N}\nabla_i^2}^{T_e} \overbrace{-\frac{\hbar^2}{2m_n}\sum_{n=1}^{M}\nabla_n^2}^{T_n} \overbrace{-\frac{1}{4\pi\varepsilon_o}\sum_{i=1}^{N}\sum_{n=1}^{M}\frac{Ze^2}{|\vec{r}_i-\vec{R}_n|}}^{U_{en}} + \overbrace{\frac{1}{8\pi\varepsilon_o}\sum_{i=1}^{N}\sum_{j\neq i}^{N}\frac{e^2}{|\vec{r}_i-\vec{r}_j|}}^{U_{ee}}$$

$$+\overbrace{\frac{1}{8\pi\varepsilon_o}\sum_{n=1}^{M}\sum_{n\neq\grave{n}}^{M}\frac{Z_nZ_{\acute{n}}e^2}{|\vec{R}_n-\vec{R}_{\acute{n}}|}}^{U_{nn}} \qquad 2.2$$

Here *i* and *j* denote the *N*-electrons while *n* and *ń* run over the *M*-nuclei in the system, m_e and m_n are the mass of electron and nucleus respectively, *e* and Z_n are the electron and nuclear charge respectively. The position of the electrons and nuclei are denoted as $\vec{r}_i$ *and* $\vec{R}_n$ respectively, and ∇^2 is the Laplacian operator, in Cartesian coordinates is defined as:

$$\nabla_i^2 = \frac{\partial^2}{\partial x_i^2}+\frac{\partial^2}{\partial y_i^2}+\frac{\partial^2}{\partial z_i^2} \qquad 2.3$$

In the equation (2.2), the first and second terms, T_e and T_n represent the kinetic energy of electrons and nuclei respectively. The last three terms represent the potential part of the Hamiltonian; where U_{en} defines the attractive electrostatic interaction between electrons and nuclei. The electron-electron, U_{ee} and nuclear-nuclear, U_{nn} describe the repulsive part of the potential respectively [1, 3, 6, 9, 13].

We can separate the Hamiltonian (Eq. 2.2) into two parts. The first part contains the kinetic terms of the nuclei and the repulsive electrostatic potential between the nuclei and the attractive potential felt by the electrons due to the positively charged nuclei. This part is system specific and will determine the geometric properties of the physical problem. The second part of the Hamiltonian contains terms which only depend on the electrons. This part is universal in all problems. Hence we can rewrite the Hamiltonian for the electronic degrees of freedom as:

$$H = \overbrace{\sum_i V_{ext}(r_i)}^{\text{nuclei}-\text{electron interaction}} \underbrace{-\frac{\hbar^2}{2m_e}\sum_i \nabla_i^2}_{\text{kinetic term}} + \overbrace{\frac{1}{8\pi\varepsilon_o}\sum_{i\neq j}\frac{e^2}{|\vec{r}_i - \vec{r}_j|}}^{\text{electron}-\text{electron interaction}} \qquad 2.4$$

Where V_{ext} contains the system-specific nuclei terms of Eq. 2.2.

It is convenient to work with Hartree atomic units. This means that in the following we adopt the convention that the length scale is set by the Bohr radius of the hydrogen atom, a_o, the energy scale is set by the ground state of the hydrogen atom, the mass scale is set by the electron mass, m_e, the charge scale is set by the elementary charge of the electron, e, the angular momentum scale is set by the reduced Planck's constant, $\hbar$, and the electric force scale is set by $1/4\pi\varepsilon_o$.

Once we have solved the Schrödinger equation (Eq. 2.1) and we know the wavefunction, Ψ, we can calculate all physical quantities we are interested in. However, even for modest system sizes - even a couple of atoms - the diagonalization of the general problem is practically impossible even on a modern supercomputer.

The virtue of density functional theory is that it expresses the physical quantities in terms of the ground-state density. The electronic density of a general many body state, characterized by a wave function,$\Psi(r_1, r_2 \dots\dots r_n)$, is defined as:

$$\rho(r) = \int dr_1\, dr_2 \dots dr_i |\Psi(r_1, r_2, \dots. r_i)|^2 \qquad 2.5$$

2.3 The Hohenberg-Kohn Theorems

P. Hohenberg and W. Kohn, in 1964 [2], showed that there is tight, unequivocal relation between the ground state energy and the density, $\rho(r)$, of an interacting electron system. The Hohenberg-Kohn theorems are two very simple yet powerful statements:

1. The external potential, V_{ext}, is a unique functional of the density, $\rho(r)$. Since V_{ext} fixes the Hamiltonian of the system, H, it is clear that the full many-body ground-state is a unique functional of $\rho(r)$.
2. The ground state energy, E_{HK}, is a functional of the ground-state density, $\rho(r)$.

Proving the validity of the first theorem shown above is a simple matter of *reduction ad absurdum*. Let us assume we have two external potentials, V_{ext}^{1} andV_{ext}^{2}, which differ by more than a constant. Let us also assume that the two external potentials yield the same ground-state density, $\rho(r)$.

The Hamiltonians for each system are denoted $H^{(1)}$ and $H^{(2)}$ and, since they are different, they will have different ground-state wavefunctions, $\Psi^{(1)}$ and $\Psi^{(2)}$. Since $\Psi^{(2)}$ is not a ground state of $H^{(1)}$, we have:

$$E^{(1)} = \langle \Psi^{(1)} | H^{(1)} | \Psi^{(1)} \rangle < \langle \Psi^{(2)} | H^{(1)} | \Psi^{(2)} \rangle \qquad 2.6$$

And, similarly:

$$E^{(2)} = \langle \Psi^{(2)} | H^{(2)} | \Psi^{(2)} \rangle < \langle \Psi^{(1)} | H^{(2)} | \Psi^{(1)} \rangle \qquad 2.7$$

For simplicity, we assume that we have non-degenerate ground states. The problem has been formulated to incorporate degeneracies in the literature [11,15]. We can rewrite Eq. 2.6:

$$\langle \Psi^{(2)} | H^{(1)} | \Psi^{(2)} \rangle = \langle \Psi^{(2)} | H^{(2)} | \Psi^{(2)} \rangle + \langle \Psi^{(2)} | H^{(1)} - H^{(2)} | \Psi^{(2)} \rangle$$
$$= E^{(2)} + \int dr \left(V_{ext}^{(1)}(r) - V_{ext}^{(2)}(r) \right) \rho_o(r) \qquad 2.8$$

And Eq. 2.7:

$$\langle \Psi^{(1)} | H^{(2)} | \Psi^{(1)} \rangle = E^{(1)} + \int dr \left(V_{ext}^{(2)}(r) - V_{ext}^{(1)}(r) \right) \rho_o(r) \qquad 2.9$$

Adding Eq. 2.6 and Eq. 2.7, we find the contradiction: $E^{(1)} + E^{(2)} < E^{(1)} + E^{(2)}$. Hence, there cannot be two external potentials that differ by more than a constant and give the same ground-state density.

The second theorem is proven just as simply as the first. Consider the expression for the total energy, E, of the system with density ρ:

$$E(\rho) = T(\rho) + E_{int}(\rho) + \int dr\, V_{ext}(r)\rho(r) \qquad 2.10$$

The kinetic term, T, and internal interaction of the electrons, E_{int}, are, by definition, universal.

Consider a system with the ground-state density ρ_o and corresponding external potential, V_{ext}, and wavefunction, Ψ_o. The first theorem tells us that ρ_o will determine the Hamiltonian, H, so for any density, ρ and wavefunction, Ψ, other than the ground-state, we find:

$$E_o = \langle \Psi_o | H | \Psi_o \rangle < \langle \Psi | H | \Psi \rangle = E \qquad 2.11$$

Thus the ground-state density, ρ_o, minimizes the functional (Eq. 2.10). It follows that if we know the functional: $T(\rho) + E_{int}(\rho)$, then by minimizing Eq. 2.10 we get the ground-state of the system and can calculate all ground-state properties we are interested in.

2.4 The Kohn-Sham Theorems

So far, we have seen that, by obtaining the ground-state density, one can in principle calculate the ground-state energy and more. However, the exact form of the functional shown in Eq. 2.10 is not known. The kinetic term and internal energies of the interacting particles cannot generally be expressed as functional of the density. The solution was introduced by Kohn and Sham in 1965 [3].

According to Kohn and Sham we can replace the original Hamiltonian of the system by an effective Hamiltonian of non-interacting particles in an effective external potential, which has the same ground-state density as the original system. Since there is no clear recipe for doing this, this step is simply an ansatz, but it is considerably easier to solve a non-interacting problem. The energy functional of the Kohn-Sham ansatz, in contrast to Eq. 2.10, will have the form:

$$E_{KS}(\rho) = T_{KS}(\rho) + \int dr\, V_{ext}(r)\rho(r) + E_H(\rho) + E_{xc}(\rho) \qquad 2.12$$

Here, T_{KS} is the kinetic energy of the non-interacting system. In Eq. 2.10, we used the kinetic energy for the interacting system: T. the difference is referred to the exchange correlation functional, E_{xc} (Eq. 2.14).

E_H is the Hartree functional, which describes the electron-electron interaction using the Hatree-Fock method and it is take the form:

$$E_H(\rho) = \frac{1}{2}\int \frac{\rho(r)\rho(\acute{r})}{|r-\acute{r}|}\, dr d\acute{r} \qquad 2.13$$

This is an approximate version of E_{int}, as defined previously. Again, the difference is referred to E_{xc}. so the exchange correlation functional, E_{xc}, represents the differences between the exact and approximated solutions to both the kinetic energy term and the electron-electron interaction term. Its definition follows:

$$E_{xc}(\rho) = \left(E_{int}(\rho) - E_H(\rho)\right) + \left(T(\rho) - T_{KS}(\rho)\right) \qquad 2.14$$

The first three functionals of Eq. 2.12 are trivially defined in practice and account for most of the contribution to the ground-state energy. By comparison, the contribution of the exchange correlation functional is small. However, despite decades of research, it does not have an exact solution. Some very good approximations have been developed, which are discussed in the next section.

2.5 The Exchange Correlation Functionals

There are numerous proposed forms for the exchange and correlation energy in the literature. The first successful - and yet simple - form was the Local Density Approximation (LDA) [17, 18], which depends only on the density and is therefore a local functional. Then the next step was the Generalized Gradient Approximation (GGA) [19-22], including the derivative of the density it also contains information about the neighborhood and therefore is semi-local.

LDA and GGA are the two most commonly used approximations to the exchange and correlation energies in density functional theory. There are also several other functionals, which go beyond LDA and GGA. Some of these functionals are tailored to fit specific needs of basis sets used in solving the Kohn-Sham equations (Eq. 2.12) and a large category are the so called hybrid functionals (eg. B3LYP [16], HSE [23] and Meta hybrid GGA [24, 25]), which combine the LDA and GGA forms.

One of the latest and most universal functionals, the Van der Waals density functional (vdW-DF) [26], contains non-local terms and has proven to be very accurate in systems where dispersion forces are important [27,28].

The following sections will briefly describe the Local Density Approximation and the Generalized Gradient Approximation.

2.5.1 Local Density Approximation

In LDA, the exchange correlation functional depends only on the local density so we can expect this approximation to give good results for systems where the density is relatively smooth locally.

The LDA is in some sense the simplest form one could imagine for the exchange and correlation energies. It is a simple yet powerful functional and it is known to be accurate for graphene and carbon nanotubes or where the electron density is not rapidly changing. For example, a larger error is expected for atoms with *d*- and *f*-type orbitals. However LDA also has many pitfalls: the band gap in semiconductors and insulators is usually underestimated with a considerable error (≈ 10 - 30%), for example. It is therefore advisable to seek a better functional.

2.5.2 Generalized Gradient Approximation

GGA extends LDA by including the derivatives of the density into the functional form of the exchange and correlation energies. In this case there exists no closed form for the exchange part of the functional, hence it has to be calculated along with the correlation contributions using numerical methods. Just as in the case of the LDA there exist many parameterizations for the exchange and correlation energies in GGA [19-22].

LDA and GGA are the two most commonly used approximations for the approximation of exchange-correlation energies in the DFT. Also, there are several other functionals, which go beyond LDA and GGA. In general, there is no robust theory of the validity of these functionals. It is determined via testing the functional for various materials over a wide range of systems and comparing results with reliable experimental data.

2.6 Pseudopotentials

I have shown that by defining an exchange-correlation functional within the Kohn-Sham formalism it is possible to split a large interacting problem into a large effective non-interacting problem. From a physical viewpoint this vastly simplifies the problem. However in typical systems of molecules which contain many atoms, the calculation is still very large and has the potential to be computationally expensive. In order to reduce the number of electrons, one can introduce pseudopotentials which effectively remove the core electrons from an atom. Pseudopotentials were first introduced by Fermi in 1934 [32, 33] and since then methods have evolved from creating not so realistic empirical pseudopotentials [34,35] to more realistic ab-initio pseudopotentials [36-39].

The electrons in an atom can be split into two types: core and valence, where core electrons lie within filled atomic shells and the valence electrons lie in partially filled shells. Together with the fact that core electrons are spatially localized about the nucleus, only valence electron states overlap when atoms are brought together so that in most systems only valence electrons contribute to the formation of molecular orbitals. This allows the core electrons to be removed and replaced by a pseudopotential such that the valence electrons still feel the same screened nucleon charge as if the core electrons were still present. This reduces the number of electrons in a system dramatically and in turn reduces the time and memory required to calculate properties of molecules that contain a large number of electrons.

2.7 Basis Sets

It is clear that in order to find the wavefunctions, the Hamiltonian has to be diagonalised. This process involves the inversion of a large matrix whose computation time scales with the number of non-zero elements. Therefore, for efficient calculations the Hamiltonian is required to be sparse with many zeros. SIESTA utilizes a Linear Combination of Atomic Orbital (LCAO) basis set which are constrained to be zero after some defined cut-off radius, and are constructed from the orbitals of the atoms. The former produces the required sparse form of the Hamiltonian as the overlap between basis functions is reduced, and the latter allows even a minimal size basis set to produce properties close to that of the studied system.

The simplest basis set for an atom is called a single ζ basis, which corresponds to a single basis function, $\Psi_{nlm}(r)$ per electron orbital (i.e. 1 for an s-orbital, 3 for a p-orbital, etc.). In this case each basis function consists of a product of one radial wavefunction, $\emptyset_{nl}^{1}$ and one spherical harmonic Y_{lm}:

$$\Psi_{nlm}(r) = \emptyset_{nl}^{1}(r)Y_{lm}(\theta,\emptyset) \qquad 2.15$$

The radial part of the wavefunction is found by using the method proposed by Sankey [40,41], where the Schrodinger equation is solved for the atom placed inside a spherical box. It is under the constraint to vanish at a cut-off radius r_c. This constraint produces an energy shift δE within the Schrödinger equation such that the eigen functions first node occurs at r_c:

$$\left[-\frac{d^2}{dr^2}+\frac{l(l+1)}{2r^2}+V_{nl}^{ion}(r)\right]\emptyset_{nl}^{1}(r) = (\varepsilon_{nl}+\delta E)\emptyset_{nl}^{1}(r) \qquad 2.16$$

For higher accuracy basis sets (multiple-ζ), additional radial wavefunctions can be included for each electron orbital. The additional radial wavefunctions, phi_{nl}^{i} for $i > 1$, are calculated using a split-valence method. This involves defining a split valence cut off for each additional wavefunction, r_s^i , so it is split into two piecewise functions: a polynomial below the cut-off and the previous basis wasvefunction above it:

$$\emptyset_{nl}^{i}(r) = \begin{cases} r^l(a_{nl}-b_{nl}r^2) & r < r_s^i \\ \emptyset_{nl}^{i-1} & r_s^i < r < r_s^{i-1} \end{cases} \qquad 2.17$$

The additional parameters are found at the point r_s^i where the wavefunction and its derivative are assumed continuous.

Further accuracy (multiple-ζ polarized) can be obtained by including wavefunctions with different angular momenta corresponding to orbitals which are unoccupied in the atom. This is done by solving Eq. 2.16 in an electric field such that the orbital is polarized or deformed due to the field (see [1] for details) so a different radial function is obtained. This is now combined with the appropriate angular dependent spherical harmonic which increases the size of the basis. Table 2.1 shows the number of basis orbitals for a selected number of atoms for single-ζ, single- ζ polarized, double- ζ and double- ζ polarized.

Table 2.1: Table showing the number of radial basis functions per atom as used within the SIESTA for different degrees of precision. For clarity the specific orbitals are listed below each number, with ~ representing the polarization of that orbital.

Basis Set	H	C	Au
SZ	$1 =$ $(1 \times 1s)$	$4 =$ $(1 \times 2s + 3 \times 2p)$	$6 =$ $(1 \times 6s + 5 \times 5d)$
SZP	$4 =$ $(1 \times 1s + 3 \times 2\tilde{p})$	$9 =$ $(1 \times 2s + 3 \times 2p + 5 \times 3\tilde{d})$	$9 =$ $(1 \times 6s + 5 \times 5d + 3 \times 6\tilde{p})$
DZ	$2 =$ $(2 \times 1s)$	$8 =$ $(2 \times 2s + 6 \times 2p)$	$12 =$ $(2 \times 6s + 10 \times 5d)$
DZP	$5 =$ $(2 \times 1s + 3 \times 2\tilde{p})$	$13 =$ $(2 \times 2s + 6 \times 2p + 5 \times 3\tilde{d})$	$15 =$ $(2 \times 6s + 10 \times 5d + 3 \times 6\tilde{p})$

References

[1] Jose M Soler, Emilio Artacho, Julian D Gale, Alberto Garcea, Javier Junquera, Pablo Ordejon, and Daniel Snchez-Portal. The SIESTA method for ab initio order-N materials simulation. Journal of Physics: Condensed Matter, 14(11):2745-2779 (2002)

[2] P. Hohenberg and W. Kohn. Inhomogeneous Electron Gas. Phys. Rev., 136 (1964)

[3] W. Kohn and L. J. Sham. Self-Consistent Equations Including Exchange and Correlation Effects. Phys. Rev., 140, (1965)

[4] Richard M. Martin. Electronic Structure: Basic Methods and Practical Methods. Cambridge University Press, Cambridge, (2004)

[5] Robert G. Parr, Weitao Yang. Density-Functional Theory of Atoms and Molecules. Oxford University Press (1989)

[6] E K U Gross, E Runge, O Heinonen. Many Particle Theory. Taylor & Francis (1991)

[7] Eberhard K.U. Gross, Reiner M. Dreizler. Density Functional Theory. Plenum Press, New York (1995)

[8] M. Born and R. Oppenheimer. On the quantum theory of molecules. Annalen der Physik, 84:20 (1927)

[9] R.M. Martin. Electronic structure: basic theory and practical methods. Cambridge University Press (2008)

[10] David Jeffery Griffiths. Introduction to quantum mechanics. Pearson Prentice Hall (2005)

[11] M. Levy. Universal variational functionals of electron densities, first-order density matrices, and natural spin-orbitals and solution of the v-representability problem. Proceedings of the National Academy of Sciences, 76,12 (1979)

[12] Mel Levy. Electron densities in search of Hamiltonians. Phys. Rev. A, 26:3 (1982)

[13] Mel Levy and J.P. Perdew. Density Functional Methods in Physics. Plenum New York (1985)

[14] E. Lieb. Density functionals for Coulomb systems. MIT Pub. Cambridge, pp 111, (1982)

[15] E. Lieb. Density functional methods in physics. Plenum New York, pp11,(1985)

[16] Chengteh Lee, Weitao Yang, and Robert G. Parr. Development of the colle-salvetti correlation-energy formula into a functional of the electron density. Phys. Rev. B, 37:785-789 (1988)

[17] D. M. Ceperley and B. J. Alder. Ground State of the Electron Gas by a Stochastic Method. Phys. Rev. Lett., 45 (1980)

[18] DC Langreth and JP Perdew. Exchange-correlation energy of a metallic surface-wave-vector analysis. Phys. Rev. B, 15(6):2884-2901 (1977)

[19] John P. Perdew, Kieron Burke, and Matthias Ernzerhof. Generalized Gradient Approximation Made Simple. Phys. Rev. Lett., 77 (1996)

[20] A. D. Becke. Density-functional exchange-energy approximation with correct asymptotic behavior. Phys. Rev. A, 38:3098-3100 (1988)

[21] John P. Perdew and Yue Wang. Accurate and simple analytic representation of the electron-gas correlation energy. Phys. Rev. B, 45:13244-13249 (1992).

[22] B. Hammer, L. B. Hansen, and J. K. Norskov. Improved adsorption energetics within density-functional theory using revised perdew-burke-ernzerhof functionals. Phys. Rev. B, 59:7413-7421 (1999)

[23] Jochen Heyd, Gustavo E. Scuseria, and Matthias Ernzerhof. Hybrid functionals based on a screened coulomb potential. The Journal of Chemical Physics, 118(18):8207-8215 (2003)

[24] Yan Zhao and DonaldG. Truhlar. The M06 suite of density functionals for main group thermochemistry, thermochemical kinetics, noncovalent interactions, excited states, and transition elements: two new functionals and systematic testing of four M06-class functionals and 12 other functionals. Theoretical Chemistry Accounts, 120:215-241 (2008)

[25] Yan Zhao and Donald G. Truhlar. Applications and validations of the Minnesota density functionals. Chemical Physics Letters, 502(1-3):1-13 (2011)

[26] M. Dion, H. Rydberg, E. Schroder, D. C. Langreth, and B. I. Lundqvist. Van der Waals Density Functional for General Geometries. Physical Review Letters, 92(24):22-25 (2004)

[27] Jiri Klimeor, David Bowler, and Angelos Michaelides. Van der Waals density functionals applied to solids. Physical Review B, 83(19):1-13 (2011)

[28] David Visontai Quantum and Classical Dynamics of Molecule Size Systems. PhD thesis, Lancaster University, (2011).

[29] Lars Hedin and Stig Lundqvist. Effects of electron-electron and electron-phonon interactions on the one-electron states of solids. Solid State Physics 23:1-181. Academic Press (1970)

[30] S.H. Vosko, L. Wilk, and M. Nusair. Accurate spin-dependent electron liquid correlation energies for local spin density calculations: a critical analysis. Canadian Journal of Physics, 58:8 (1980)

[31] J. P. Perdew and Alex Zunger. Self-interaction correction to density functional approximations for many-electron systems. Phys. Rev. B, 23 (1981)

[32] E. Fermi. Il Nuovo Cimento, 11, 157, (1934)

[33] E. Fermi. Motion of neutrons in hydrogenous substances. Ricerca sci (1936)

[34] I. V. Abarenkov and V. Heine. The screened model potential for 25 elements. Phil. Mag., XII, 529 (1965)

[35] N. W. Ashcroft. Electron-ion pseudopotentials in metals. Phys. Lett., 23:48 (1966)

[36] A. Zunger and M. L. Cohen. First-principles nonlocal-pseudopotential approach in the density-functional formalism: Development and application to atoms. Phys. Rev. B, 18:5449 (1978)

[37] A. Zunger and M. L. Cohen. First-principles nonlocal-pseudopotential approach in the density-functional formalism. II. Application to electronic and structural properties of solids. Phys. Rev. B, 18:5449 (1979)

[38] D. R. Hamann, M. Schluter, and C. Chiang. Norm-Conserving Pseudopotentials. Phys. Rev. Lett. 43, 1494 (1979)

[39] Giovanni B. Bachelet and M. Schluter. Relativistic norm-conserving

[40] O. F. Sankey and D. J. Niklewski. Ab initio multicenter tight-binding model for molecular-dynamics simulations and other applications in covalent systems. Phys. Rev. B, 40, 3979 (1989).

[41] T. Pope. Quantum and Classical Dynamics of Molecular-Scale Junctions. PhD thesis, Lancaster University, (2013).

Chapter 3

3. Single Particle Transport

In molecular electronics, the goal is to understand electrical properties of molecular junctions; where a molecule (or sufficiently small structure) is bound to bulk electrodes so that ballistic transport can occur through its energy levels. The coupling strength between the leads and the molecule is usually small compared to the intra-electrode or intra-molecule bond strengths, which introduces a scattering process from the electrode to the molecule and from the molecule to the electrode. Since this system is not periodic, the electronic properties are no longer well described by the band structure, as calculated by the DFT method in Chapter 2. For this reason, a general approach is needed to understand the scattering process in the electrode junction and the molecular bridge. This can be achieved through the Green's function formalism.

In this chapter, I will begin with a brief overview of the Landauer formula. Following this, I will introduce the simplest form of a retarded Green's function for a one-dimensional tight binding chain. Next, I will break the periodicity of this lattice at a single connection and show that the Green's function is related directly to the transmission coefficient across the scattering region. The methods used on these simple systems will then be used to derive the transmission coefficient of mesoscopic conductors of arbitrarily complex geometry The method presented here assumes negligible interaction between carriers, the absence of inelastic processes and zero temperature.

3.1 The Landauer Formula

The Landauer formula [1,2, 3] is the standard way to describe transport phenomena in ballistic mesoscopic systems and is applicable for phase coherent systems, where a single wave function is sufficient to describe the electronic flow. It relates the conductance of a mesoscopic sample to the transmission properties of electrons passing through it. The method used to calculate the transmission properties will be discussed later in this chapter.

Figure 3.1 A mesoscopic scattering region connected to contacts by ballistic leads. The chemical potential in the contacts is μ_L and μ_R respectively. If an incident wave packet hits the scattering region from the left, it will be transmitted with probability $T = tt^*$ and reflected with probability $R = rr^*$. Charge conservation requires $T + R = 1$.

To start, we consider a mesoscopic scatter connected to two contacts, which behave as electron reservoirs, by means of two ideal ballistic leads (Fig. 3.1). All inelastic relaxation processes are limited to the reservoirs [4]. The reservoirs have slightly different chemical potentials $\mu_L - \mu_R > 0$, which will drive electrons from the left to the right reservoir. Initially, I will discuss the solution for one open channel (i.e. where only one electron is allowed to travel in a given direction).

To calculate the current in such a system we start by analyzing the incident electric current, δI, generated by the chemical potential gradient:

$$\delta I = ev\frac{\partial n}{\partial E}(\mu_L - \mu_R) \qquad 3.1$$

Where e is the electronic charge, v in the group velocity and $\frac{\partial n}{\partial E}$ is the density of states per unit length in the lead in the energy window defined by the chemical potentials of the contacts:

$$\frac{\partial n}{\partial E} = \frac{\partial n}{\partial k}\frac{\partial k}{\partial E} = \frac{\partial n}{\partial k}\frac{1}{v\hbar} \qquad 3.2$$

In one dimension, after including a factor of 2 for spin dependency, $\frac{\partial n}{\partial k} = \frac{1}{\pi}$

Substituting this into Eq. 3.2, we find that$\frac{\partial n}{\partial E} = \frac{1}{vh}$. This simplifies Eq. 3.1 to:

$$\delta I = \frac{2e}{h}(\mu_L - \mu_R) = \frac{2e^2}{h}\,\delta V \qquad 3.3$$

Where δV is the voltage generated by the chemical potential mismatch. From Eq. 3.3 it is clear that in the absence of a scattering region, the conductance of a quantum wire with one open channel is $\frac{2e^2}{h}$, which is approximately 77.5μS (or in other words, a resistance of 12.9 kΩ). This is an everyday quantity; it typically appears on the circuit boards of everyday electrical appliances. If now we consider a scattering region, the current collected in the right contacts will be:

$$\delta I = \frac{2e^2}{h}T\delta V \Longrightarrow \frac{\delta I}{\delta V} = G = \frac{2e^2}{h}T \qquad 3.4$$

This is the well-known Landauer formula, relating the conductance, *G*, of a mesoscopic scatterer to the transmission probability, T, of the electrons traveling through it. It describes the linear response conductance, hence it only holds for small bias voltages, $\delta V \approx 0$.

The Landauer formula has been generalized for the case of more than one open channel by Buttiker [4]. In this case the transmission coefficient is replaced by the sum of all the transmission amplitudes describing electrons incoming from the left contact and arriving to the right contact. The Landauer formula Eq. 3.3 for many open channels hence becomes:

$$\frac{\delta I}{\delta V} = G = \frac{2e^2}{h} \sum_{i,j} |t_{i,j}|^2 = \frac{2e^2}{h} Tr(tt^\dagger) \qquad 3.5$$

Where $t_{i,j}$ is the transmission amplitude describing scattering from the j^{th} channel of the left lead to the i^{th} channel of the right lead. With the definition of transmission amplitudes, one can introduce similarly reflection amplitudes $r_{i,j}$ which describe scattering processes where the particle is scattered from the j^{th} channel of the left lead to the i^{th} channel of the same lead. Combining reflection and transmission amplitudes one can define an object called the *S* matrix, which connects states coming from the left lead to the right lead and vice versa:

$$S = \begin{pmatrix} r & \acute{t} \\ t & \acute{r} \end{pmatrix} \qquad 3.6$$

Here *r* and *t* describe electrons coming of the left and $\acute{t}$ and $\acute{r}$ describe electrons coming from the right. Eq. 3.6 suggests that r, t, $\acute{r}$ and $\acute{t}$ are matrices for more than one channel, and could be complex (in the presence of a magnetic field for example). On the other hand charge conservation demands the S matrix be unitary: $SS^{\dagger} = I$. The S matrix is a central object of scattering theory. It is useful not just in describing transport in the linear response regime, but also in other problems, such as adiabatic pumping [4].

3.2 One-Dimension

Before presenting the generalized methodology, it is useful to calculate the scattering matrix for a simple one-dimensional system. This will give a clear outline of the methodology used. Green's functions will be used in the derivation, so I will first discuss the form of the Greens function for a simple one dimensional discretized lattice (Ch. 3.2.1) and then move on to calculating the scattering matrix of a one-dimensional scattered (Ch. 3.2.2).

3.2.1 Perfect One-Dimensional Lattice

In this section I will discuss the form of the Greens function for a simple one dimensional lattice with on-site energies ε_o and real hopping parameters as shown in Figure 3.2.

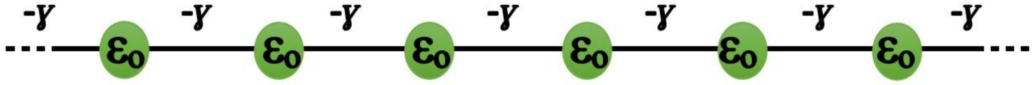

Figure 3.2 Tight-binding approximation of a one-dimensional periodic lattice with one site energies $\boldsymbol{\varepsilon_o}$ and coupling $\boldsymbol{\gamma}$

The matrix form of the Hamiltonian can be simply written:

$$H = \begin{pmatrix} \ddots & -\gamma & & & \\ -\gamma & \varepsilon_o & -\gamma & & \\ & -\gamma & \varepsilon_o & -\gamma & \\ & & -\gamma & \ddots & \end{pmatrix} \qquad 3.7$$

Within the tight-binding approximation, the Schrödinger equation (Eq. 3.8) can be expanded at a lattice site *z* in terms of the energy and wavefunction *Ψz* (Eq. 3.9).

$$(E - H)\psi = 0 \qquad 3.8$$

$$\varepsilon_o\psi_z - \gamma\psi_{z+1} - \gamma\psi_{z-1} = E\psi_z \qquad 3.9$$

The wavefunction for this perfect lattice takes the form of a propagating Bloch state (Eq. 3.10), normalized by its group velocity v in order for it to carry unit current flux. When this is substituted into Eq 3.9, it leads to the well-known one-dimensional dispersion relation (Eq. 3.11).

$$\psi_z = \frac{1}{\sqrt{v}} e^{ikz} \qquad 3.10$$

$$E = \varepsilon_o - 2\gamma\cos k \qquad 3.11$$

Where we introduced the quantum number, *k*, commonly referred to as the wavenumber.

The retarded Greens function $g(z, \acute{z})$ is closely related to the wavefunction and is in fact the solution to an equation very similar to that of the Schrödinger equation:

$$(E - H)g(z, \acute{z}) = \delta_{z,\acute{z}} \qquad 3.12$$

Physically, the retarded Greens function, $g(z, \acute{z})$, describes the response of a system at a point z due to a source at a point $\acute{z}$. Intuitively, we expect such an excitation to give rise to two waves, traveling outwards from the point of excitation, with amplitudes A^+ and A^- as shown in figure 3.3

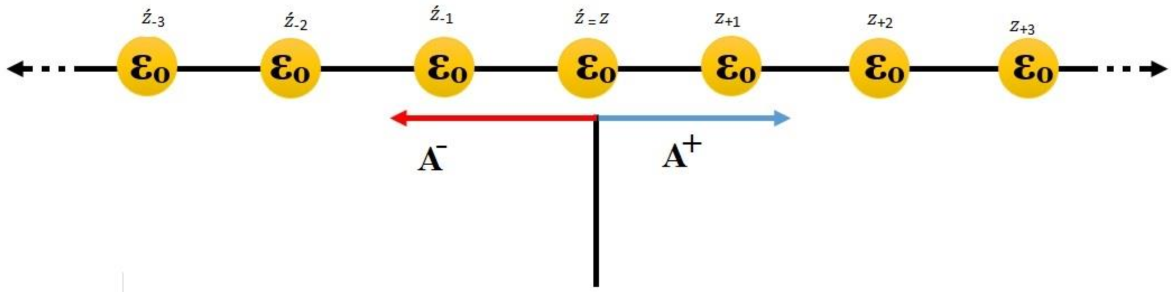

Figure 3.3 Retarded Green's Function of an infinite one-dimensional lattice. The Excitation at $l = j$ causes wave to propagate left and right with amplitudes A^- and A^+ Respectively

These waves can be expressed simply as:

$$
\begin{aligned}
g(\acute{z}, z) &= A^{+} e^{ikz} \qquad z > \acute{z} \\
g(\acute{z}, z) &= A^{-} e^{-ikz} \qquad z < \acute{z}
\end{aligned}
\qquad 3.13
$$

This solution satisfies Eq. 3.12 at every point but $z = \acute{z}$. To overcome this, the Green's function must be continuous (Eq. 3.14), so we equate the two at $z = \acute{z}$

$$A^{+} e^{ik\acute{z}} = A^{-} e^{-ik\acute{z}} \qquad 3.14$$

$$A^{-} = A^{+} e^{2ik\acute{z}} \qquad 3.15$$

Substituting Eq. 3.15 into the Green's functions (Eq. 3.13) yields:

$$g(\acute{z},z) = A^{+}e^{ik\acute{z}}e^{ik(z-\acute{z})} \qquad \acute{z} > z$$
$$g(\acute{z},z) = A^{+}e^{ik\acute{z}}e^{ik(\acute{z}-z)} \qquad \acute{z} < z \qquad 3.16$$

With a little thought, it is clear that this can be written simply as:

$$g(z,\acute{z}) = A^{+}e^{ik\acute{z}}e^{ik|z-\acute{z}|} \qquad 3.17$$

Where

$$A^{+} = \frac{e^{-ik\acute{z}}}{i\hbar v} \qquad 3.18$$

Hence $g(z,\acute{z}) = \dfrac{e^{ik|z-\acute{z}|}}{i\hbar v}$ 3.19

Where the group velocity, found from the dispersion relation, is:

$$v = \frac{dE(k)}{\hbar\, dk} = \frac{2\gamma sin(k)}{\hbar} \qquad 3.20$$

A more thorough derivation can be found in the literature [5, 8, 9].

3.2.2 One-Dimensional Scattering

In this section I will deal with two pieces of one dimensional tight binding semi-infinite leads connected by a coupling element α. Both leads have equal on-site potentials, ε_o, and hopping elements, -ɣ (see Figure 3.4). The analytical solutions for the transmission and reflection coefficients can be calculated easily.

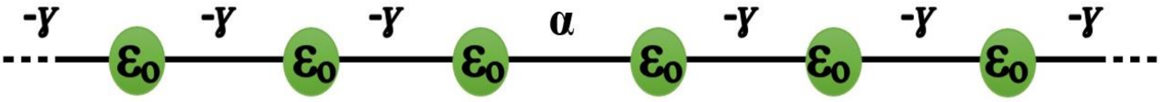

Figure 3.4 Simple tight-binding model of a one dimensional scattered attached to one dimensional leads.

Firstly, we need to define a Hamiltonian, which takes the form of an infinite matrix.

$$H = \begin{pmatrix} \ddots & -\gamma & & & & \\ -\gamma & \varepsilon_o & -\gamma & & & \\ & -\gamma & \varepsilon_o & \alpha & & \\ & & \alpha & \varepsilon_o & -\gamma & \\ & & & -\gamma & \varepsilon_o & -\gamma \\ & & & & -\gamma & \ddots \end{pmatrix} \qquad 3.21$$

For real γ, the dispersion relation corresponding to the leads introduced above was given in Eq. 3.11 and the group velocity was given in Eq. 3.20:

$$E(k) = \varepsilon_o - 2\gamma \cos k \qquad 3.22$$

$$v = \frac{1}{\hbar}\frac{dE}{dk} \qquad 3.23$$

In order to obtain the scattering amplitudes we need to calculate the Green's function of the system. The formal solution to Eq. 3.12 can be written as:

$$G = (E - H)^{-1} \qquad 3.24$$

Eq. 3. 24 is singular if the energy E is equal to an eigenvalues of the Hamiltonian H. To circumvent this problem, it is practical to consider the limit:

$$G_{\pm} = \lim_{\eta \to 0} (E - H \pm i\eta)^{-1} \tag{3.25}$$

Here η is a positive number and G+, G- is the retarded (advanced) Green's function. In this thesis I will only use retarded Green's functions and hence choose the + sign.

The retarded Green's function for an infinite, one dimensional chain with the same parameters is defined in Eq. 3.19:

$$g^{\infty}(j,l) = \frac{e^{ik|j-l|}}{i\hbar v} \tag{3.26}$$

Where j, l are the labels of the sites in the chain. In order to obtain the Green's function of a semi-infinite lead we need to introduce the appropriate boundary conditions. In this case, the lattice is semi-infinite, so the chain must terminate at a given point, i_0, so that all points for which $i \geq i_0$ are missing. This is achieved by adding a wave function to the Green's function to mathematically represent this condition. The wavefunction in this case is:

$$\psi_{jl}^{i_o} = -\frac{e^{ik(2i_o - l - j)}}{i\hbar v} \tag{3.27}$$

The Green's function $g(j,l) = g_{j,l}^{\infty} + \psi_{j,l}^{i_o}$ will have the following simple form at the

Boundary $j = l = i_0 - 1$:

$$g(i_o - 1, i_o - 1) = -\frac{e^{ik}}{\gamma} \tag{3.28}$$

If we consider the case of decoupled leads, $\alpha = 0$, the total Green's function of the system will simply be given by the decoupled Green's function:

$$g = \begin{pmatrix} -\frac{e^{ik}}{\gamma} & 0 \\ 0 & -\frac{e^{ik}}{\gamma} \end{pmatrix} = \begin{pmatrix} gL & 0 \\ 0 & gR \end{pmatrix} \qquad 3.29$$

If we now switch on the interaction, then in order to get the Green's function of the coupled system, G, we need to use Dyson's equation:

$$G^{-1} = (g^{-1} - V) \qquad 3.30$$

Here the operator V describing the interaction connecting the two leads will have the form:

$$V = \begin{pmatrix} 0 & V_c \\ V_c^{\dagger} & 0 \end{pmatrix} = \begin{pmatrix} 0 & \alpha \\ \alpha^* & 0 \end{pmatrix} \qquad 3.31$$

The solution to Dyson's equation, Eq. 3.30 reads:

$$G = \frac{1}{|\alpha|^2 - \gamma^2 e^{-2ik}} \begin{pmatrix} \gamma e^{-ik} & \alpha \\ \alpha^* & \gamma e^{-ik} \end{pmatrix} \qquad 3.32$$

The only remaining step is to calculate the transmission, t, and reflection, r, amplitudes from the Green's function Eq. 3.32. This is done by making use of the Fisher-Lee relation [5, 7] which relates the scattering amplitudes of a scattering problem to the Green's function of the problem. The Fisher-Lee relations in this case reads:

$$r = i\hbar v_L G_{00} - 1 \; ; \qquad t = i\hbar\sqrt{v_R v_L} G_{10} \qquad 3.33$$

and the transmission coefficient will be:

$$T \;=\; \hbar^2 v_R |G_{10}|^2 \;\; v_L \qquad 3.34$$

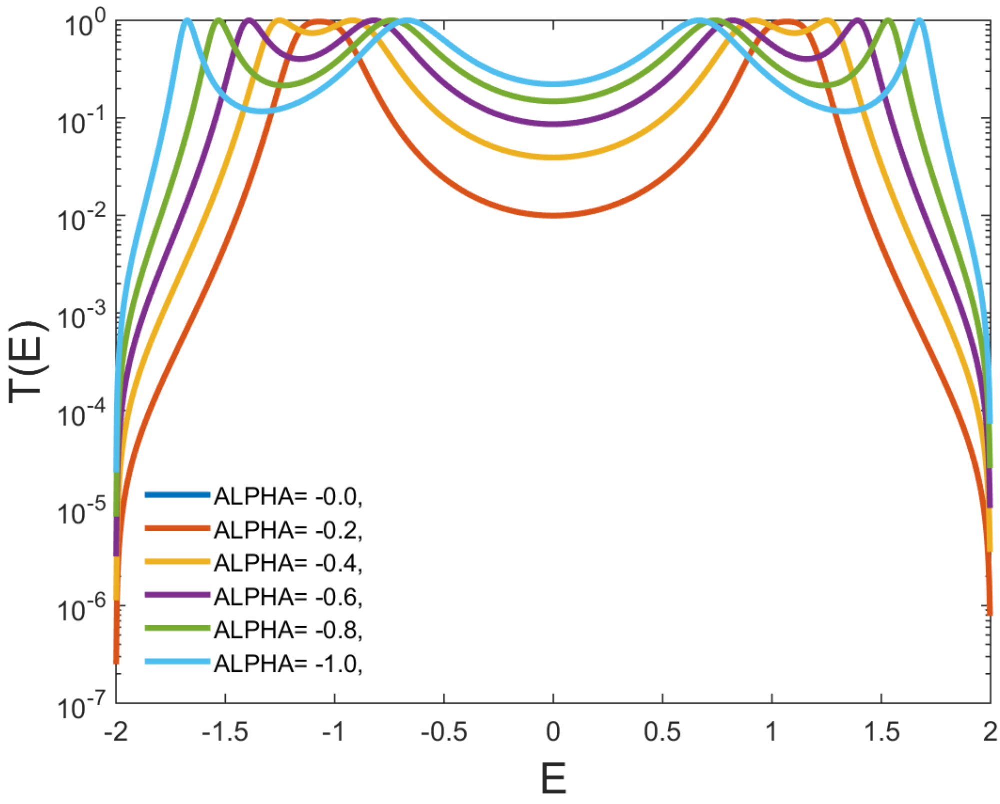

Figure 3.5 Transmission coefficient versus energy for carbon chain N=4 as in (figure 3.4) for α vary from 0 to -1 and ε_o=0

These amplitudes correspond to particles incident from the left. If one would consider particles coming from the right than similar expressions could be recovered for the transmission, $\acute{t}$, and reflection, $\acute{r}$, amplitudes.

Since we are now in the possession of the full scattering matrix we can use the Landauer formula Eq. 3.4 to calculate the zero bias conductance.

The procedure by which this analytical solution for the conductance of a one-dimensional scatterer was found can be generalized for more complex geometries. So to briefly summarize the steps:

1. The first step was to calculate the Green's function describing the surface sites of the leads.

2. The total Green's function in the presence of a scatterer is obtained by Dyson's equation.

3. The Fisher-Lee relation gives us the scattering matrix from the Green's function

4. Using the Landauer formula, we can then find the zero-bias conductance

3.3 Generalization of the Scattering Formalism

In this section I will show a generalized approach to transport calculations following the derivation of Lambert, presented in [2, 10, 11]. This is similar to the previous approach. First the surface Green's function of crystalline leads is computed, and the scattering amplitudes are recovered by means of a generalization of the Fisher-Lee relation.

3.3.1 Hamiltonian and Green's Function of the Leads

Firstly, we study a general semi-infinite crystalline electrode of arbitrary complexity. Because the leads are crystalline, the structure of the Hamiltonian is a generalization of the one-dimensional electrode Hamiltonian in Eq. 3.7. Figure 3.5 shows the general system topology. Instead of site energies, we have Hamiltonians for each repeating layer of the bulk electrode, H_0, and a coupling matrix to describe the hopping parameters between these layers, H_1.

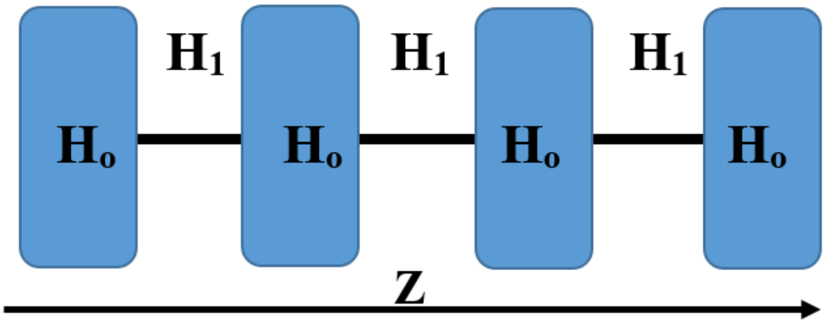

Figure 3.5 Schematic representation of a semi-infinite generalized lead. States described by the Hamiltonian H_0 are connected via generalized hopping H_1. The direction z is defined to be parallel to the axis of the chain. One can assign for each slice an individual z value.

The Hamiltonian for such a system has the form:

$$H = \begin{pmatrix} \ddots & H_1 & & \\ H_1^\dagger & H_o & H_1 & \\ & H_1^\dagger & H_o & H_1 \\ & & H_1^\dagger & \ddots \end{pmatrix} \qquad 3.35$$

Where H_0 and H_1 are in general complex matrices and the only restriction is that the full Hamiltonian, H, should be Hermitian. Our first goal in this section is to calculate the Green's function of such a lead for general H_1 and H_0.

In order to calculate the Green's function one has to calculate the spectrum of the Hamiltonian by solving the Schrödinger equation of the lead.

$$H_0\psi_z + H_1\psi_{z+1} + H_1^\dagger\psi_{z-1} = E\psi_z \qquad 3.36$$

Here ψ_z is the wave function describing layer z, where z is an integer measured in units of inter-layer distance. We assume the system is infinitely periodic in the z direction only, so the on-site wavefunction, ψ_z, can be represented in Bloch form; consisting of a product of a propagating plane wave and a wavefunction, ϕ_k, which is perpendicular to the transport direction, z. If the layer Hamiltonian, H_0, has dimensions $M \times M$ (or in other words consists of M site energies and their respective hopping elements), then the perpendicular wavefunction, ϕ_k, will have M degrees of freedom and take the form of a $1 \times M$ dimensional v ector. So the wave function, ψ_z, takes the form:

$$\psi_z = \sqrt{n_k}\ e^{ikz}\phi_k \qquad 3.37$$

Where, n_k is an arbitrary normalization parameter. Substituting this into the Schrödinger equation (Eq. 3.36) gives:

$$\left(H_o + e^{ik}H_1 + e^{-ik}H_1^\dagger - E\right)\phi_k = 0 \qquad 3.38$$

Typically, to find the band structure for such a problem, one would select values of k and calculate the eigenvalues at that point, $E = E_l(k)$, where $l = 1 \dots\dots M$. Here, l denotes the band index. For each value of k, there will be M solutions to the Eigen problem, and so M energy values. In this way, by selecting multiple values for k, it is relatively simple to build up a band structure. In a scattering problem, the problem is approached from the opposite direction; instead of finding the values of E at a given k, we find the values of k at a given E. In order to accomplish this, a root-finding might have been used, but this would have required an enormous numerical effort since the wave numbers are in general complex. Instead, we can write down an alternative eigenvalue problem in which the energy is the input and the wave numbers are the result by introducing the function:

$$v_k = e^{-ikz}\phi_k \qquad 3.39$$

And combining it with Eq. 3.38:

$$\begin{pmatrix} -H_1^{-1}(H_o - E) & -H_1^{-1}H_1^{\dagger} \\ I & 0 \end{pmatrix}\begin{pmatrix} \phi_k \\ v_k \end{pmatrix} = e^{ikz}\begin{pmatrix} \phi_k \\ v_k \end{pmatrix} \qquad 3.40$$

For a layer Hamiltonian, H_0, of size $M \times M$, Eq 3.40 will yield 2M eigenvalues, $e^{ik_l z}$ and eigenvectors, ϕ_k, of size M. We can sort these states into four categories according to whether they are propagating or decaying and whether they are left going or right going. A state is propagating if it has a real wave number, k_l, and is decaying if it has an imaginary part. If the imaginary part of the wave number is positive then we say it is a left decaying state, if it has a negative imaginary part it is a right decaying state. The propagating states are sorted according to the group velocity of the state defined by

$$v_{kl} = \frac{1}{\hbar}\frac{\partial E_{k,l}}{\partial k} \qquad 3.41$$

If the group velocity, v_{kl} , of the state is positive than it is a right propagating state if it is negative than it is a left propagating state.

Table 3.1: Sorting the eigenstates into left and right propagating or decaying states according to the wave number and group velocity.

	Left	Right
decaying	$Im(k_l) > 0$	$Im(k_r) < 0$
Propagation	$Im(k_l) = 0, v_g^{kl} < 0$	$Im(k_r) = 0, v_g^{kr} > 0$

For convenience, from now on I will denote the k_l wave numbers which belong to the left propagating decaying set of wave numbers by k_l and the right propagating decaying wave numbers will remain plainly k_r. Thus, ϕ_{kr} is a wave function associated to a right state and ϕ_{kl} is associated to a left state. If H_l is invertible, there must be exactly the same number, M, of left and right going states. It is clear that if H_l is singular, the matrix in Eq. 3.40 cannot be constructed, since it relies of the inversion of H_l. However, any one of several methods can be used to overcome this problem. The first [9-12] uses the decimation technique to create an effective, non-singular H_1. Another solution might be to populate a singular H_1 with small random numbers, hence introducing an explicit numerical error. This method is reasonable as the introduced numerical error can be as small as the numerical error introduced by decimation. Another solution is to re-write Eq 3.40 such that H_1 need not be inverted:

$$\begin{pmatrix} -(H_o - E) & -H_1^{\dagger} \\ I & 0 \end{pmatrix} \begin{pmatrix} \phi_k \\ v_k \end{pmatrix} = e^{ikz} \begin{pmatrix} H_1 & 0 \\ 0 & I \end{pmatrix} \begin{pmatrix} \phi_k \\ v_k \end{pmatrix} \qquad 3.42$$

However, solving this generalized Eigen-problem is more computationally expensive. Any of the aforementioned methods work reasonably in tackling the problem of a singular H_1 matrix, and so can the condition that there must be exactly the same number, M, of left and right going states, whether H_1 is singular or not [13-19].

The solutions to the eigenvalue equation (3.38) at a given wave number (k) will form an orthogonal basis set, however, the eigenstates $(\phi_{(k_l)})$ obtained by solving the Eigen-problem equation (3.42) at a given energy (E) will not generally form an orthogonal set of states. This is crucial, since we will have to deal with the non-orthogonality when constructing the Green's function. It is, therefore, necessary to introduce the duals to $\phi_{(k_l)}$ and $\phi_{(\bar{k}_l)}$ in such a way that they obey:

$$\tilde{\phi}^{\dagger}_{(k_i)}\phi_{(k_j)} = \tilde{\phi}^{\dagger}_{(\bar{k}_i)}\phi_{(\bar{k}_j)} = \delta_{ij} \qquad 3.43$$

This yields the generalized completeness relation:

$$\sum_{l=1}^{M} \tilde{\phi}^{\dagger}_{(k_l)}\phi_{(k_l)} = \sum_{l=1}^{M} \tilde{\phi}^{\dagger}_{(\bar{k}_l)}\phi_{(\bar{k}_l)} = I \qquad 3.44$$

Once we are in possession of the whole set of eigenstates at a given energy we can calculate the Green's function first for the infinite system and then, by satisfying the appropriate boundary conditions, for the semi-infinite leads at their surface. Since the Green's function satisfies the Schrödinger equation when $z \neq z'$, we can build up the Green's function from the mixture of the eigenstates $\phi_{(k_l)}$ and $\phi_{(\bar{k}_l)}$:

$$g(z,z') = \begin{array}{l} \sum_{l=1}^{M} \phi_{(k_l)} e^{ik_l(z-z')}\, \omega^{\dagger}_{k_l},\ z \geq z' \\ \sum_{l=1}^{M} \phi_{(\bar{k}_l)} e^{i\bar{k}_l(z-z')}\, \omega^{\dagger}_{\bar{k}_l},\ z \leq z' \end{array} \qquad 3.45$$

where the M-component vectors ω_{k_l} and $\omega_{\bar{k}_l}$ are to be determined. It is important to note the structural similarities between this equation and equation (3.13) and also that all the degrees of freedom in the transverse direction are contained in the vectors $\phi_{(k)}$ and ω_k.

The task now is to obtain the ω vectors. As in section 3.2.1, we know that equation (3.45) must be continuous at $z = z'$ and should fulfill the Green's equation (equation (3.12)). The first condition is expressed as:

$$\sum_{l=1}^{M} \phi_{(k_l)}\omega^{\dagger}_{k_l} = \sum_{l=1} \phi_{(\bar{k}_l)}\omega^{\dagger}_{\bar{k}_l} \qquad 3.46$$

and the second:

$$\sum_{l=1}^{M}\left[(E-H_o)\phi_{(k_l)}\omega^{\dagger}_{k_l} + H_1\phi_{(k_l)}e^{ik_l}\omega^{\dagger}_{k_l} + H_1^{\dagger}\phi_{(\bar{k}_l)}e^{-i\bar{k}_l}\omega^{\dagger}_{\bar{k}_l}\right] = I$$

$$\sum_{l=1}^{M}\left[(E-H_o)\phi_{(k_l)}\omega^{\dagger}_{k_l} + H_1\phi_{(k_l)}e^{ik_l}\omega^{\dagger}_{k_l} + H_1^{\dagger}\phi_{(\bar{k}_l)}e^{-i\bar{k}_l}\omega^{\dagger}_{\bar{k}_l} + H_1^{\dagger}\phi_{(k_l)}e^{-ik_l}\omega^{\dagger}_{k_l} - H_1^{\dagger}\phi_{(k_l)}e^{-ik_l}\omega^{\dagger}_{k_l}\right] = I$$

$$\sum_{l=1}^{N}\left[H_1^{\dagger}\phi_{(\bar{k}_l)}e^{i\bar{k}_l}\omega^{\dagger}_{\bar{k}_l} - H_1^{\dagger}\phi_{(k_l)}e^{-ik_l}\omega^{\dagger}_{k_l}\right] + \sum_{l=1}^{M}\left[(E-H_o) + H_1e^{ik_l} + H_1^{\dagger}e^{-ik_l}\right]\phi_{(k_l)}\omega^{\dagger}_{k_l} = I$$

and since, from the Schrödinger equation (equation (3.38)), we know that:

$$\sum_{l=1}^{M}\left[(E - H_o) + H_1 e^{ik_l} + H_1^{\dagger} e^{-ik_l}\right] \phi_{(k_l)} = 0 \qquad 3.47$$

This yields to:

$$\sum_{l=1}^{N} H_1^{\dagger}\left[\phi_{(\bar{k}_l)} e^{i\bar{k}_l} \omega_{\bar{k}_l}^{\dagger} - \phi_{(k_l)} e^{-ik_l} \omega_{k_l}^{\dagger}\right] = I \qquad 3.48$$

Now let us make use of the dual vectors defined in equation (3.43). Multiplying equation (3.46) by $\widetilde{\phi}_{(k_p)}$ we get:

$$\sum_{l=1}^{M} \widetilde{\phi}_{(k_p)}^{\dagger}\, \phi_{(\bar{k}_l)} \omega_{\bar{k}_l}^{\dagger} = \omega_{k_p}^{\dagger} \qquad 3.49$$

and similarly multiplying by $\widetilde{\phi}_{(\bar{k}_p)}^{\dagger}$ gives:

$$\sum_{l=1}^{M} \widetilde{\phi}_{(\bar{k}_p)}^{\dagger}\, \phi_{(k_l)} \omega_{k_l}^{\dagger} = \omega_{\bar{k}_p}^{\dagger} \qquad 3.50$$

Using the continuity equation (3.46) and equations (3.49) and (3.50), the Green's equation (equation (3.48)) becomes:

$$\sum_{l=1}^{M} \sum_{p=1}^{M} H_1^{\dagger}\left(\phi_{(\bar{k}_l)} e^{-i\bar{k}_l} \widetilde{\phi}_{(\bar{k}_l)}^{\dagger} - \phi_{(k_l)} e^{-ik_l} \widetilde{\phi}_{(k_l)}^{\dagger}\right) \phi_{(\bar{k}_p)} \omega_{\bar{k}_p}^{\dagger} = I \qquad 3.51$$

From which it follow:

$$\sum_{l=1}^{M}\left[H_1^\dagger\left(\phi_{(\bar{k}_l)}e^{-i\bar{k}_l}\tilde{\phi}^\dagger_{(\bar{k}_l)} - \phi_{(k_l)}e^{-ik_l}\tilde{\phi}^\dagger_{(k_l)}\right)\right]^{-1}$$

$$= \sum_{p=1}^{M}\phi_{(\bar{k}_p)}\omega^\dagger_{\bar{k}_p} = \sum_{p=1}^{M}\phi_{(k_p)}\omega^\dagger_{k_p} \qquad 3.52$$

This immediately gives us an expressions for $\omega^\dagger_k$:

$$\omega^\dagger_k = \tilde{\phi}^\dagger_{(k)}\nu^{-1} \qquad 3.53$$

where ν is defined as:

$$\nu = \sum_{l=1}^{M} H_1^\dagger\left(\phi_{(\bar{k}_l)}e^{-i\bar{k}_l}\tilde{\phi}^\dagger_{(\bar{k}_l)} - \phi_{(k_l)}e^{-ik_l}\tilde{\phi}^\dagger_{(k_l)}\right) \qquad 3.54$$

The wave number (k) in equation (3.53) refers to both left and right type of states. Substituting equation (3.53) into equation (3.45) we get the Green's function of an infinite system:

$$g^\infty_{z,z'} = \begin{cases}\sum_{l=1}^{M}\phi_{(k_l)}e^{ik_l(z-z')}\tilde{\phi}^\dagger_{(k_l)}\nu^{-1}, & z \geq z' \\ \sum_{l=1}^{M}\phi_{(\bar{k}_l)}e^{i\bar{k}_l(z-z')}\tilde{\phi}^\dagger_{(\bar{k}_l)}\nu^{-1}, & z \leq z'\end{cases} \qquad 3.55$$

In order to get the Green's function for a semi-infinite lead we have to add a wave function to the Green's function in order to satisfy the boundary conditions at the edge of the lead, as with the one dimensional case. The boundary condition here is that the

Green's function must vanish at a given place ($z = z_o$). In order to achieve this we simply add:

$$\Delta = -\sum_{l,p=1}^{M} \phi_{\bar{k}_l} e^{i\bar{k}_l(z-z_o)} \tilde{\phi}^{\dagger}_{(\bar{k}_l)} \phi_{(k_p)} e^{ik_p(z_o-z)} \tilde{\phi}^{\dagger}_{(k_p)} \nu^{-1} \qquad 3.56$$

To the Green's function, equation (3.55), $g = g^{\infty} + \Delta$. This yields the surface Green's function for a semi-infinite lead going left:

$$g_L = \left(I - \sum_{l,p=1}^{M} \phi_{(\bar{k}_l)} e^{-i\bar{k}_l} \tilde{\phi}^{\dagger}_{(\bar{k}_l)} \phi_{(k_p)} e^{ik_p} \tilde{\phi}^{\dagger}_{(k_p)}\right) \nu^{-1} \qquad 3.57$$

and going right:

$$g_R = \left(I - \sum_{l,p=1}^{M} \phi_{(k_l)} e^{ik_l} \tilde{\phi}^{\dagger}_{(k_l)} \phi_{(\bar{k}_p)} e^{-i\bar{k}_p} \tilde{\phi}^{\dagger}_{(\bar{k}_p)}\right) \nu^{-1} \qquad 3.58$$

All that remains is to obtain the hamiltonian of the scattering region using DFT and combine this with the surface Green's functions via Dyson's equation, to obtain the total Green's function and transmission amplitude t_{kl}[20]

$$G_{tot} = \left[\begin{pmatrix} g_L & o \\ o & g_R \end{pmatrix}^{-1} - H_{scatt}\right]^{-1} \qquad 3.59$$

$$t_{kl} = \tilde{\phi}^{\dagger}_{(k_l)} G_{tot} v \phi_{(k_l)} \sqrt{\frac{v_k}{v_l}} e^{ik_l} \qquad 3.60$$

Reference

[1] Li, C.; Pobelov, I.; Wandlowski, T.; Bagrets, A.; Arnold, A.; Evers, F. J. Am. Chem. Soc. 2008, 130, 318-326.

[2] David Visontai Quantum and Classical Dynamics of Molecule Size Systems. PhD thesis, Lancaster University, (2011).

[3] R Landauer. Spatial Variation of Currents and Fields Due to Localized Scatterers in Metallic Conduction. IBM J. Res. Dev., 1:233, (1957).

[4] M Buttiker, Y Imry, R Landauer, and S Pinhas. Generalized many channel conductance formula with application to small rings. Phys. Rev. B, 31(10):6207-6215, May (1985).

[5] S Datta. Electronic Transport in Mesoscopic Systems. Cambridge University Press, Cambridge, (1995).

[6] P W Brouwer. Scattering approach to parametric pumping. 58(16):135-138, (1998).

[7] Daniel S Fisher., and Patrick A. Lee. Relation between conductivity and transmission matrix. Physical Review B 23.12:6851-6854, (1981).

[8] E.N. Economou. Green's Functions in Quantum Physics. Springer Verlag, (1983).

[9] Pier A. Mello and Narendra Kumar. Quantum Transport in Mesoscopic Systems. Oxford University Press (2004).

[10] S. Sanvito. Giant Magnetoresistance and Quantum Transport in Magnetic Hybrid Nanostructures. PhD thesis, Lancaster University, (1999).

[11] C. M. Finch. An understanding of electrical characteristics of organic molecular devices. PhD thesis, Lancaster University, (2008).

[12] James G MacKinnon and Halbert White. Some heteroskedasticity-consistent covariance matrix estimators with improved finite sample properties. Journal of Econometrics, 29(3):305-325, (1985).

[13] D. A. Ryndyk, R. Guti rrez, B. Song, and G. Cuniberti. Green Function Techniques in the Treatment of Quantum Transport at the Molecular Scale. Energy Transfer Dynamics in Biomaterial Systems (2008)

[14] C. J. Lambert, V. C. Hui, S. J. Robinson. Multi-probe conductance formulae for mesoscopic superconductors. J. Phys.: Condens. Matter 5 (1993).

[15] I. M. Grace, S. W. Bailey, C. J. Lambert, and J. H. Jefferson. Molecular Nanowires and Other Quantum Objects. NATO ASI Series, pages 13-21, (2004).

[16] S. Athanasopoulos. Electronic Properties of Hybrid Carbon Nanotubes. PhD thesis, Lancaster University, (2005).

[17] M. Leadbeater and C. Lambert. Superconductivity-induced phase-periodic transport in nanoscale structures. Physical Review B, 56(2):826-831, July (1997).

[18] J. Koltai, J. Cserti, and C. Lambert. Andreev bound states for a superconducting-ferromagnetic box. Physical Review B, 69(9):3-6, March (2004).

[19] P. Polin_ak, C. Lambert, J. Koltai, and J. Cserti. Andreev drag effect via magnetic quasiparticle focusing in normal-superconductor nanojunctions. Physical Review B, 74(13):2-5, October (2006).

[20] T. Pope. Quantum and Classical Dynamics of Molecular-Scale Junctions. PhD thesis, Lancaster University, (2013).

Chapter 4

4.1 Quantum interference and heteroaromaticity of para- and meta-linked bridged biphenyl units in single molecular conductance measurements

4.2 Introduction

This study aims to understand the effect of the heteroatom which is the bridge atom linking two benzene rings and the role it plays in the quantum interference through these structures. We study how this quantum interference combined with connectivity alters the conductance by changing the anchor groups between *para-para* linked and *meta-meta* linked. Generally, meta-linked electron donor–acceptor molecules have weaker electronic coupling in the ground state compared to those that are para-linked, whereas the excited-state electronic coupling of meta-linked molecules is comparable to or larger than that of para-linked molecules. More generally, the meta effect is one manifestation of a broader class of quantum interference effects that are readily observed in both conjugated and cross-conjugated systems [1]. Quantum interference (QI) effects have attracted much attention through theoretical and experimental approaches. Both constructive and destructive QI are found in the different systems. For example, a molecule with two parallel electron transmission paths with no phase shift can lead to constructive interference with a larger conductance, while the conductance of molecular junction with meta-substituted benzene ring is lower than that with para-substituted benzene ring by several orders of magnitude, due to destructive QI [2].

The measurement and understanding of charge transport in single molecules is of fundamental interest and is relevant to the proposed future applications such as diode, transistor, sensor and solar cell of molecules in electronic devices [3–8]. Many studies have addressed correlations between molecular structure and transport properties of molecules wired into gold–molecule–gold nanoscale junctions [9,10]. Several experimental approaches are well established for measuring transport through single (or a few) molecules, notably the mechanically controlled break junction (MCBJ) [11] and scanning tunneling microscopy-break junction (STM-BJ) techniques [12]. Combined experimental and theoretical studies [13] have established that charge transport through molecular junctions is controlled by the intrinsic properties of the molecular backbone, the terminal anchoring group, and the metal leads. Key features are the molecular length, the molecular conformation, the gap between the highest occupied and the lowest unoccupied molecular orbitals (the HOMO-LUMO gap), the alignment of this gap to the Fermi level of the metal electrodes, and the coordination geometry at the metal-molecule contacts. Oligo (arylene-ethynylene) (OAE)-type molecular wires have been widely explored in single molecular junctions [14–18]. They are π–conjugated, rod-like molecules and their functional properties can be systematically tuned over a wide range of parameters by chemical synthesis [19].

In the present work we investigate a series of ten OAE molecules **1–10** whose structures are shown in Figure 4.1. The molecular design combines three key structural features: (i) all of the molecules have terminal pyridyl anchoring units at both ends; (ii) each molecule has one of five different core units and (iii) there is either para-para or meta-meta conjugation through the core unit, providing two isomeric series. The dibenzothiophene (**1-*Sp*, 6-*Sm***), N-ethylcarbazole **(2-*Np*, 7-*Nm***), dibenzofuran (**3-*Op*, 8-*Om***) and 9,9-dimethylfluorene cores (**4-*Cp*, 9-*Cm***) are rigid and planar. Heteroaromaticity, i.e., the resonance energy (is a way of describing delocalized electrons within certain molecules [48]), will decrease in the sequence dibenzothiophene > carbazole > dibenzofuran, reflecting the extent of delocalization of a lone pair from the heteroatom into the π–system of the central ring **(S > N > O**) [20]. Fluorene, with no heteroatom and a bridging sp3 carbon atom instead, has a non-aromatic central ring. In contrast to the other molecules in Figure 4.1, biphenyl derivatives **5** and **10** possess a flexible and twisted core. It is well known that increasing the torsion angle within a biphenyl unit leads to reduced single-molecule conductance (The orbital overlap of π systems decrease with increaseφ) [21–25], therefore, **5** and **10** are studied here as model compounds.

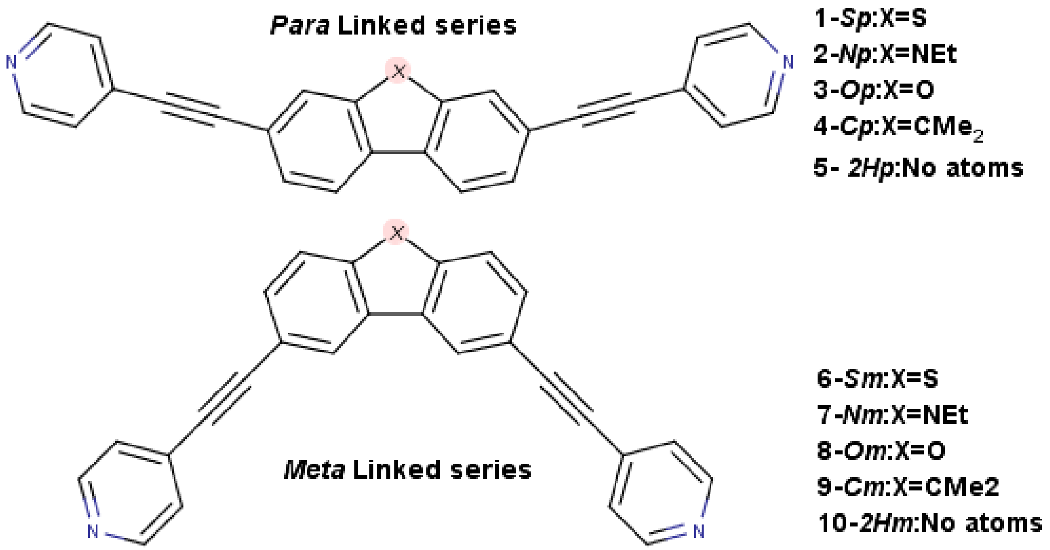

Figure 4.1 Structures of the molecules discussed in this work and their nomenclature. The structures represent the para-linked series **1–5** (top) and meta-linked series **6–10**(bottom)

We are aware of only two related reports on the effect of heteroaromaticity on single-molecule conductance. Venkataraman, Breslow and co-workers studied three amine-terminated molecules comprising thiophene, furan and dimethylcyclopentadiene cores (11–13, Figure 4.2). Based on STM–BJ measurements the authors concluded that aromaticity in the core leads to a decrease in the single-molecule conductance, i.e. the non-aromatic cyclopentadiene derivative 13 has the highest conductance, while the most aromatic thiophene derivative 11 has the lowest conductance [26]. This work did not consider the linkage of the anchor units to different positions on the core.

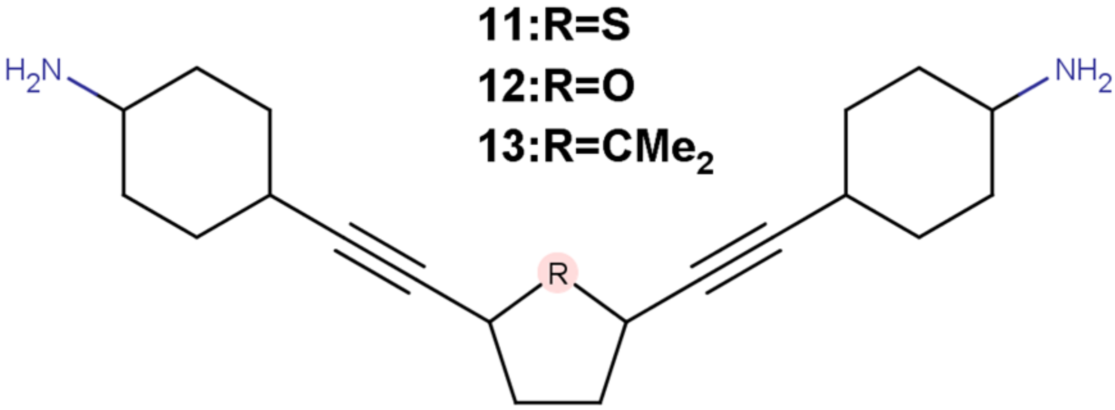

Figure 4.2 Molecules studied in reference [26]. Amine-terminated molecules 11–13 measured by STM-BJ.

A second study concerns multiple pathways through a molecular wire based on fluorene-like molecules [27]. Several studies have established that para (conjugated) connectivity through a core unit results in enhanced conductance compared to the isomeric *meta* (reduced conjugation) connectivity. This is ascribed to quantum interference and has been observed experimentally and theoretically in aromatic rings such as benzene [28–31], naphthalene [16], anthracene [16], pyrene [32] and anthanthrene [33].

The motivation for the present work is to study for the first time the combined effects of two important molecular parameters on the single-molecule conductance of molecular wires: (i) heteroaromaticity in the core of the wire, and (ii) para versus *meta* conjugation through the core unit.

4.3 Results

Single-molecule Conductance Measurements. Single-molecule conductance measurements of **1–10** in molecular junctions were performed by collaborators in the group of Wenjing Hong using a home-built mechanically controllable break junction (the conductance measurement in single-molecule junctions were studied using MCBJ, in nonconductive solution and at room temperature. The MCBJ experiments are based on the opening/closing of nanogaps formed by notching a freely suspended, horizontally supported gold wire) (MCBJ) setup at a bias V_{bias} = 0.1 V. Figure 4.3a shows typical individual conductance G (in units of quantum point conductance $G_0=2e^2/h$, corresponding to perfect transmission of electrons from left to the right electrode, through the point contact. Therefore, the conductance of a molecule given in units of G_0 tells us how conductive the molecule is in comparison with a metal atom [4]) versus distance (Δz) stretching traces in the measurement of ***Np***. The conductance in the molecule-free traces (black line) reveals exponential decrease characteristics upon the stretching process. When molecule ***Np*** is present a pronounced conductance plateau around 10^{-5} G_0 could be detected (green line) after the Au–Au contact breaks, which is assigned to the gold–molecule–gold junction. Since the break junction method can create a large number of molecular junctions with different molecule–electrode contact geometries, more than 1000 curves were recorded for statistical analysis to determine the most probable conductance of the molecular junctions. We further introduced a relative distance (Δz) and defined $\Delta z = 0$ at 0.5 G_0 to align all the traces. This procedure leads to an accurate alignment of the conductance−distance traces because of the sharp drop in conductance at $G < G_0$. The electrode separation z_{exp} is then estimated by $z_{exp} = \Delta z + \Delta z_{corr}$, where Δz_{corr}

= 0.5 ± 0.1 nm corresponds to the "snap-back" nanogap which forms immediately upon breaking of the gold-gold atomic contact [34]. The all–data two–dimensional (2D) histogram (Figure 4.3b) exhibits features of gold–gold contacts around G ≥ 1 G0, followed by another well-defined conductance scatter group in the range of 10^{-4} G0 ~ 10^{-6} G_0 which is attributed to the formation of single–molecule junctions. Figures 4.3c-d demonstrate the comparison between molecules with different heteroatoms and anchoring positions. For the compounds **1–3** with the para–para connectivity, the conductance clearly increases in the sequence **Sp < Np < Op**. However, for the isomers **6–8** where the anchoring groups are attached at meta–meta positions, the conductance reveals a different trend, **Sm ≈ Om < Nm**. Control experiments using analogues with a carbon bridge (**4-*Cp* and 9-*Cm***) and without any bridging atom (**5-*2Hp* and 10-*2Hm***) were also conducted. The conductance of 2Hm could not be measured within the detection range ($\geq 10^{-7}$) of our setup. This can be explained by the *meta* coupling combined with a non-planar biphenyl core giving a conductance value below the direct tunneling conductance [31]. Furthermore, some of the measured conductance histograms have more than one peak, this feature usually appears with the bipyridine anchor groups, with low and high conductance values. The low and high conductance is usually attributed to the different binding geometries these types of contacts form [42].

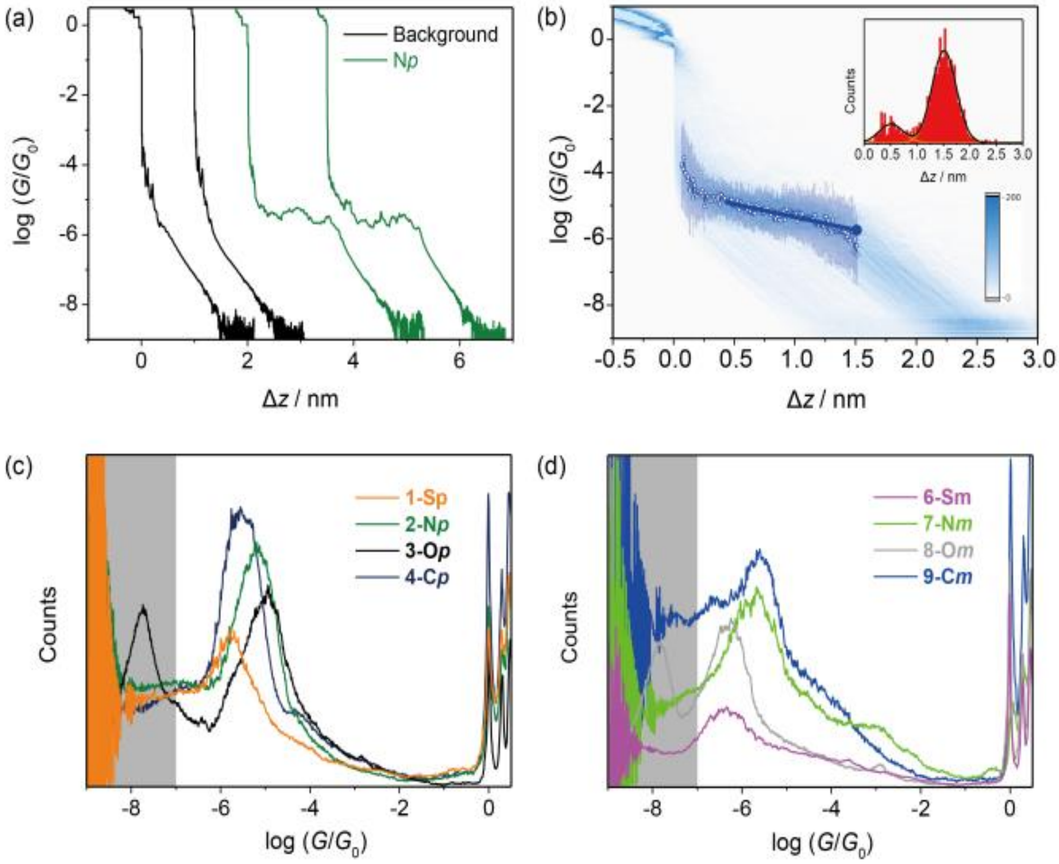

Figure 4.3 Single-molecule conductance results from MCBJ experiments. (a) Typical individual conductance–distance traces (horizontally offset for clarity) of Np (green) and pure tunneling traces (black). (b) All-data-point 2D conductance versus relative distance (Δz) of Np. In 2D histogram, statistically averaged conductance−distance traces (hollow circles) with variations indicated by the standard deviations (bars) are shown, along with the linear fit (line). The solid circle represents the last data point in the linear fit before junction rupture. Inset: Stretching distance distribution obtained between $10^{-0.30}$ G_0 and $10^{-6.25}$ G_0. (c) and (d) All-data-point 1D conductance histograms constructed from more than 1,000 MCBJ traces of molecules with anchoring groups on (c) para-para and (d) meta–meta position. The gray area represents the detection limit of the MCBJ set up at 10^{-7} G_0.

As the junction configuration is known to have a significant effect on the single–molecule conductance, we further explored the master curves composed of the fitted conductance with standard variation at each cross-sectional distance point [35]. After a linear fitting, the *Np* junction conductance with a fully stretched molecular conformation before the junction rupture can be deduced as $10^{-5.74 \pm 0.17}$ G_0, which should be closer to the theoretical predicted configurations.

Table 4.1 Most Probable Conductance Values as Obtained from MCBJ Experiments and Computations DFT.

Compound	MCBJ ($\log(G/G_0)$)		DFT ($\log(G/G_0)$)	$G_{Spara}–G_{Smeta}$ ($\log(G/G_0)$)	JFP (%)	Electrode separation $z_{exp}=\Delta z+\Delta z_{corr}$ (nm)	Theoretical length (nm)
	$G_{Gaussian}$	$G_{stretched}$	G	MCBJ			
1-S*p*	–5.79±0.30	–5.93±0.16	–5.50	0.72	69	2.04 ± 0.45	2.04
2-N*p*	–5.22±0.40	–5.74±0.17	–5.15	0.67	83	2.01 ± 0.23	2.02
3-O*p*	–5.04±0.47	–5.47±0.22	–5.10	1.37	99	1.92 ± 0.26	2.03
4-C*p*	–5.55±0.44	–5.81±0.12	–5.44	0.09	70	1.84 ± 0.22	2.03
5-2H*p*	–5.4 ± 0.36	–5.68±0.11	–5.30	>1.32	83	2.11 ± 0.23	2.08
6-S*m*	–6.34±0.47	–6.65±0.35	–6.34		100	1.64 ± 0.29	1.51
7-N*m*	–5.76±0.48	–6.41±0.25	–6.06		71	1.66 ± 0.14	1.56
8-O*m*	–6.32±0.38	–6.84±0.24	–6.40		100	1.65 ± 0.19	1.55
9-C*m*	–5.26±0.82	–5.90±0.39	–5.74		100	1.46 ± 0.29	1.51
10-2H*m*	< –7	< –7	–7.38		–	–	1.41

It is found that there is some difference in the conductance comparison among different molecules: ***Om*** shows lower conductance than ***Sm*** for the conductance of the fully-stretched configurations, while ***Om*** shows a slightly higher conductance for the most probable conductance extracted from conductance histogram.

The key results of the MCBJ measurements are summarized in Table 4.1 and the corresponding original results are presented in the (Figures 4.4-4.5). No multiple features were observed in the experiments, including **3-*Op*** and **8-*Om***. The lower peaks covered by the grey area below 10^{-7} G_0 is the noise level of the MCBJ experiments (Figure 4.3(c and d)). All the curves were used for the statistical analysis without any data selection. Junction formation probability (JFP) is the proportion of molecular stretching traces with a pronounced plateau relative to the total number of traces (Table 4.1). It is judged by area ratio of the peak in the plateau length distribution. Direct tunneling traces have no plateau and decay faster to the noise level, corresponding to the smaller stretching peak alongside the molecular peak in the plateau length histogram. (Figures 4.4-4.5).

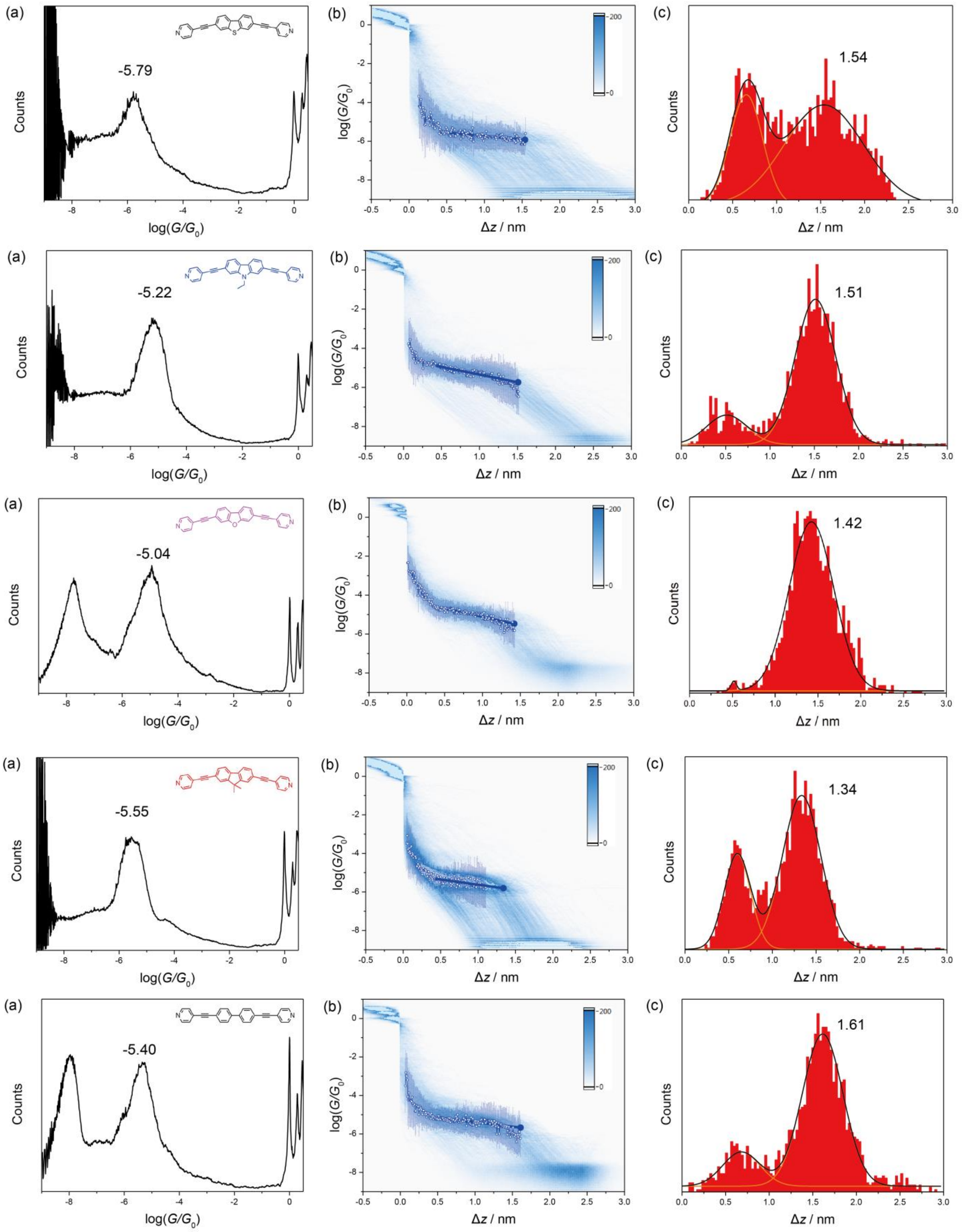

Figure 5.4. (a) 1D conductance histogram, (b) 2D histogram and (c) characteristic

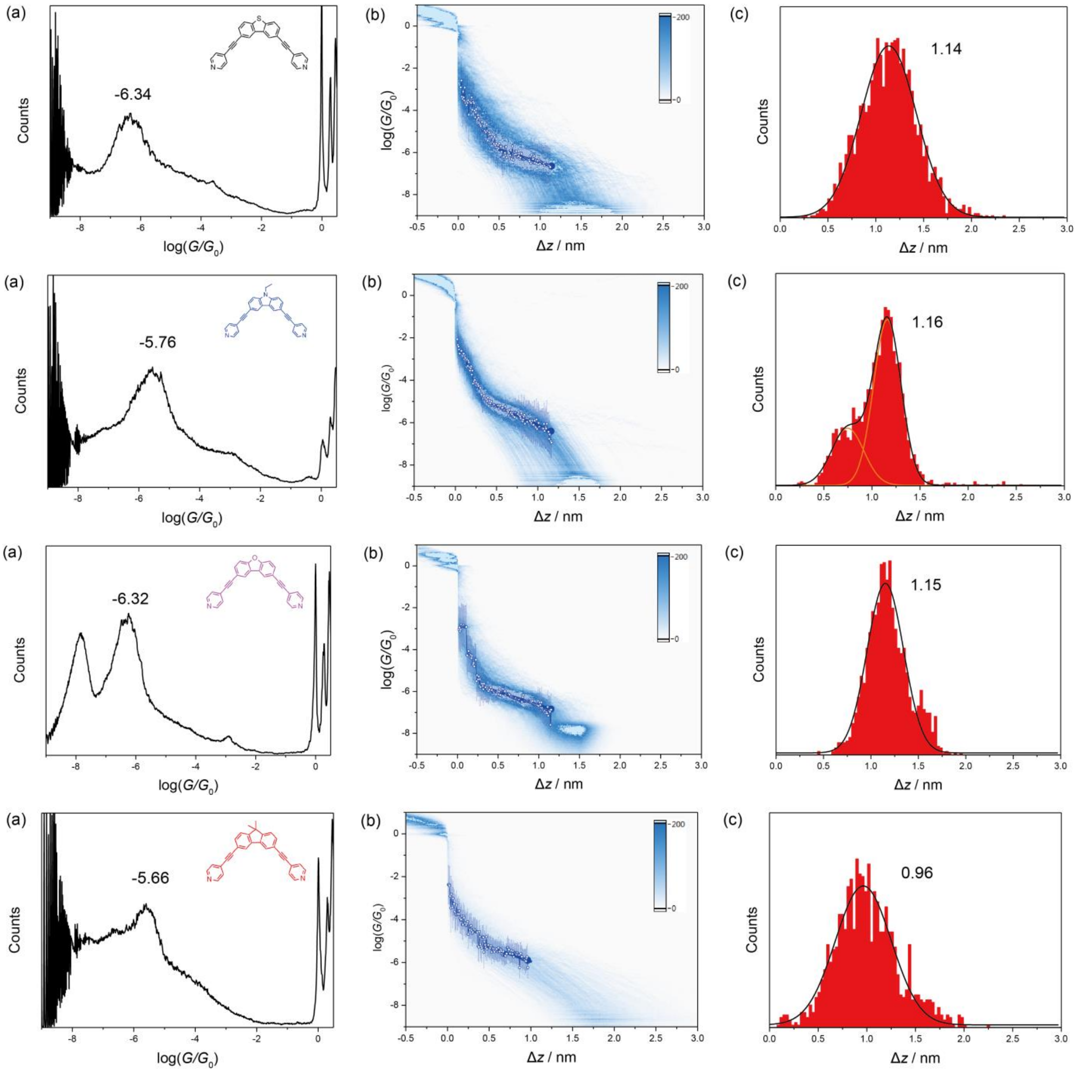

Figure 5.5. (a) 1D conductance histogram, (b) 2D histogram and (c) characteristic

Several interesting conclusions can be drawn from the comparative conductance values of these molecules. First, in all cases, molecules with para connectivity **1–5** present larger conductance values than their *meta* isomers, regardless of the bridging unit. This can be attributed to the partial de Broglie waves traversing in different paths through the core being in phase in the para isomers, giving rise to a constructive quantum interference (QI) effect. On the contrary, in the meta-anchored isomers the waves are out of phase leading to destructive quantum interference. The conductance relationship of the para and meta molecules is consistent with that of molecules with a central single benzene ring [29–31,36], indicating the quantum interference effect can still operate in polycyclic compounds. Secondly, the structure of the central core plays an important role in the conductance of QI molecules. It is noted that the largest difference between the para– and meta–anchored molecules (ΔG) is for the dibenzofuran pair ***3-Op*** and ***8-Om***, 1.37 $\log(G/G_0)$. However, as we reported previously, the differences between para and meta linked molecules are nearly 1.50 $\log(G/G_0)$ in benzene-cored analogs[31]. The lower experimental differences in the present study demonstrate that the quantum interference effect has not been amplified, and is even slightly reduced, by bridging the two benzene rings with a five-membered ring. Additionally, differences of the conductance in fully-stretched conformations between para– and meta–anchored molecules follow the increasing order of **ΔGC < ΔGN < ΔGS < ΔGO**, illustrating that the heteroatom can also contribute to the expression of the quantum interference. The electrode separations (z_{exp} in Table 4.1) are in good agreement with the theoretical molecular lengths. This indicates that in the fully stretched configuration, the molecular junctions are primarily linked by the gold–nitrogen bonds.

Moreover, there is no distinct correlation between the plateau length (or JFP) and the nature of the bridging atoms (S, N, O or C), demonstrating that these atoms have no significant influence on the conformation of the molecular junction. Furthermore, I did not observe any additional conductance group during the experiments for the ten molecules. I attributed this fact to three reasons. Firstly, pyridyl-terminated compounds have been reported to show well-defined peaks in the conductance histograms resulting from the high directionality of the donor-acceptor binding between N lone pair and Au [17,37,38]. Secondly, the alkyl groups connected to the bridged atom (N and C) sterically hinder the interaction between the electrode and the core of the molecule as well as restricting any π-π interaction of two molecules. Thirdly, molecules with similar core structures have been reported [21,24,25] to exhibit only one conductance statistical peak, suggesting that the junction formed by the core of the molecule is not robust enough during the elongation process. In the control experiments with 5-*2Hp* and 10-*2Hm*, however, we observed such an obvious difference that the conductance of 5-*2Hp* is higher than that of 10-*2Hm* by almost two orders of magnitude.

4.4 Theory and Simulations.

The density of state (DOS) represents the number of electronics states in a band per unit energy, the density of states could be calculated from $D(E) = \sum_i \delta(E - \varepsilon_i)$ where ε_i is the eigenvalues of a system and δ is Kronecker delta. The DFT calculated of DOS spectra for the isolated molecule versus energy, present in figure 4.6, the gap ‘’the value of gap in DOS, which is the gap in between first onset of electron density from the right and left side’’ between HOMO LUMO peaks about 3.5 eV for both meta and para linked.

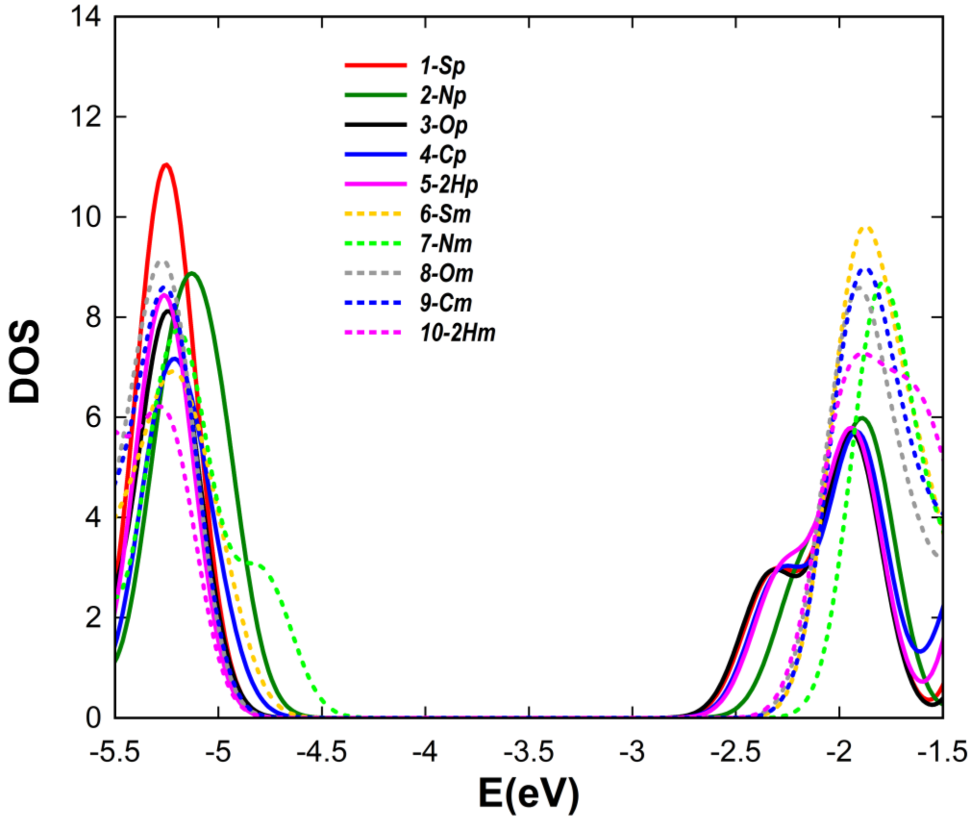

Figure 4.6 density of state versus energy for para end meta calculated by DFT, in the gas phase.

4.5 Binding Energy.

To calculate the optimum binding distance for a **1-*Sp*** molecule between two gold (111) surfaces we used the SIESTA implementation of DFT and the counterpoise method, which removes basis set superposition errors (BSSE). The binding distance z is defined as the distance between the gold surface and the molecule (**1-*Sp***) at the closest point. **1-*Sp*** is defined as monomer A and the gold electrodes as monomer B.

The ground state energy of the total system is calculated using SIESTA and is denoted E_{AB}^{AB}, with the parameters defined as those in the "Theory and Simulation" section of the main text. The gold leads consist of 6 layers each containing 25 atoms. The energy of each monomer is then calculated in a fixed basis, which is achieved by the use of ghost atoms in SIESTA. Hence the energy of the individual molecule **1-*Sp*** in the presence of the fixed basis is defined as E_A^{AB} and for the gold is E_B^{AB}. The binding energy is then calculated using the following equation:

$$\text{Binding Energy} = E_{AB}^{AB} - E_A^{AB} - E_B^{AB} \qquad 4.1$$

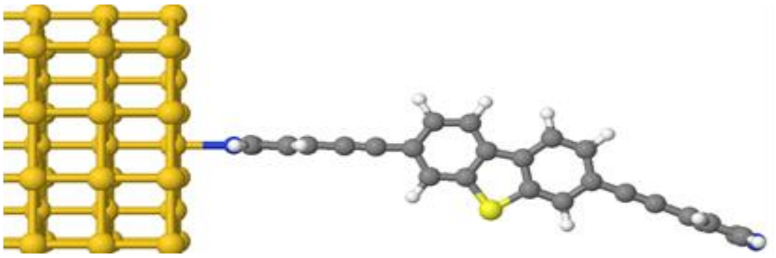

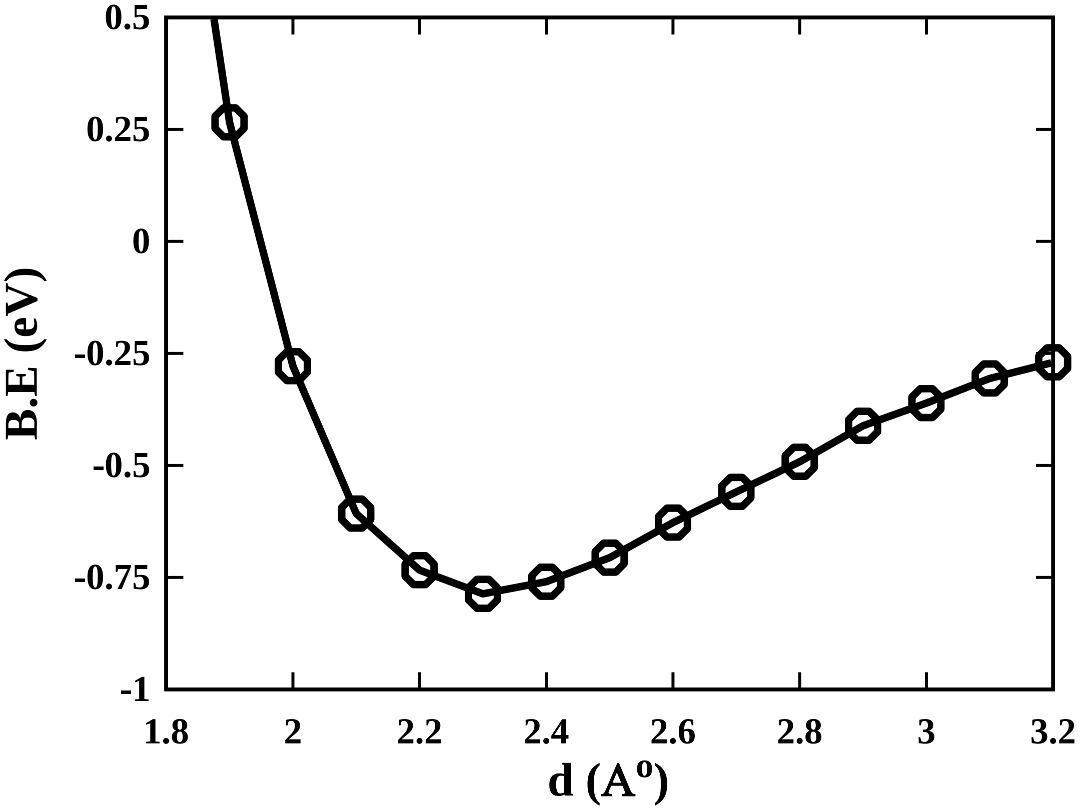

Figure 4.7. Binding energies as a function of the distance (Å) of the nitrogen from the electrode surface (lower). Examples of binding geometries on a flat electrode and an electrode containing an adatom (above).

To understand the effect of pendant groups on quantum interference in the molecules of Figure 4.1, I first consider their two tight-binding representations shown in Figure 4.8, connected to 1-dimensional external leads.

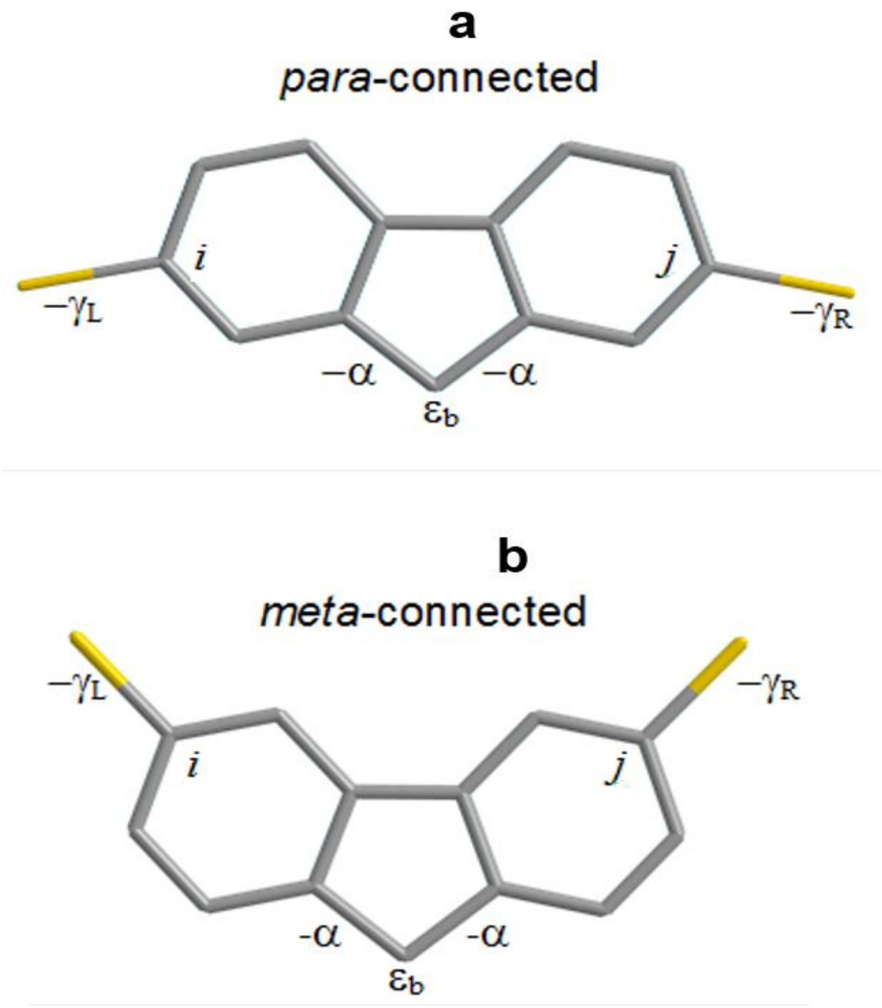

Figure 4.8 Tight-binding (i.e. Hückel) models of *para*-(a) and *meta*-connected (b) molecules. Within the core of each, all site energies are zero except the pendant site energy ε_b and all nearest neighbour bonds are equal to –1, except for those denoted as α. The weaker couplings between the molecule and left leads are $-\gamma_L = -0.08$ at atom number *i* and right leads $-\gamma_R = -0.08$ at atom number *j*.

The tight binding model is introduced to illustrate the underlying trends in the transmission function and to allow us to obtain an analytic formula as described in section 4.8. Figure 4.9 shows results for various values of alpha, to reveal the evolution of the transmission curves with increasing coupling to the pendant groups. In Figure 4.11a, to use the simplest possible description, the same value of alpha = 1 is used for all molecules (for more information Table 4.2). When $\alpha = 0$, the pendant orbital is decoupled from the central core. Since the latter is a bipartite lattice, in the meta case, destructive interference should occur at the centre of the HOMO–LUMO gap (i.e. E = 0) [13,32,33]. The black curves in Figure 4.9 show the resulting transmission coefficients T (E), when $\varepsilon_b = 0$. The other curves in Figure 4.10 show how the transmission coefficient evolves as the coupling α to the pendant orbital is increased from zero (black curves) to unity (red curves).

Table 4.2. Comparison between experimental conductances (column 2) and theoretical values. Columns 3-6 show DFT-GOLLUM results obtained at different Fermi energies (relative to the DFT-predicted Fermi energy). Column 7 shows the conductance obtained from the tight binding model by choosing values of ε_b, which yield closest agreement with experiment. Where $\alpha = -1$, $\gamma_L = \gamma_R = -0.08$

Compound	MCBJ (log(G/ G_0))	Tight-binding conductance	ε_b	Mulliken charge	Electronegativity[47]
1-S*p*	–5.79	–5.06	–1.8	6.04	2.58
2-N*p*	–5.22	–5.04	–2.0	4.50	3.04
3-O*p*	–5.04	–5.02	–2.2	5.73	3.44
4-C*p*	–5.55	–5.08	–1.6	3.83	2.55
5-2H*p*	–5.40	–4.99	$\alpha = 0$		
6-S*m*	–6.34	–5.71	–1.8	6.04	2.58
7-N*m*	–5.76	–5.79	–2.0	4.50	3.04
8-O*m*	–6.32	–5.85	–2.2	5.72	3.44
9-C*m*	–5.66	–5.63	–1.6	3.83	2.55
10-2H*m*	< –7	–	$\alpha = 0$		

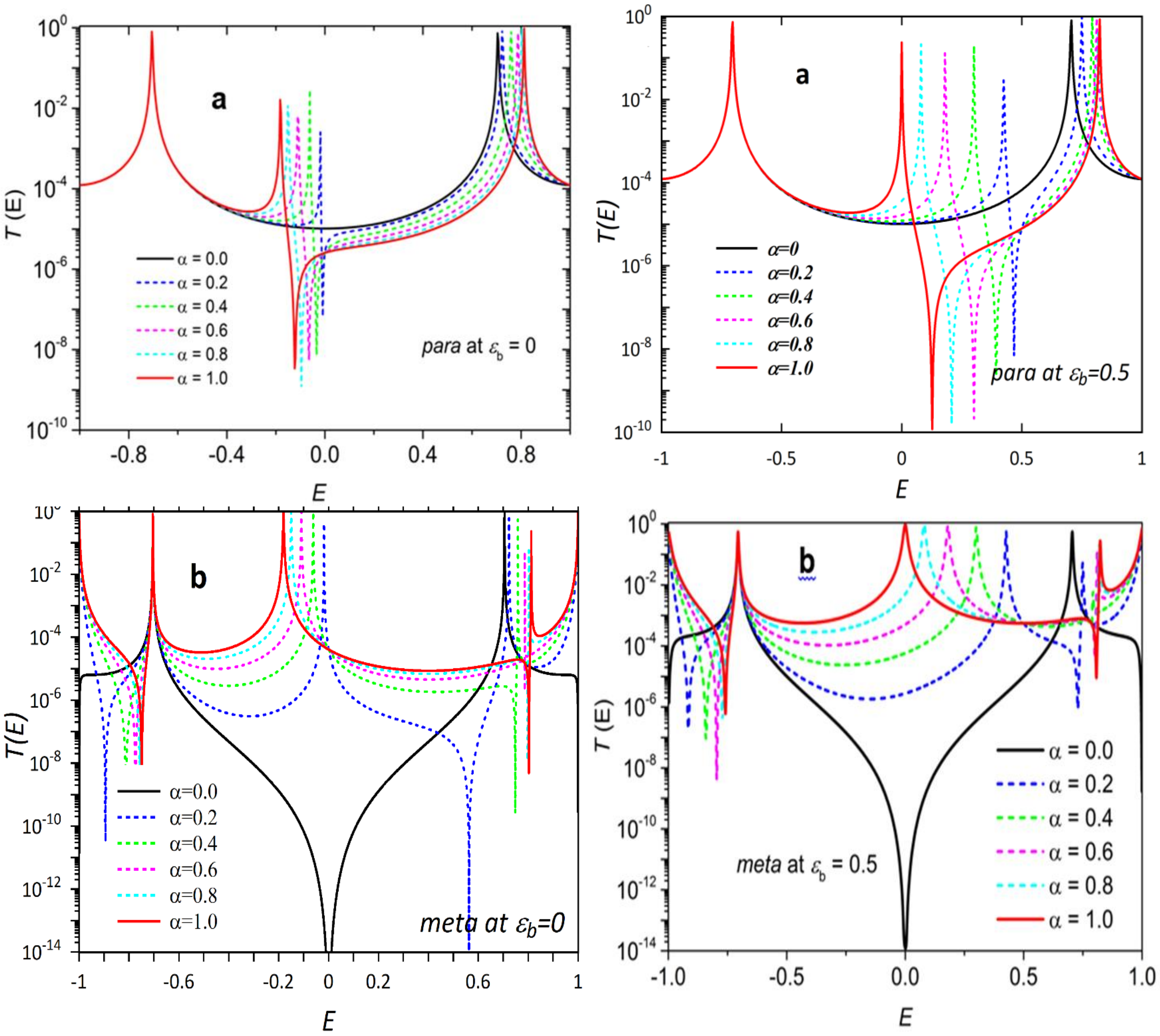

Figure 4.9 T (E) vs. E for different values of α at $\varepsilon_b = 0$. Transmission coefficients T (E) for para-connection (a) , meta-connection (b), when $\varepsilon_b = 0$ left panel and $\varepsilon_b = 0.5$ right panel

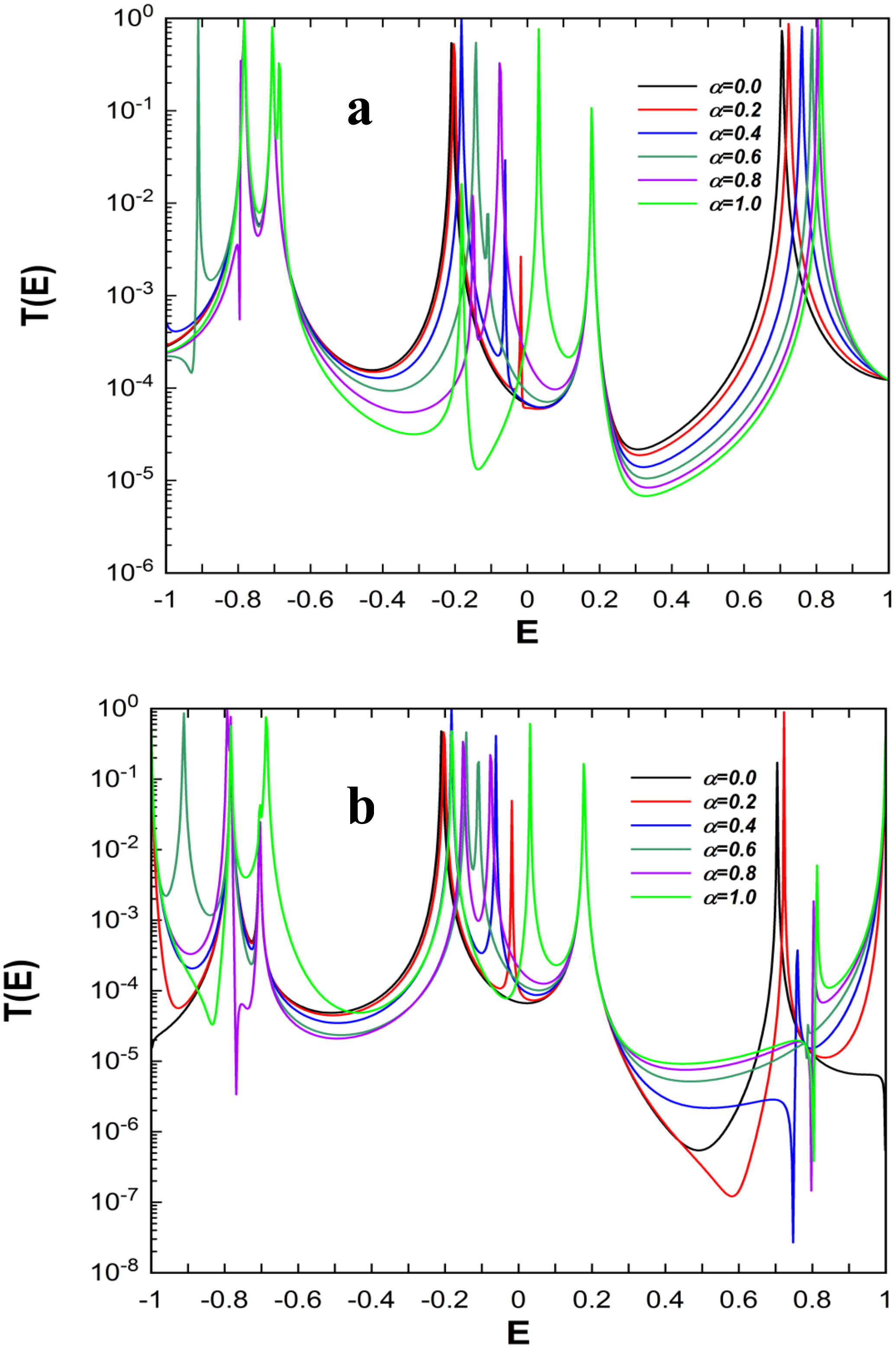

Figure 4.10 T (E) vs. E for different values of α at $\varepsilon_b = 0$. Transmission coefficients T (E) for para-connection (a) , meta-connection (b), when $\varepsilon_b = 0.0$

Fano resonances occur when a bound state is coupled to a continuum of states. For a single molecule connected to metallic electrodes, the continuum of states is supplied by the metal [13]. The appearance of Fano resonances in electron transport through single molecules was recognised in a series of studies of a family of rigid molecules which contained pendant groups [43-45], Ismael and co-worker give specific detail to examine how Fano resonances can be distinguished from other quantum interference (QI) effects in molecules [46]. The above results show that in the absence of pendant groups (i.e. when $\alpha = 0$) the *meta* case shows a sharp transmission dip due to destructive interference at the gap centre, which is absent in the para case. In the presence of pendant groups (i.e. when α is non-zero) this destructive interference is alleviated in the *meta* case. In the para case, the non-zero coupling to the pendant group introduces a new conductance pathway, which can cause destructive interference within the gap, signaled by the Fano lineshape just below $E = 0$. Further examples of this evolution for different choices of ε_b are presented figure 4.9b. For the values of ε_b shown in Table 4.2, Figure 4.11a, shows the resulting tight-binding transmission coefficients. Clearly the tight-binding model captures the qualitative features of the full density-functional calculation of transmission curves shown in Figure 4.11b. In particular the tight-binding result for 2-*Hm*, which does not possess a pendant orbital, shows a pronounced transmission dip near $E = 0$, which is reflected in the low transmission coefficient predicted by DFT. (In the latter case, the presence of non-pi orbitals provides a parallel conductance path, which prevents the transmission coefficient completely vanishing.)

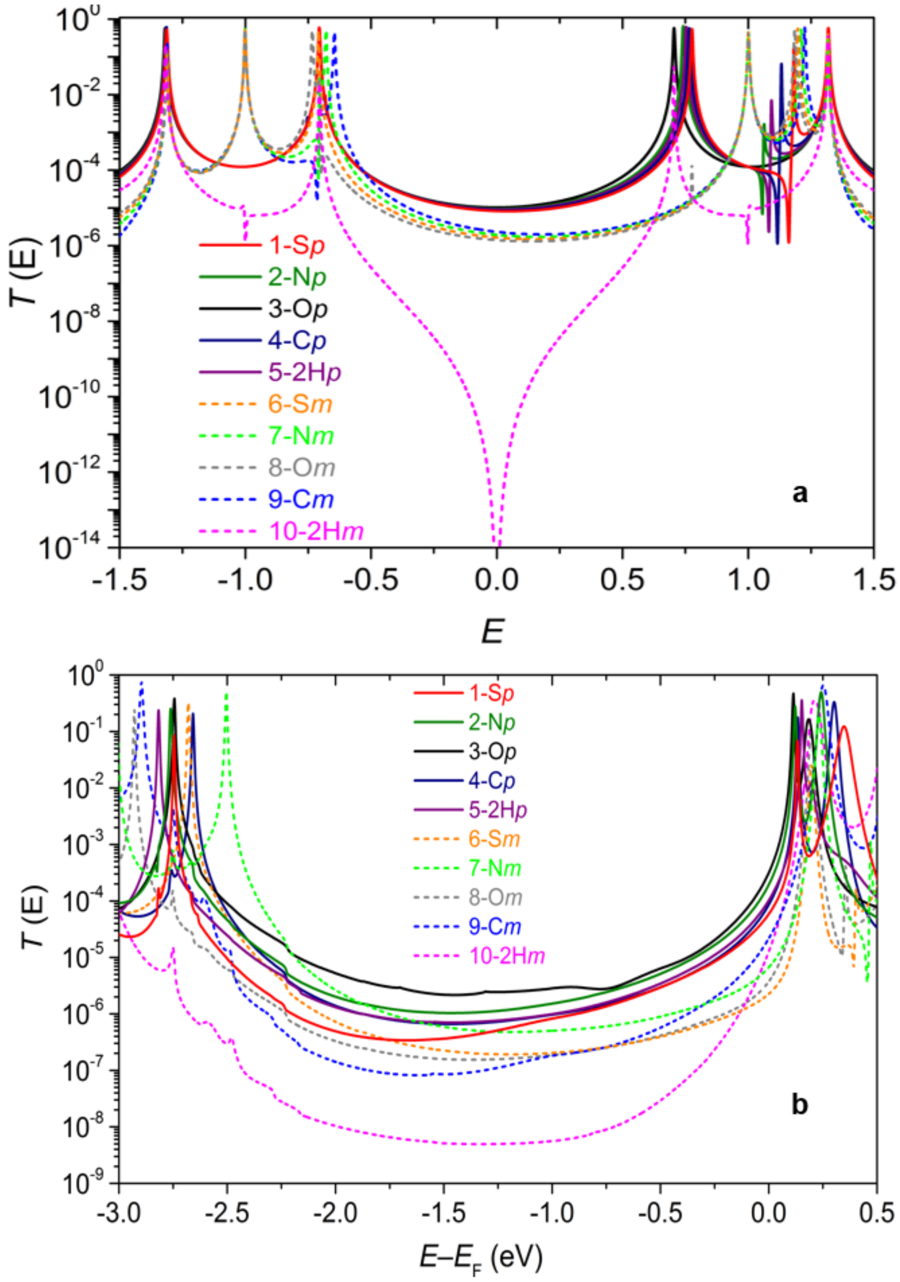

Figure 4.11 Transmission coefficients. Results for the tight-binding (Hückel-model) transmission coefficients (a) obtained using the parameters in Table 4.2. The transmission coefficients (b) obtained for electrodes with adatoms (see figure 4.10b) using density functional theory combined with Gollum.

The electronic interference structure calculations leading to transmission curves (Figure 4.11b) were performed using the DFT code SIESTA [39]. The optimum geometry of the isolated molecules was obtained by relaxing the molecules until all forces on the atoms were <0.05 V/Å. The SIESTA calculations employed a double-zeta plus polarization orbital basis set, norm-conserving pseudopotentials, an energy cutoff of 200 Rydbergs defined the real space grid and the exchange correlation functional was Local Density Approximation (LDA) [40].

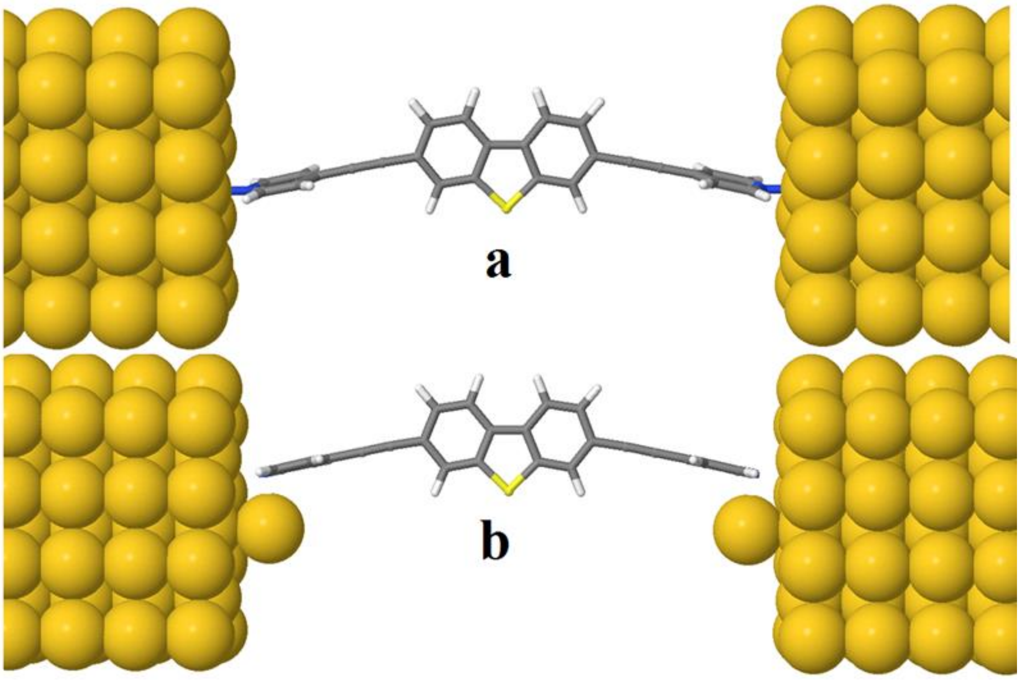

Figure 4.12 Geometry of the molecular junction containing a *1-S* wire (a) on flat electrodes (b) on electrodes containing adatoms.

To calculate the conductance through these two groups of molecules, para and *meta* shown in Figure 4.1, they were attached to gold leads via the pyridyl anchor groups. The leads were constructed of 6 layers of (111) gold each containing 25 gold atoms. Transport calculations were carried out both for flat electrodes and for electrodes containing adatoms, as shown in Figure 4.12. According to DFT, the molecule binds most favourably to a top site, with a binding energy of about -0.8 eV at a distance of 2.3 Å (Figure 4.7) between the terminal nitrogen atoms and a 'top' gold atom. This most-favourable binding geometry has been used in all simulations. A Hamiltonian describing this structure was produced using SIESTA and the zero-bias transmission coefficients T(E) were calculated using the Gollum code [41]. An excellent agreement between theoretical and experimental conductance values has been obtained (Figure 4.15), by choosing a Fermi energy of EF = –0.5 eV relative to the DFT-predicted value. Figure 4.11 shows that the transmission coefficients of *meta*-connected molecules are all lower than those of para connected molecules over a wide energy range within their HOMO–LUMO gaps, in agreement with a tight-binding model of pi-orbital transport. In the latter case, in the absence of bridging atoms (5-*2Hp* and 10-*2Hm*) there appear sharp transmission dips due to destructive interference in the *meta* case, which are alleviated by the presence of pendant groups. In contrast, in the para case, constructive interference in the pi-channel is preserved in the presence of bridging atoms. Furthermore σ channel shows there are no dips in the transmission for both *meta* and *para* linked as shown in figure 4.10. On the other hand, in the DFT-based transmission curves perfect destructive interference is masked by the presence of sigma orbitals, which provide a parallel path for conductance.

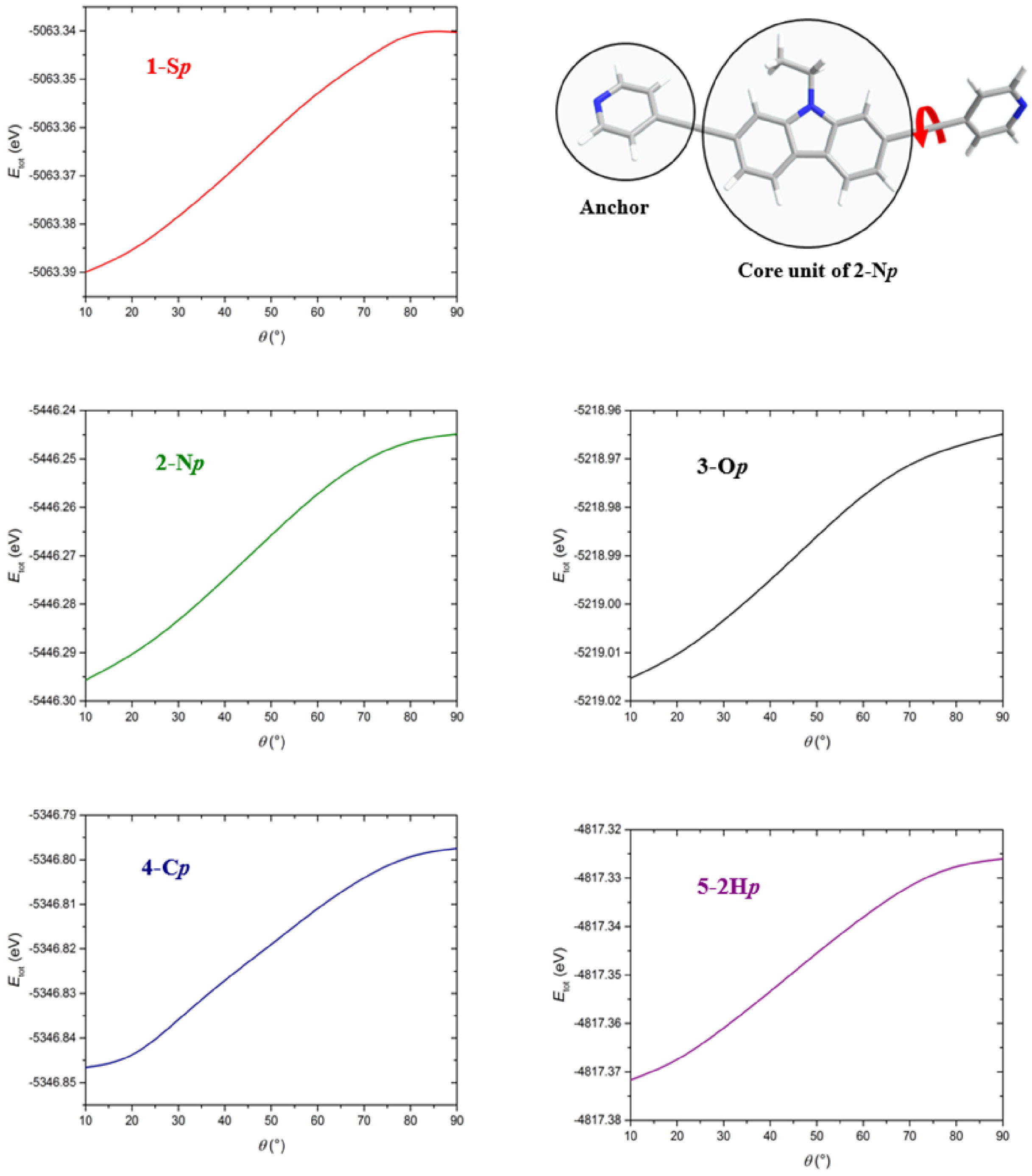

Figure 4.13. Total energy versus angle rotation of anchoring groups with respect to the central unit of para-linked molecules

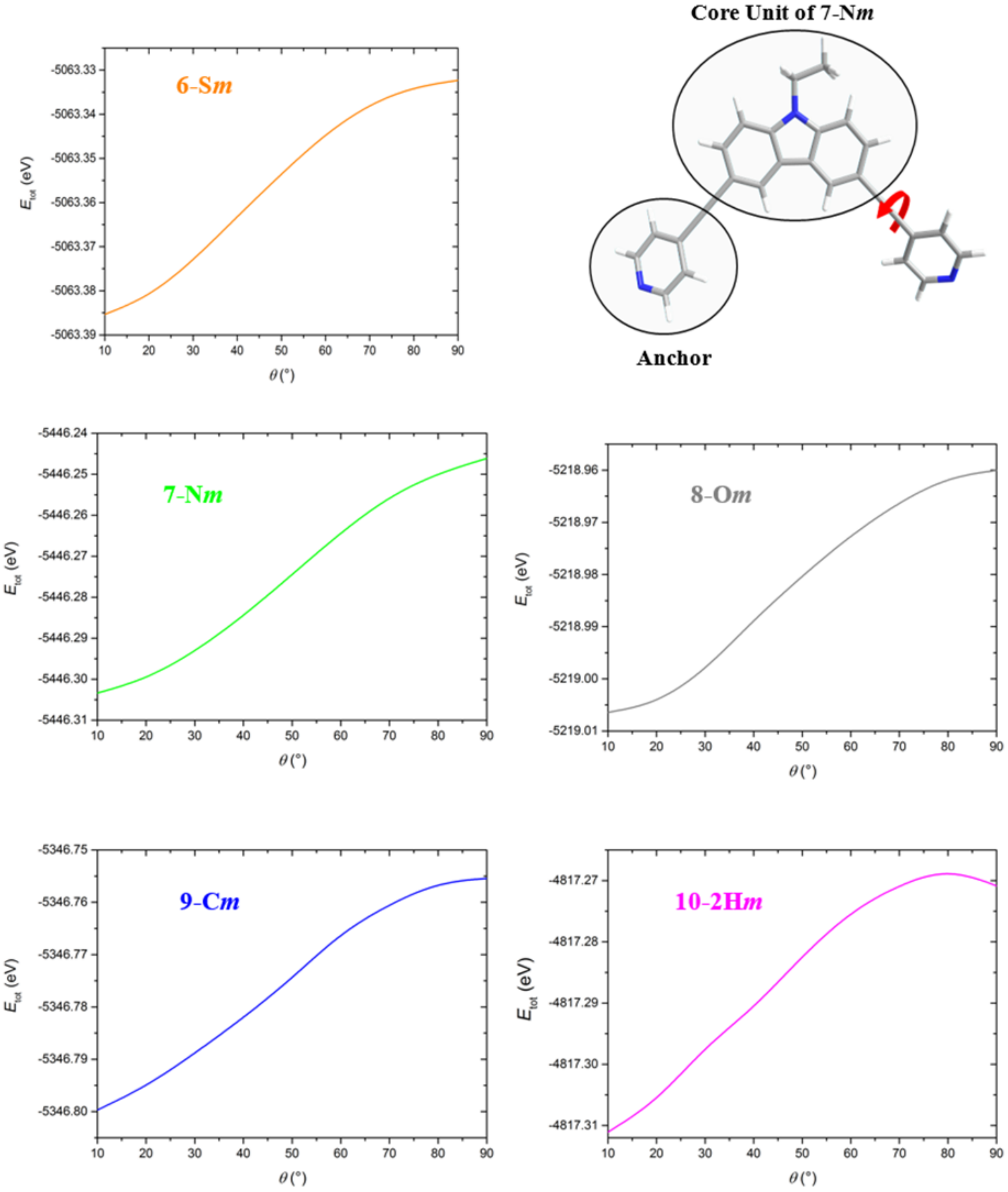

Figure 4.14. Total energy versus angle rotation of anchoring groups with respect to the central unit of meta-linked molecules.

Figure 5.13 and 5.14 are shown the total energy with respect to the angle of anchored group for isolated system this is predicting the angle between anchored and backbone of each molecule in both case para and *meta*, the different between 0° and 90° are less than 0.025 eV (energy at room temperature) for all molecules. In this work I used 90° to find transmission coefficient T(E).

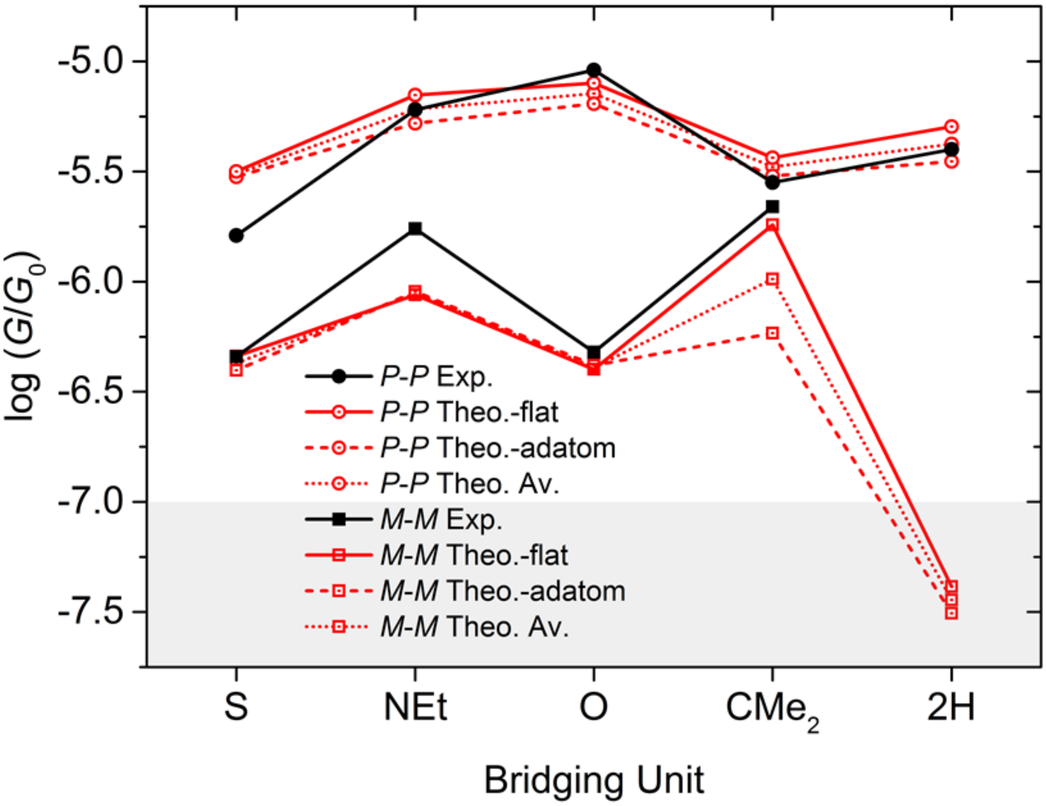

Figure 4.15 Comparison between theoretical and experimental data for most probable conductance values. DFT results are shown for both flat electrodes (solid red lines) and with electrodes containing adatoms (dashed red lines). The dotted lines show the average of the 'flat' and 'adatom' DFT conductances. Although there are differences, we conclude that the same qualitative trends are obtained using both geometries, with the exception of CMe_2, which in the presence of adatoms, no longer has an anomalously high conductance observed experimentally in the meta case 9-Cm.

4.6 Discussion

I conclude, therefore, from our experimental and theoretical data for the para series 1–4 and the *meta* series **6–9**, that there is a clear correlation between aromaticity of the central ring when heteroatoms are present and the single-molecule conductance value in the para series. Aromaticity follows the sequence: **S > NEt > O > CMe2**. Our conductance trend for the heterocyclic para series, i.e. **O > NEt > S** is in agreement with a previous experimental study by Venkataraman, Breslow, et al[24] on monocyclic core units (furan > thiophene) (Figure 4.2). However, the fluorene derivative ***4-Cp*** (which does not have a heteroatom in the core) shows a lower conductance than ***2-Np*** and ***3-Op*** although it exhibits a non-aromatic core. The reason for this exceptional behaviour of ***4-Cp*** is not clear. However, I note that other workers [23–25] have observed that the single-molecule conductance of fluorene-based cores do not follow expected trends.

These results demonstrates that a non-aromatic core unit does not necessarily lead to higher conductance since the polycyclic series **1–5** exhibits a clear difference in comparison to the monocyclic series shown in figure 4.2. However, our data show that the sequence is very different in the *meta* series where dibenzothiophene ≈ dibenzofuran < carbazole. Multiple factors (such as quantum interference, aromaticity and electronegativity) and their composite effects should be taken into consideration in explaining the trends in the conductance. Our results show that bridging heteroatoms alleviate destructive quantum interference in the meta-connected molecules. The contribution of electronegativity of the bridging atoms should not be ignored. For the *meta* series dibenzothiophene 6-Sm and dibenzofuran ***8-Om*** represent both extremes. Dibenzothiophene Sm is the most aromatic and therefore it lowers the conductance. As was mentioned above, dibenzofuran **8-*Om*** is the least aromatic core unit. Therefore, based on the conclusions of the series shown in Figure 4.1, **8-*Om*** should be the most conductive molecule. However, the lone pair of oxygen is tightly bonded due to oxygen's high electronegativity, which hinders the delocalization of electrons and decreases the electron density of the conjugated π system in **8-*Om***. The carbazole derivative 7-Nm is the most conductive in this *meta* series because it is less aromatic than dibenzothiophene, but also bears a lone pair which allows transmission through the molecule. The conductance of model non-bridged compound ***5-2Hp*** is reduced because of the dihedral angle between the two phenyl units. Model compound **10-*2Hm*** shows no conductance within the detection limit of the MCBJ setup. This is consistent with the bridging atom of **6-9** planarizing the core, which is essential for raising the conductance in the meta-series.

4.7 Analytical formula *G* of fluorene core

To obtain the core Green's function *G* for the isolated core of figure 4.17, I first consider the case where $\alpha = \beta = 0$. Figure 4.16 . In this case, apart from the isolated site ε_b, the structure consists of two isolated 6-membered rings labelled A and B with Green's functions (equation 4.5).

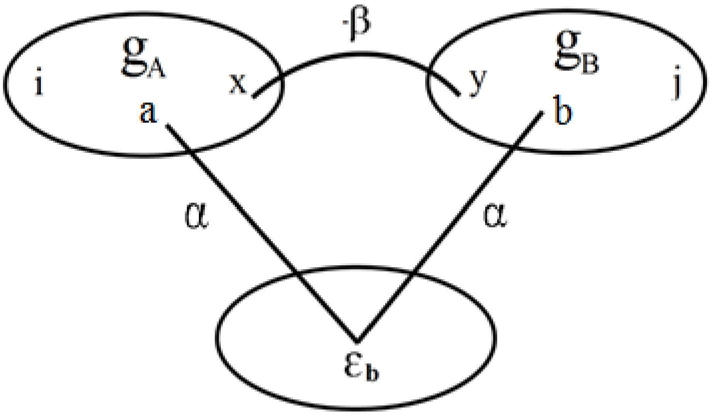

Figure 4.16 An abstraction of the isolated core

$$t = 2isin(k)e^{2ik}\frac{\gamma_L\gamma_R}{\gamma}\frac{G_{ij}}{\Delta} \qquad 4.5$$

As noted in ref [11], the Green's function of the 6-membered rings are given by

$$(g_A)_{ix} = C\cos(k(|i-x|-3))$$

$$(g_B)_{yj} = C\cos(k(|y-j|-3))$$

where i, x are sites belonging to the left ring A and j, y belong to the right ring B and

$$C = \frac{1}{2\gamma\sin(k)\sin(kN/2)}$$

When γ_L and γ_R are non-zero, it is convenient to view the above lattice as an example of the more general structure shown in figure 4.16, in which two subsystems labelled A and B are coupled to each other via sites x, y by a single matrix element $-\beta$ and to a pendant site by $-\alpha$.

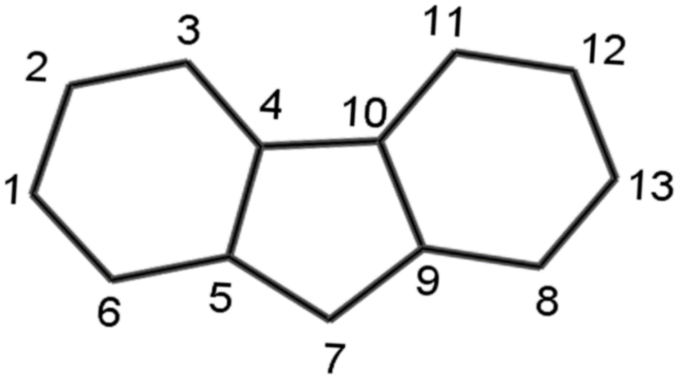

Figure 4.17 The geometry of fluorene core

Then after solving Dyson's equation we obtain,

$$G_{ij} = (\hat{g}_{AB})_{ji} + \frac{\alpha^2}{E - \varepsilon_b - \Sigma}[(\hat{g}_{AA})_{i\,a} + (\hat{g}_{AB})_{i\,b}]\big[(\hat{g}_{AB})_{aj} + (\hat{g}_{BB})_{\,bj}\big] \qquad 4.6$$

Where

$$\Sigma \ = \alpha^2[(\hat{g}_{AA})_{aa} + (\hat{g}_{AB})_{ab} + (\hat{g}_{BA})_{ba} + (\hat{g}_{BB})_{bb}]$$

$$(\hat{g}_{AA})_{ia} = (g_A)_{ia} + \frac{\beta^2\,(g_A)_{ix}(g_B)_{yy}(g_A)_{xa}}{1 - x_A}$$

$$(\hat{g}_{AB})_{ib} = \frac{-\beta\,(g_A)_{ix}(g_B)_{yb}}{1 - x_A}$$

$$(\hat{g}_{AB})_{aj} = \frac{-\beta\,(g_A)_{ax}(g_B)_{yj}}{1 - x_A}$$

$$(\hat{g}_{BB})_{bj} = (g_B)_{bj} + \frac{\beta^2\,(g_A)_{by}(g_B)_{xx}(g_A)_{ya}}{1 - x_A}$$

$$(\hat{g}_{AB})_{ij} = \frac{-\beta\,(g_A)_{ix}(g_B)_{yj}}{1-\,x_A}$$

$$x_A = (g_A)_{xx}(g_B)_{yy}\,\beta^2$$

An interesting prediction from equation 4.6 is that when $E = \varepsilon_b$ the transmission coefficient is independent of α. For $\beta = 1$ and $\varepsilon_b = 0$. Figure 4.9 shows examples of T (E) versus E for different values of α when $\varepsilon_b = 0$ while figure 4.10 shows the corresponding results when $\varepsilon_b = 0.5$. As expected, these curves coincide when $E = \varepsilon_b$. as is clear in figure 4.18

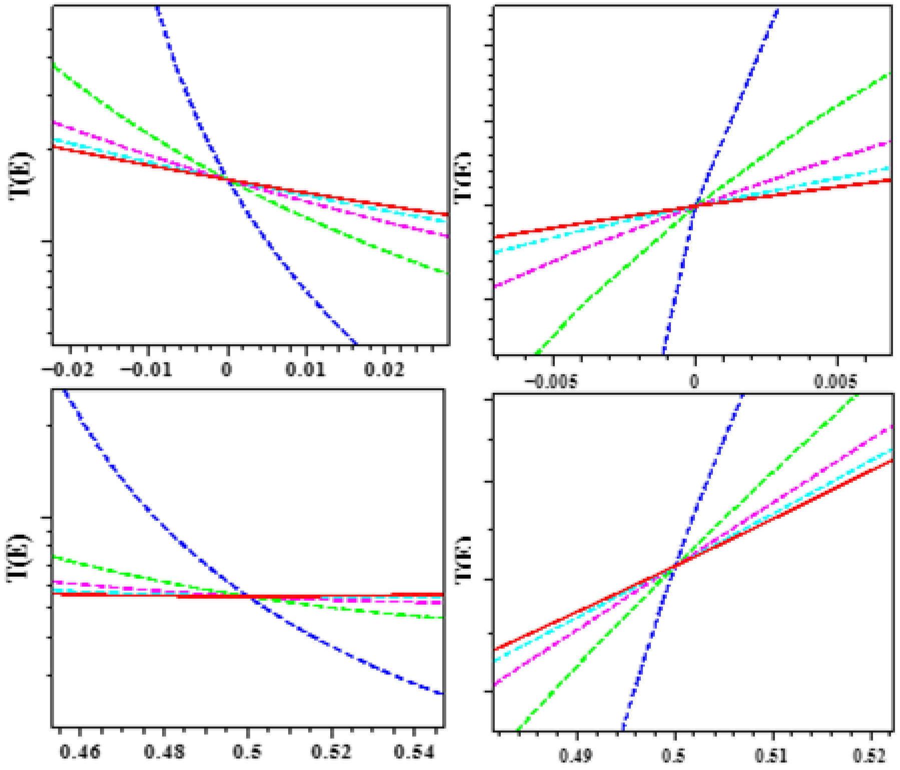

Figure 4.18 shows the zoom in of figure 4.7 and 4.8 the upper panel for $\varepsilon_b = 0$ and the lower for $\varepsilon_b = 0.5$ with left side para-para linked and right side meta-meta linked.

4.9 Conclusion

Overall, I find that constructive quantum interference in the para-connected molecules persists in the presence of bridging atoms and is partly masked by the presence of sigma channels, whereas bridging atoms alleviate destructive quantum interference in the meta-connected molecules. My comprehensive study establishes that both quantum interference and heteroaromaticity in the molecular core units play important and inter-related roles in determining the conductance of single molecular junctions. These results should assist in future research in the development of new molecules for incorporation into nanoscale molecular circuits.

References

[1] Huang, Guan-Jhih, et al. "Photoinduced Charge and Energy Transfer within meta-and para-Linked Chlorophyll a-Perylene-3, 4: 9, 10-bis (dicarboximide) Donor–Acceptor Dyads." The Journal of Physical Chemistry B 120.4 (2016): 756-765.

[2] Hong, Ze-Wen, et al. "Quantum interference effect of single-molecule conductance influenced by insertion of different alkyl length." Electrochemistry Communications 68 (2016): 86-89.

[3]. Carroll, R. L. & Gorman, C. B. The Genesis of Molecular Electronics. Angew. Chem. Int. Ed. 41, 4378–4400 (2002).

[4]. Chen, F., Hihath, J., Huang, Z., Li, X. & Tao, N. J. Measurement of Single-Molecule Conductance. Annu. Rev. Phys. Chem. 58, 535–564 (2007).

[5] Moth-Poulsen, K. & Bjørnholm, T. Molecular electronics with single molecules in solid-state devices. Nat. Nanotechnol. 4, 551–556 (2009).

[6]. Cuevas, J. C. & Scheer, E. Molecular Electronics: An Introduction to Theory and Experiment. (WORLD SCIENTIFIC, 2010).

[7]. Leary, E. et al. Incorporating single molecules into electrical circuits. The role of the chemical anchoring group. Chem. Soc. Rev. 44, 920–942 (2015).

[8]. Perrin, M. L., Burzurí, E. & van der Zant, H. S. J. Single-molecule transistors. Chem. Soc. Rev. 44, 902–919 (2015).

[9]. Song, H., Reed, M. A. & Lee, T. Single Molecule Electronic Devices. Adv. Mater. 23, 1583–1608 (2011).

[10]. Weibel, N., Grunder, S. & Mayor, M. Functional molecules in electronic circuits. Org. Biomol. Chem. 5, 2343–2353 (2007).

[11]. Reed, M. A., Zhou, C., Muller, C. J., Burgin, T. P. & Tour, J. M. Conductance of a Molecular Junction. Science 278, 252–254 (1997).

[12]. Xu, B. & Tao, N. J. Measurement of Single-Molecule Resistance by Repeated Formation of Molecular Junctions. Science 301, 1221–1223 (2003).

[13]. Lambert, C. J. Basic concepts of quantum interference and electron transport in single-molecule electronics. Chem. Soc. Rev. 44, 875–888 (2015).

[14]. Tour, J. M. et al. Synthesis and Preliminary Testing of Molecular Wires and Devices. Chem. – Eur. J. 7, 5118–5134 (2001).

[15]. Huber, R. et al. Electrical Conductance of Conjugated Oligomers at the Single Molecule Level. J. Am. Chem. Soc. 130, 1080–1084 (2008).

[16]. Kaliginedi, V. et al. Correlations between Molecular Structure and Single-Junction Conductance: A Case Study with Oligo(phenylene-ethynylene)-Type Wires. J. Am. Chem. Soc. 134, 5262–5275 (2012).

[17]. Zhao, X. et al. Oligo(aryleneethynylene)s with Terminal Pyridyl Groups: Synthesis and Length Dependence of the Tunneling-to-Hopping Transition of Single-Molecule Conductances. Chem. Mater. 25, 4340–4347 (2013).

[18]. González, M. T. et al. Stability of Single- and Few-Molecule Junctions of Conjugated Diamines. J. Am. Chem. Soc. 135, 5420–5426 (2013).

[19]. Jenny, N. M., Mayor, M. & Eaton, T. R. Phenyl–Acetylene Bond Assembly: A Powerful Tool for the Construction of Nanoscale Architectures. Eur. J. Org. Chem. 2011, 4965–4983 (2011).

[20]. Eicher, T., Hauptmann, S. & Speicher, A. in The Chemistry of Heterocycles 52–121 (Wiley-VCH Verlag GmbH & Co. KGaA, 2003).

[21]. Venkataraman, L., Klare, J. E., Nuckolls, C., Hybertsen, M. S. & Steigerwald, M. L. Dependence of single-molecule junction conductance on molecular conformation. Nature 442, 904–907 (2006).

[22]. Haiss, W. et al. Variable contact gap single-molecule conductance determination for a series of conjugated molecular bridges. J. Phys. Condens. Matter 20, 374119 (2008).

[23]. Vonlanthen, D. et al. Chemically Controlled Conductivity: Torsion-Angle Dependence in a Single-Molecule Biphenyldithiol Junction. Angew. Chem. Int. Ed. 48, 8886–8890 (2009).

[24]. Mishchenko, A. et al. Influence of Conformation on Conductance of Biphenyl-Dithiol Single-Molecule Contacts. Nano Lett. 10, 156–163 (2010).

[25]. Mishchenko, A. et al. Single-Molecule Junctions Based on Nitrile-Terminated Biphenyls: A Promising New Anchoring Group. J. Am. Chem. Soc. 133, 184–187 (2011).

[26]. Chen, W. et al. Aromaticity Decreases Single-Molecule Junction Conductance. J. Am. Chem. Soc. 136, 918–920 (2014).

[27]. Klausen, R. S. et al. Evaluating atomic components in fluorene wires. Chem. Sci. 5, 1561–1564 (2014).

[28]. Meisner, J. S. et al. Importance of Direct Metal−π Coupling in Electronic Transport Through Conjugated Single-Molecule Junctions. J. Am. Chem. Soc. 134, 20440–20445 (2012).

[29]. Arroyo, C. R. et al. Quantum interference effects at room temperature in OPV-based single-molecule junctions. Nanoscale Res. Lett. 8, 234 (2013).

[30]. Arroyo, C. R. et al. Signatures of Quantum Interference Effects on Charge Transport Through a Single Benzene Ring. Angew. Chem. Int. Ed. 52, 3152–3155 (2013).

[31]. Manrique, D. Z. et al. A quantum circuit rule for interference effects in single-molecule electrical junctions. Nat. Commun. 6, 6389 (2015).

[32]. Sangtarash, S. et al. Searching the Hearts of Graphene-like Molecules for Simplicity, Sensitivity, and Logic. J. Am. Chem. Soc. 137, 11425–11431 (2015).

[33]. Geng, Y. et al. Magic Ratios for Connectivity-Driven Electrical Conductance of Graphene-like Molecules. J. Am. Chem. Soc. 137, 4469–4476 (2015).

[34]. Moreno-García, P. et al. Single-Molecule Conductance of Functionalized Oligoynes: Length Dependence and Junction Evolution. J. Am. Chem. Soc. 135, 12228–12240 (2013).

[35]. Hong, W. et al. Single Molecular Conductance of Tolanes: Experimental and Theoretical Study on the Junction Evolution Dependent on the Anchoring Group. J. Am. Chem. Soc. 134, 2292–2304 (2012).

[36]. Kiguchi, M., Nakamura, H., Takahashi, Y., Takahashi, T. & Ohto, T. Effect of Anchoring Group Position on Formation and Conductance of a Single Disubstituted Benzene Molecule Bridging Au Electrodes: Change of Conductive Molecular Orbital and Electron Pathway. J. Phys. Chem. C 114, 22254–22261 (2010).

[37]. Wu, S. et al. Molecular junctions based on aromatic coupling. Nat. Nanotechnol. 3, 569–574 (2008).

[38] Frisenda, R. et al. Electrical properties and mechanical stability of anchoring groups for single-molecule electronics. Beilstein J. Nanotechnol. 6, 1558–1567 (2015).

[39]. Soler, J. M. et al. The SIESTA method for ab initio order- N materials simulation. J. Phys. Condens. Matter 14, 2745 (2002).

[40]. Langreth, D. C. & Perdew, J. P. Exchange-correlation energy of a metallic surface: Wave-vector analysis. Phys. Rev. B 15, 2884–2901 (1977).

[41].Ferrer, J. et al. GOLLUM: a next-generation simulation tool for electron, thermal and spin transport. New J. Phys. 16, 093029 (2014).

[42]. Quek, Su Ying, et al. "Mechanically controlled binary conductance switching of a single-molecule junction." Nature nanotechnology 4.4 (2009): 230-234.

[43]. Wang, Changsheng, et al. "Nanoscale aryleneethynylene molecular wires with reversible fluorenone electrochemistry for self-assembly onto metal surfaces." Organic letters 6.13 (2004): 2181-2184.

[44]. Wang, Changsheng, Andrei S. Batsanov, and Martin R. Bryce. "Nanoscale aryleneethynylene oligomers incorporating fluorenone units as electron-dopable molecular wires." Faraday discussions 131 (2006): 221-234.

[45]. Wang, Changsheng, Andrei S. Batsanov, and Martin R. Bryce. "Convergent synthesis of 10 nm aryleneethynylene molecular wires by an iterative regioselective deprotection/Sonogashira coupling protocol." The Journal of organic chemistry 71.1 (2006): 108-116.

[46]. Ismael, Ali K., Iain Grace, and Colin J. Lambert. "Connectivity dependence of Fano resonances in single molecules." Physical Chemistry Chemical Physics 19.9 (2017): 6416-6421.

[47]. Clayden, J., Greeves, N. & Warren, S. Organic Chemistry. (OUP Oxford, 2012).

[48]. Gold, V., et al. "IUPAC compendium of chemical terminology." Blackwell Science, Oxford (1997).

Chapter 5

Carbon Nanotube based single molecule devices

5.1 introduction

The molecular electronics is at the heart of nanoscience, because it hinges on the fundamental idea that novel devices can be created by using ingredients so small that new properties emerge. Molecules bring in their intrinsically quantum mechanical nature and hence molecular devices can exhibit characteristics that, even at ambient temperature, cannot be achieved otherwise. In fact, by making functional molecules, such as switches, synthetic chemists add a unique ingredient of variability and structural control that cannot be achieved with equivalent solid-state devices. The use of carbon-based nanoelectrodes, in particular, has emerged as a promising approach because of the intrinsic nanoscale size of CNTs and graphene and the reduced electronic mismatch granted by having molecules and electrodes of the same material (carbon atoms)[1-4].

5.2 Carbon Nanotube

The carbon nanotube (CNT) was discovered accidentally by Sumio Iijima in 1991.[5] There are two families of CNTs, namely single-wall CNTs and multi-wall CNTs (MWCNT). A single-wall CNT is a hollow cylindrical structure of carbon atoms with a diameter that ranges from about 0.5 to 5 nm and lengths of the order of micrometres to centimeters. An MWCNT is similar in structure to a single-wall CNT but has multiple nested or concentric cylindrical walls with the spacing between walls comparable to the interlayer spacing in graphite, approximately 0.34 nm. Carbon nanotubes are considered 1D nanomaterials owing to their very small diameter that confines electrons to move along their length.[1]

5.2.1 Chirality a concept to describe nanotubes

Chirality is the key concept used to identify and describe the different configurations of CNTs and their resulting electronic band structure. Since the concept of chirality is of fundamental importance I will introduce the concept before discussing how it is applied to describe CNT structure. The term chirality is derived from the Greek term for hand, and it is used to describe the reflection symmetry between an object and its mirror image. Formally, a chiral object is an object that is not superimposable on its mirror image; and conversely, an achiral object is an object that is superimposable on its mirror image.

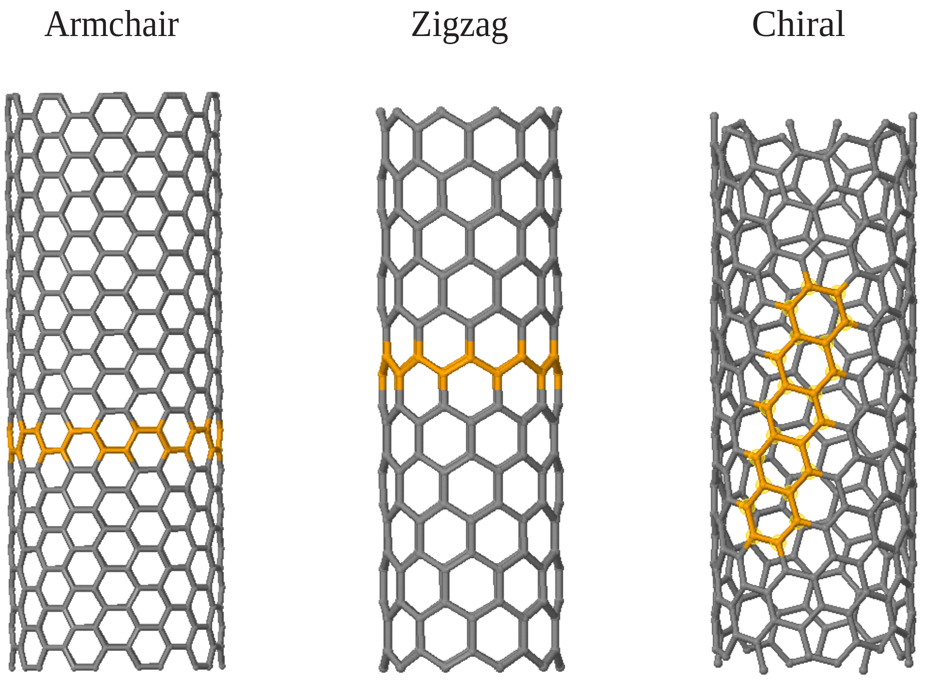

Fig. 5.1 The three types of single-wall CNT: (a) A chiral CNT, (b) an armchair CNT, and (c) a zigzag CNT. The cross-sections of the latter two illustrations have been highlighted by the bold lines showing the armchair and zigzag character respectively.

5.2.2 The CNT lattice

I introduced the concept of chirality to classify the different types of CNT in the previous section, but it was not at all clear why CNTs arrange to form a chiral or an achiral geometry. Fortunately, it is actually fairly easy to understand the origin of the different types of CNT by considering that a CNT results from folding or wrapping of a graphene sheet. To see how the folding operation works, I start from the direct lattice of graphene and then define a mathematical construction which folds graphene’s lattice into a CNT. Moreover, this mathematical folding construction directly leads to a precise determination of the primitive lattice of carbon nanotubes, which is required information in order to derive the CNT band structure. It is very important to keep in mind that the folding of graphene to form a CNT is simply a convenient conceptual idea to study the basic properties of CNTs. In actuality, CNTs naturally grow as a cylindrical structure, often with the aid of a catalyst, which does not involve folding of graphene in any physical sense.

Figure 5.2 shows the honeycomb lattice of graphene and the primitive lattice vectors a_1 and a_2, defined on a plane with unit vectors ˆx and ˆy:

$$a_1 = \left(\frac{\sqrt{3}\,a}{2}, \frac{a}{2}\right), \qquad a_2 = \left(\frac{\sqrt{3}\,a}{2}, -\frac{a}{2}\right) \qquad 5.5$$

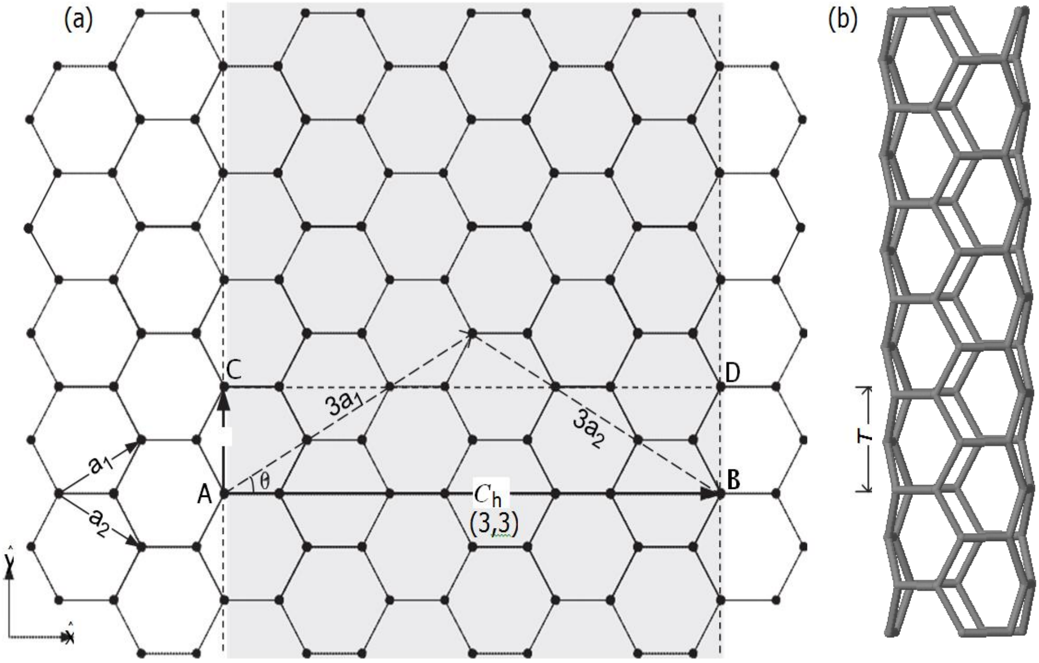

Figure 5.2 An illustration to describe the conceptual construction of a CNT from graphene. (a)Wrapping or folding the dashed line containing points A and C to the dashed line containing points B and D results in the (3, 3) armchair carbon nanotube in (b) with θ = 30◦. The CNT primitive unit cell is the cylinder formed by wrapping line AC onto BD and is also highlighted in (b).

where a is the underlying Bravais lattice constant, $a = \sqrt{3}a_{C-C} = 2.46$ Å, and a_{C-C} is the carbon–carbon bond length (∼1.42 Å). Also, $a_1 \cdot a_1 = a_2 \cdot a_2 = a^2, a_1 \cdot a_2 = a^2/2$, and the angle between a_1 and a_2 is 60◦. With reference to Figure 5.2a, a single-wall CNT can be conceptually conceived by considering folding the dashed line containing primitive lattice points A and C with the dashed line containing primitive lattice points B and D such that point A coincides with B, and C with D to form the nanotube shown in Figure 5.2b. The CNT is characterized by three geometrical parameters, the chiral vector C_h, the translation vector T, and the chiral angle θ, as shown in Figure 5.2a. The chiral vector is the geometrical parameter that uniquely defines a CNT, and $|C_h| = C_h$ is the CNT circumference. C_h is defined as the vector connecting any two primitive lattice points of graphene such that when folded into a nanotube these two points are coincidental or indistinguishable. For the particular exercise of Figure 5.2, the chiral vector is the vector from point A to B, $C_h = 3a_1 + 3a_2 = (3, 3)$. In general:

$$C_h = na_1 + ma_2 = (n, m) \quad where \ 0 \leq m \leq n \qquad 5.6$$

And the resulting carbon nanotube is described as an (*n*, *m*) CNT. The main parameters defining CNTs are shown in Table 5.1.

Table 5.1. Table of parameters and associated equations for CNTs [1,4]

Symbol	Name	CCNT	ACNT	ZCNT
$\boldsymbol{C}_h$	chiral vector	$\boldsymbol{C}_h = na_1 + ma_2 = (n,m)$	$\boldsymbol{C}_h = (n,n)$	$\boldsymbol{C}_h = (n,0)$
C_h	length of chiral vector	$C_h = a\sqrt{n^2 + nm + nm^2}$	$C_h = an\sqrt{3}$	$C_h = an$
d_t	diameter	$d_t = \frac{a}{\pi}\sqrt{n^2 + nm + m^2}$	$C_h = \frac{an}{\pi}\sqrt{3}$	$C_h = \frac{an}{\pi}$
θ	chiral angle	$\cos\theta = \frac{2n+m}{\sqrt{n^2 + nm + m^2}}$	$\theta = 30^0$	$\theta = 0^0$
gd	Greatest common divisor	$g_d = \gcd(2m+n, 2n+m)$	$g_d = 3n$	$g_d = n$
$\boldsymbol{T}$	translation vector	$\boldsymbol{T} = \frac{2m+n}{g_d}\boldsymbol{a}_1 - \frac{2n+m}{g_d}\boldsymbol{a}_2$	$T = \boldsymbol{a}_1 - \boldsymbol{a}_2$	$T = \boldsymbol{a}_1 - 2\boldsymbol{a}_2$
T	length of translation vector	$T = \frac{\sqrt{3}C_h}{g_d}$	$T = \boldsymbol{a}$	$T = \boldsymbol{a}\sqrt{3}$
N	Number of hexagons/cell	$N = \frac{2C_h^2}{a^2 g_d}$	$N = 2n$	$N = 2n$

5.2.3 The Tight Binding Model.

The electronic properties of the carbon structures can be described using a tight binding model. These are numerical calculations based upon the linear combination of atomic orbitals (LCAO) where the local potential energy is obtained from the Slater-Koster parameterisation. In particular for the case of the CNT we will need six Slater-Koster parameters to describe the C - C bond for a simple two center parameterisation. These are chosen by fitting first-principles LDA results of energy versus nearest-neighbour interatomic separation for diamond. Checks have been made to ensure that the parameters give reasonable results for the electronic band structure, elastic modulii and phonon frequencies in the diamond structure although these properties do not enter explicitly into the fitting procedure. The values are given in Table 5.2, where (ε_s , ε_p) are in the diagonal elements and ($V_{sss}, V_{sps}, V_{pps}, and\ V_{ppp}$) are in the off-diagonal elements that make up the tight binding Hamiltonian.

A crystalline solid can be viewed as an array of localised atomic orbitals, the overlap of which is only significant if the atoms are very close together. This is the tight binding model upon which the calculations are based. It does not describe the interatomic region, nevertheless it does provide a method to calculate accurately many physical effects usually outside computational capability by reducing the degrees of freedom involved.

To gain a clearer insight into the tight binding model consider the discretisation of the Schrodinger equation in terms of continuous coordinate (x),

Table 5.2. The (4 x 4) elements orbital of the total Hamiltonian [6]

	S	*Sp*$_x$	*Sp*$_y$	*Sp*$_z$
S	V_{sss}	$-l \times V_{sps}$	$-m \times V_{sps}$	$-n \times V_{sps}$
Sp$_x$	$l \times V_{sps}$	$l^2 \times V_{pps} + (1 - l^2)V_{ppp}$	$m \times l \times (V_{pps} - V_{ppp})$	$n \times l \times (V_{pps} - V_{ppp})$
Sp$_y$	$m \times V_{sps}$	$m \times l \times (V_{pps} - V_{ppp})$	$m^2 \times V_{pps} + (1 - m^2)V_{ppp}$	$n \times m \times (V_{pps} - V_{ppp})$
Sp$_z$	$n \times V_{sps}$	$n \times l \times (V_{pps} - V_{ppp})$	$n \times m \times (V_{pps} - V_{ppp})$	$n^2 \times V_{pps} + (1 - n^2)V_{ppp}$

The tight binding parameters given in the matrix above are the full sp3 tight-binding values. They enable the model to take into account the curvature of the nanotube surface (as opposed to the simpler π model considered in the analytical results). This is achieved by applying the formulas given in Table 5.3, which make up the full sp3 configuration. The direction cosines, (l,m,n), will describe the curvature of a given CNT from the position of each atomic site, which in turn will give values to all the elements of the 4 x 4 sub-matrix. Tight-binding results which take into account the *2s* electrons (as in this model) show that the large curvature of the small diameter CNTs (except for armchair CNTs) leads to hybridisation of the u and π orbitals. This results in a small energy gap (meV) in these tubes. Note when the unfolded energy bands of CNTs are seen in the 2-D Brillouin zone of graphite, the degenerate point at the K point moves away from this point due to the hybridisation effect. The hopping parameters of Table 5.3 are then scaled with interatomic separation r as a function s(r)[7].

$$s(r) = \frac{2.39}{r^2} exp\left\{-2.0\left[\left(\frac{r}{2.18}\right)^{6.5} + \left(\frac{1.546}{2.18}\right)^{6.5}\right]\right\} \qquad 5.7$$

Where *r* is the *C-C* bond distance.

Table 5.3 shows the parameter for C-C atoms,

es	-3.65
ep	3.65
V_{sss}	$-3.63 \times s(r)$
V_{sps}	$4.2 \times s(r)$
V_{pps}	$5.38\times s(r)$
V_{ppp}	$-2.24 \times s(r)$

The parameters in the above scaling function are again the result of fitting the tight-binding results to LDA calculations the full details of which are given in [7]. In my model the scaling function provides an accurate tailing off of the orbital interaction which limits the bonds to nearest-neighbour elements only i.e. there is a gradual cut off at approximately half way between the nearest-neighbour and next nearest-neighbour atomic positions in the CNT.

The material specific Hamiltonian for the Carbon nanotube can now be accurately constructed. To calculate the effects upon transport across the scattering region some clever numerical tricks need to be employed as follows.

5.3 Numerical simulations

5.3.1 Four orbital tight binding calculation

The focus of this chapter is to develop a model of a molecular junction using CNTs as electrodes. In these structures, direct bonding between the molecule and the lead should lead to more clearly defined contact geometries and stronger binding which will enhance conductance. This is in comparison to metal/molecule/metal junctions where the contact geometry is unknown and leads to a statistical distribution of conductance values. To begin with a four orbital tight binding calculation is constructed to predict the transmission coefficient of a perfect crystalline CNTs. Figure 5.3 shows the transmission coefficient for three different types of CNTs, two zigzag and one armchair. The black line is for a CNT(8,0) and a gap of 0.68 eV opens at 0eV, this gap decrease to 0.04 eV for CNT(9,0) (red line), on the other hand the blue line indicates the metallic CNT(5,5) where the band gap disappears. Thus this model accurately predicts the electronic properties of these structures, as zig-zag nanotubes are expected to be semi-conducting unless n is divisible by 3 and all arm-chair nanotubes are metallic. In the case of the (9,0) CNT the opening of a small gap is due to the curvature of the tube.

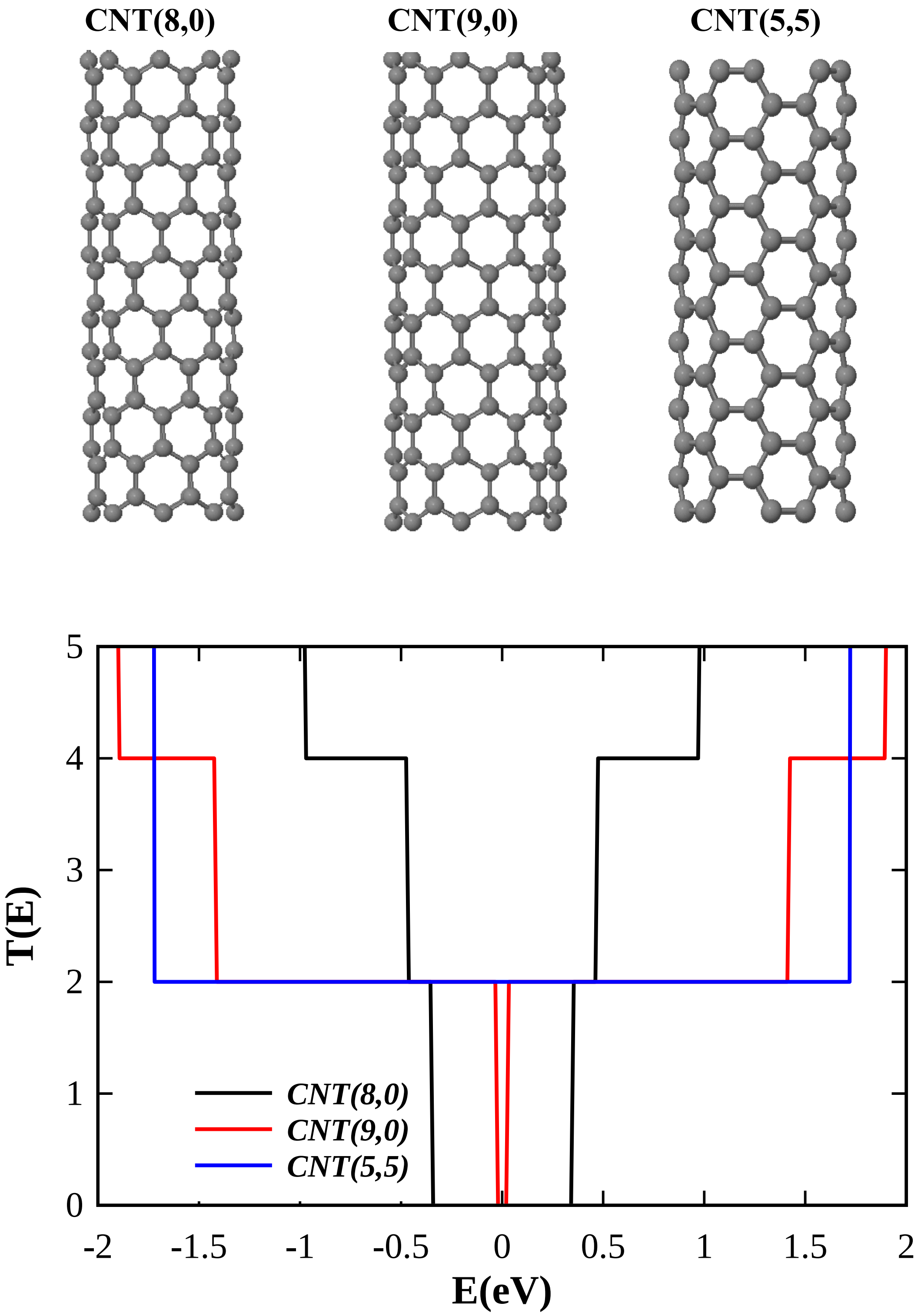

Figure 5.3 (Top) Geometry of a (8,0), (9,0) and (5,5) CNT. (Bottom) Zero bias transmission coefficient T(E) for (8,0), (9,0) and (5,5) using a four orbital tight binding model.

The CNT(5,5) will form the basis of the electrodes, because it is metallic and has two open channels close to the Fermi energy (0eV) . The next step is to attach the molecule to form a junction. To test this tight binding method I am again going to investigate the connectivity dependence that was studied in the previous chapter. Using a simple benzene ring and assuming direct carbon-carbon coupling between the edge of the nanotube, I calculate transmission for the case of para-para ,meta-meta and ortho-ortho binding. The structures and transmission coefficients can be seen in Figure 5.4. In this case I ignore the role of hydrogen atoms, and the conductance of the meta-meta coupling is lowest in agreement with previous work in the literature[8].

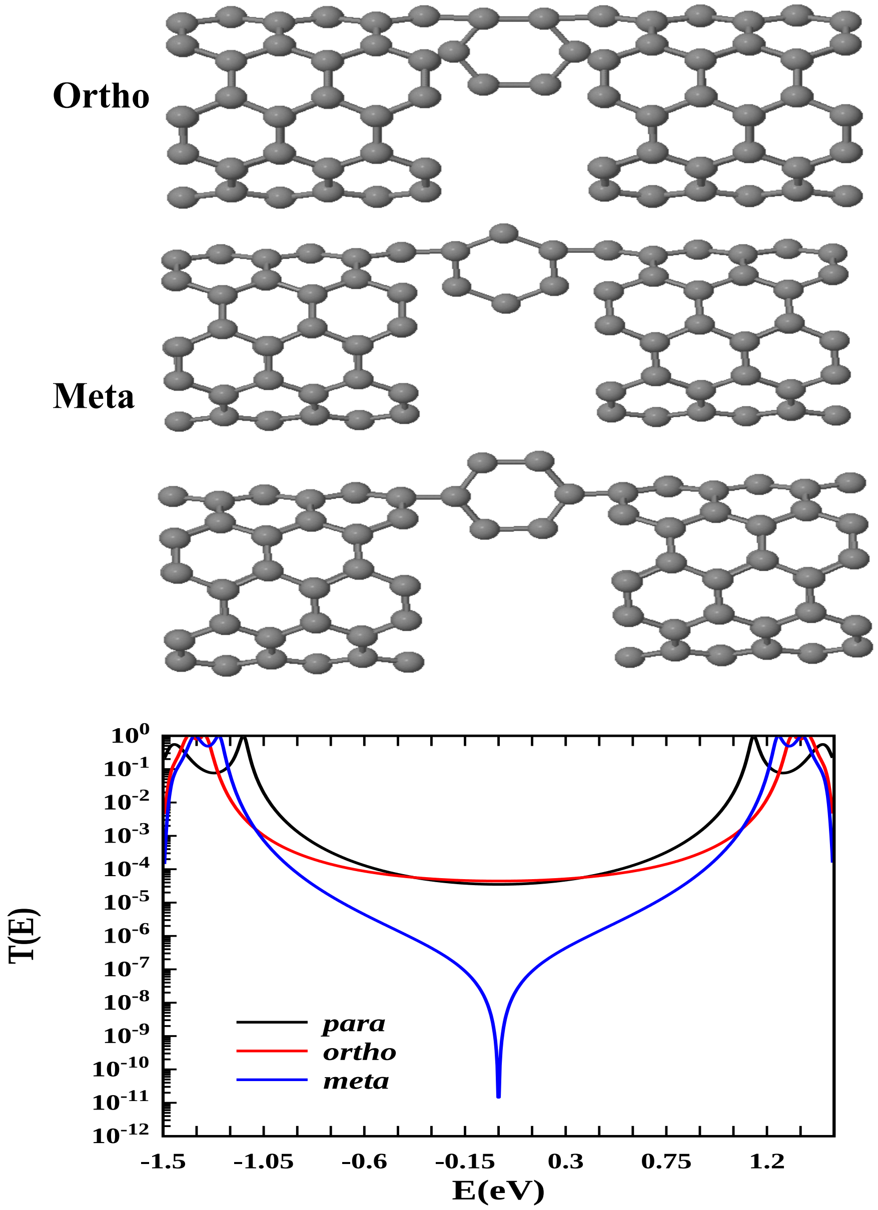

Figure 5.4 Transmission coefficient of benzene with CNT (5,5) electrodes for para-para, meta-meta and ortho-ortho linked.

The second test I apply using this model is to investigate the length dependence of these junctions on conductance. Here, I increase the number of benzene rings up to 3 and these structures are shown in Figure 5.10a and 5.10b with the molecules connected in the para orientation. The resulting transmission curves shown in figure 5.5 show the expected behaviour of a decrease in conductance in the longest molecule as is usually found in metal-molecule conductance measurements. The final step is to replace the central 6 carbon ring with a 5-carbon ring (5.5c). The result of the transmission coefficient shows similar behaviour to 5.5b but has an extra anti-resonant feature at -1.0eV. In conclusion, the four-orbital tight binding model I have developed is suitable to use with carbon based systems and can provide qualitative understanding of transport such as quantum interference. However, for more complicated molecules containing atoms other than carbon e.g. nitrogen and oxygen the construction of tight-binding parameters is difficult. Therefore, to overcome this and to allow for a more quantitative model I switch to the DFT method.

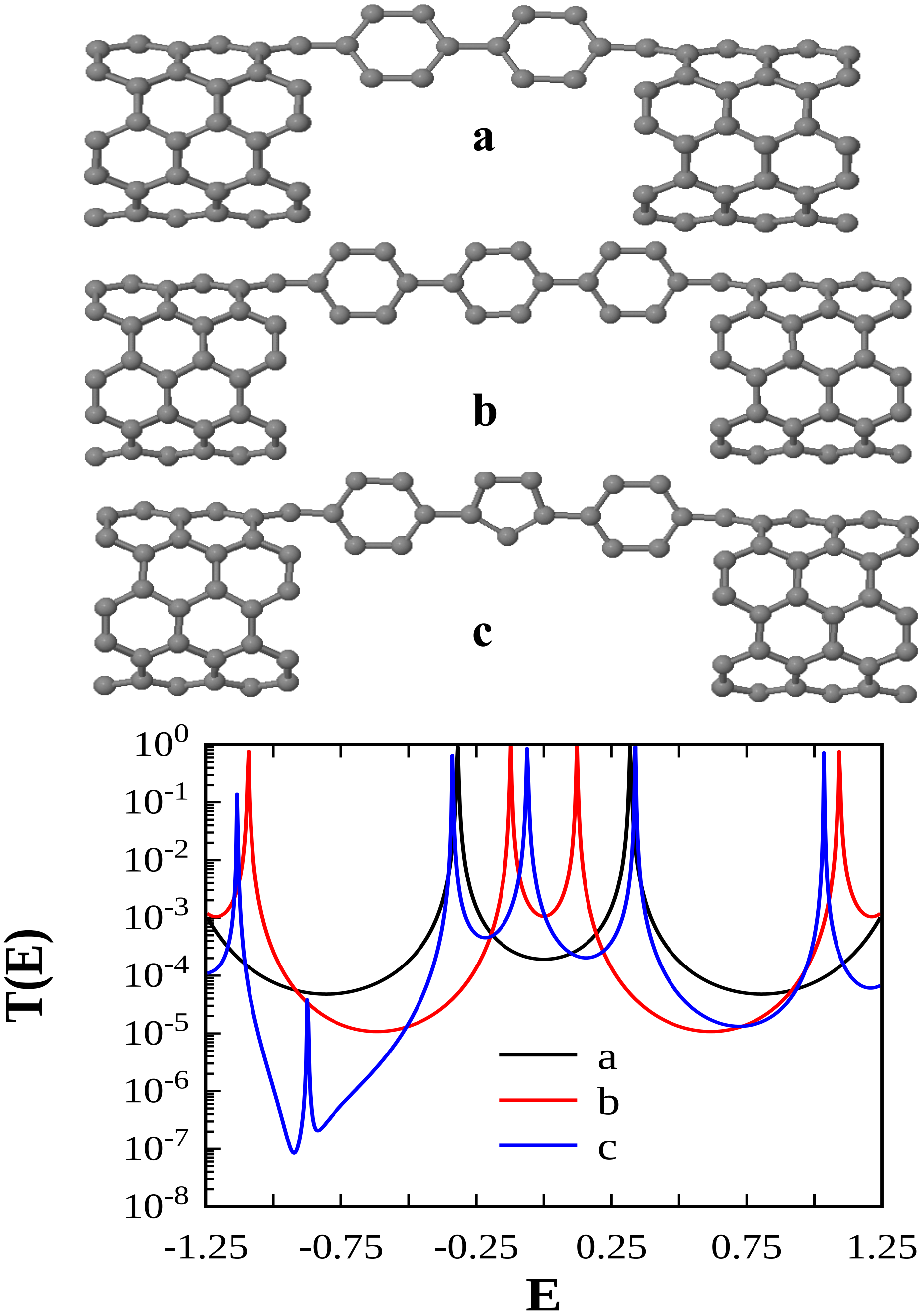

Figure 5.5 Transmission coefficient of a-two benzene ring, b-three benzene ring and c-five atoms in mid two benzene ring with CNT (5,5) electrodes.

5.3.2 DFT calculations

The motivation for this work is previous experimental work[25] which using a chemical synthesis approach and AFM measurements has shown it is possible to measure the conductance of carbon nanotube molecule junctions. In this work, I focus on the molecules shown in Figure 5.6 which I call M1 and M2.

Following the previously described method to calculate the electrical properties of single molecules, I used density function theory (DFT), SIESTA code [9] to obtain the Hamiltonian of the structure and relax the system shown in figure 5.6. A double-zeta polarized basis set was used for all atoms and the local density approximation (LDA) [10], for the exchange and correlation functionals. The Hamiltonian and overlap matrices are calculated on a real-space grid defined by a plane-wave cut-off of 200 Ry. Each molecule was relaxed to the optimum geometry until the forces on the atoms are smaller than 0.01 eV/Å and in case of the isolated molecules; a sufficiently-large unit cell was used to avoid inter-cell interactions.

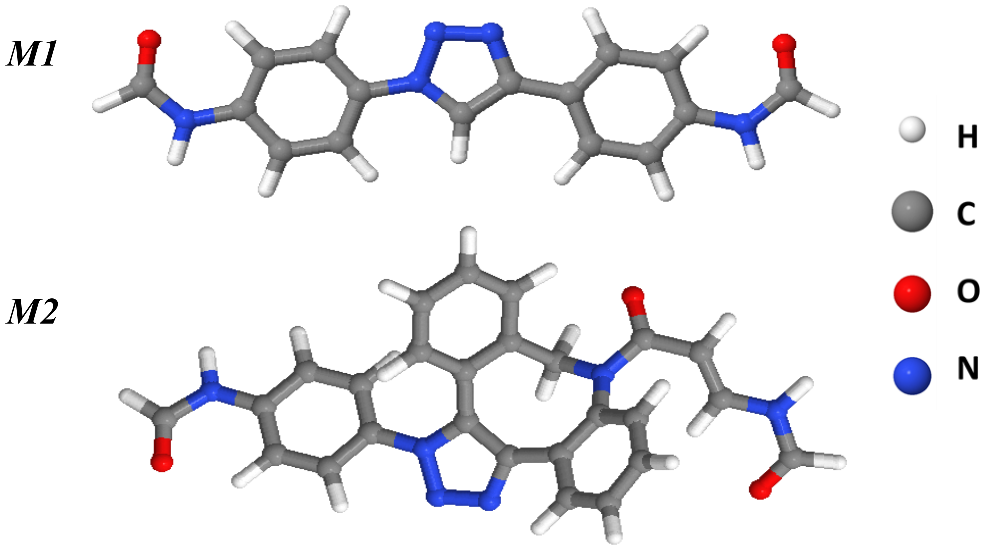

Figure 5.6 Optimized geometries of molecules M1 and M2

5.4 Calculation of Electronic Properties

In this section I will present the DFT calculated electronic properties for perfect crystalline CNTs of differing chirality (*n*,*m*) . I have studied several different types of CNTs, such as zigzag, armchair and chiral and for each of these I calculate the band structure and number of open channel channels. This study is important to determine that this method gives the correct behaviour for the electrodes.

5.4.1 CNT (n, m)

The unit cell of an (8,0) nanotube has 32 atoms, with its axis lying along the z-direction as shown in the figure 5.7a. The calculated band structure (5.12a) shows there is a gap of about 0.6 (eV) between valence and conduction band and the number of open channels drops from a value of 2 at this gap. This is in good agreement with the previously calculated tight binding model. Figure 5.7b shows the results for (9,0) which has 36 atoms in the unit cell. The band structure has a very small gap of about 0.06 eV and therefore the semimetal (9,0) is not a good metallic electrode. The (5,5), Figure 5.7c, is the best choice for the electrodes, because it does not have a gap around the fermi level and it has two open channels. The size of the unit cell is also small (20 atoms). The final nanotube I investigate is the chiral (7,4) shown in figure 5.7d which is expected to be metallic. The resulting band structure shows this and the behaviour is similar to the armchair tube. It has 124 atoms in its unit cell which makes it computationally expensive to use as an electrode, also the chirality makes the contact between molecule and lead asymmetric. Therefore, while experimental junctions may typically be formed using metallic chiral nanotubes the electronic properties can be modelled using the simple armchair nanotubes.

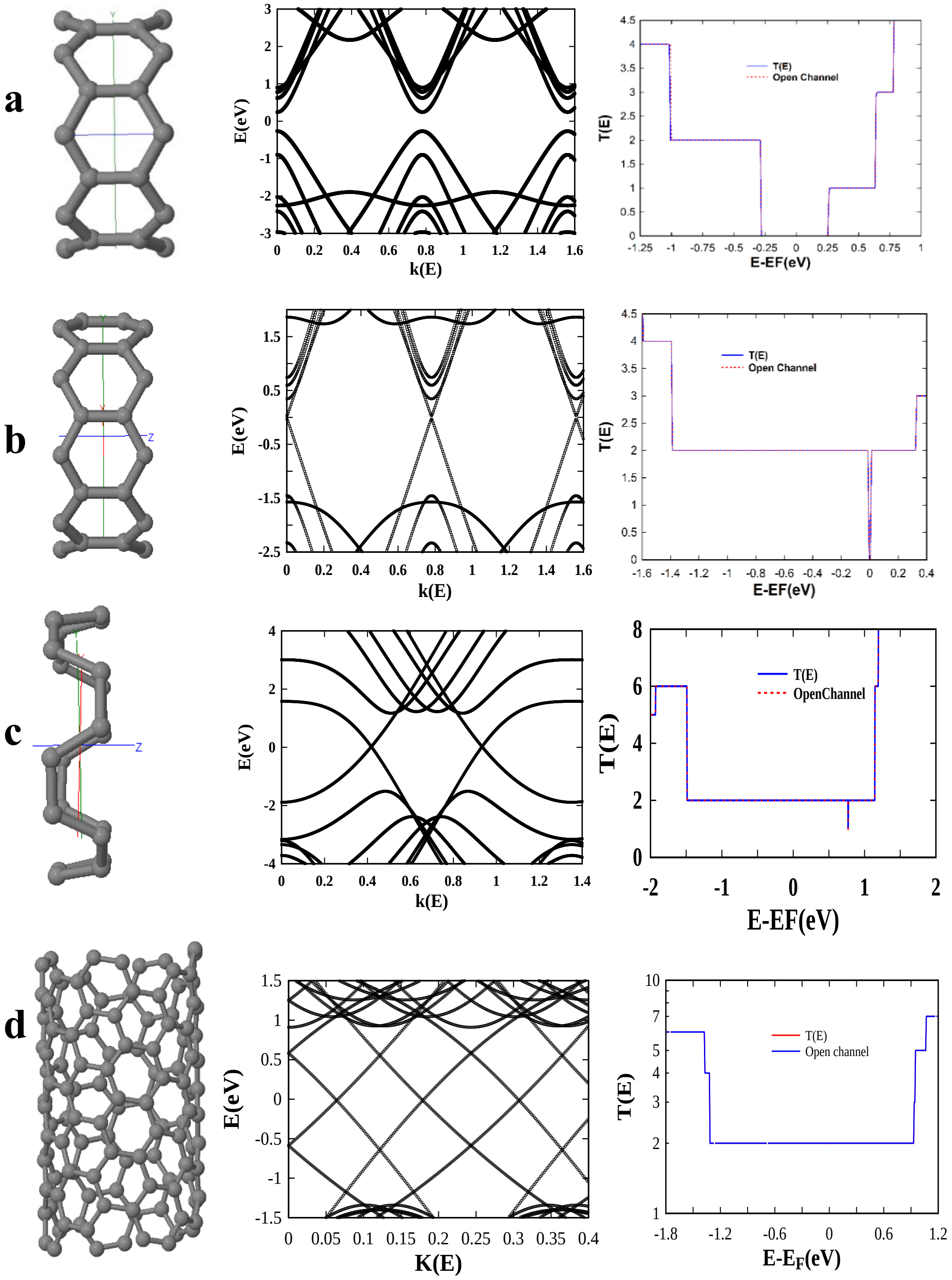

Figure 5.7 CNT(n,m) configuration, band structure of CNT(8,0) and transmission coefficient and open channel for a- CNT(8,0),b- CNT(9,0), c- CNT(5,5), d- CNT(7,4),

5.4.2 Binding Energy

The next step is to understand how the molecules M1 and M2 attach to the edge of the nanotube, and to do this I calculate the optimum binding geometry of each attached to the CNT(5,5). For these molecules the expected binding is through a direct carbon-carbon coupling to the terminal carbon atoms (there the hydrogen atoms shown in Fig 5.13 attached to the end carbons are removed). I again used the SIESTA implementation of DFT and the counterpoise method, which removes basis set superposition errors (BSSE). The binding distance d is defined as the distance between the CNT(5,5) surface and the molecule (M1) at the closest point. M1 is defined as monomer A and the CNT(5,5) electrodes as monomer B.

The ground state energy of the total system is calculated using SIESTA and is denoted E_{AB}^{AB}, with the parameters defined as those in section 5.3.2. The CNT(5,5) consists of 2 layers containing 20 atoms. The energy of each monomer is then calculated in a fixed basis, which is achieved by the use of ghost atoms in SIESTA. Hence the energy of the individual molecule M1 in the presence of the fixed basis is defined as E_{A}^{AB} and for the CNT(5,5) is E_{B}^{AB}. The binding energy is then calculated using the following equation:

$$\text{Binding Energy} = E_{AB}^{AB} - E_{A}^{AB} - E_{B}^{AB} \qquad 5.8$$

Figure 5.8 shows the optimum binding distance d is 1.6 Å and the binding energy is approximately -3.4 eV. The distance is equivalent to the formation of a covalent bond and has a large binding energy, meaning the binding of the molecule in this structure is much stronger than in typical molecular junctions.

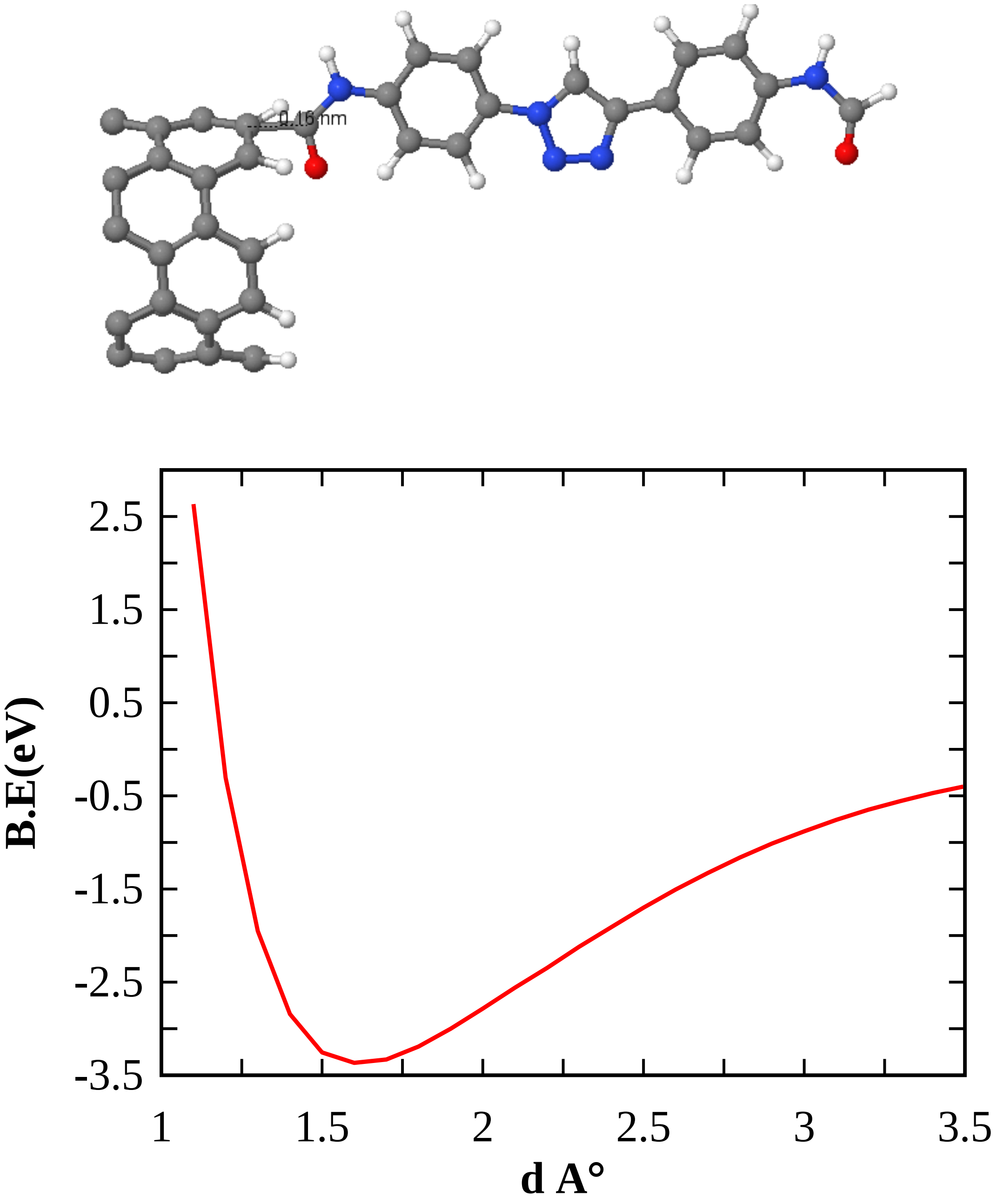

Figure 5.8. Molecule (M1) on a CNT(5,5) surface. M1 molecule with respect to the CNT(5,5) leads (above panel). Binding energy of M1 molecule to CNT(5,5) as a function of molecule–contact distance (below panel). The equilibrium distance is found to be approximately 1.6 Å from the minimization of the binding energy.

In the literature the typical distance between C-C for a single bond is about 1.5 A^o, therefore the above distance of 1.6 A^o is slightly larger. However, this fixed energy calculation doesn't allow for a change in the angle between the nanotube and molecule. Therefore, using the optimized bond length as a stating point, I then performed a geometry relaxation in which the atoms of the electrode are fixed. The figure (5.9) below shows the geometry after relaxation for M1 and M2 contacted to a (5,5) and the carbon-carbon bonding distance decreases to 1.5 Å in M1 and 1.47 Å in M2 and also the bonding angle is changed.

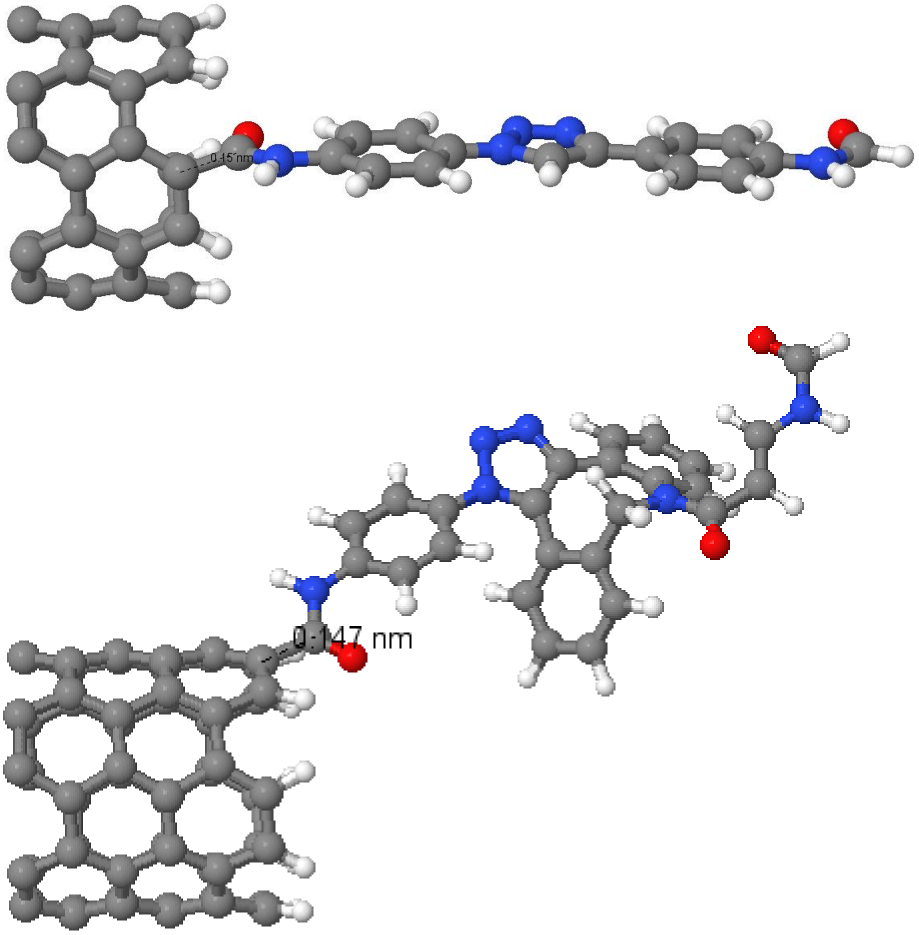

Figure 5.9. Optimized molecules M1 (top) and M2 (bottom) on a CNT(5,5) surface the distance for M1 =1.5 and for M2=1.47

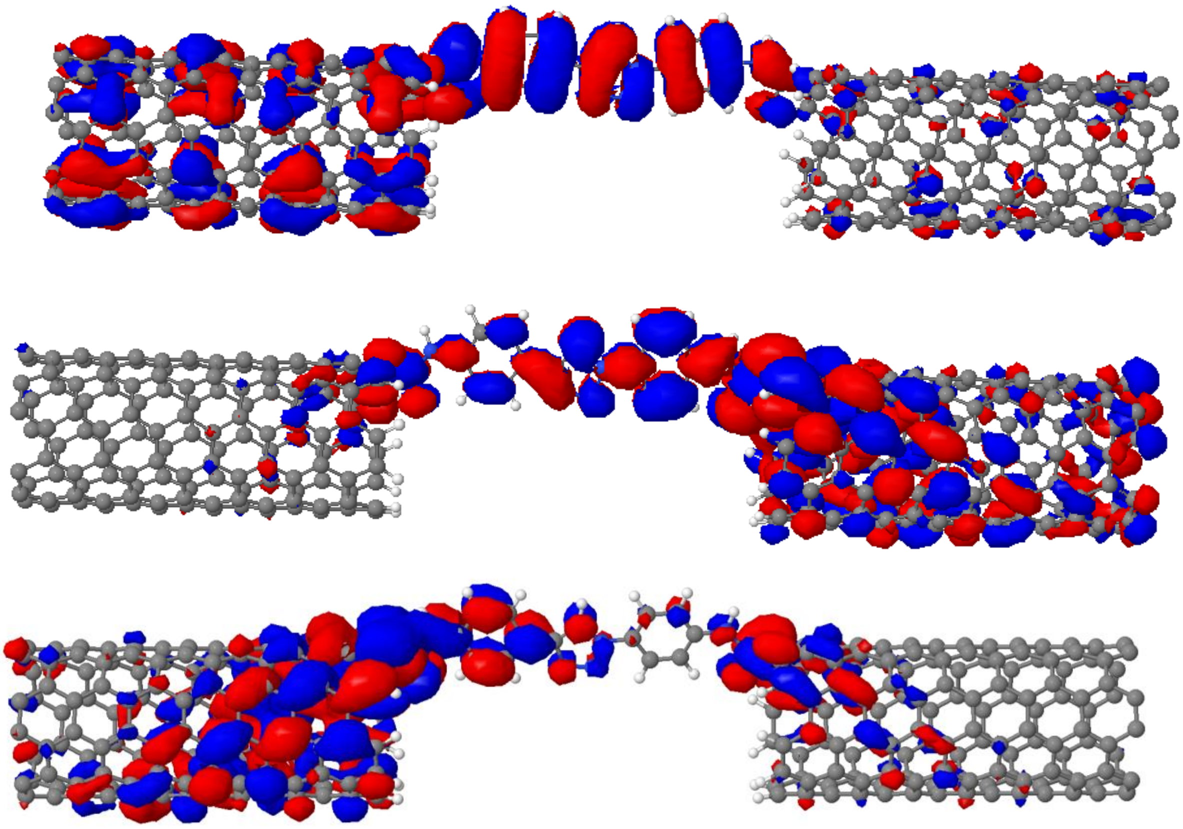

Figure 5.10. DFT based orbital diagrams for compounds M1.

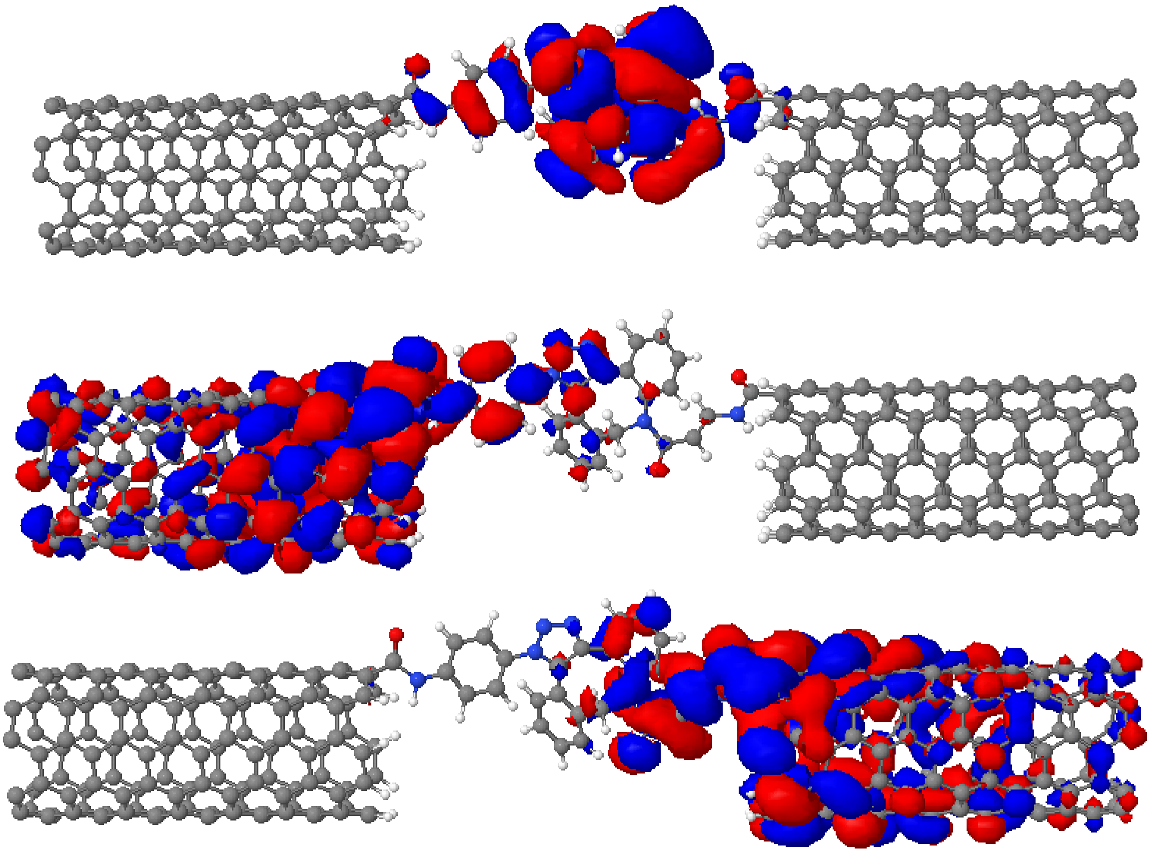

Figure 5.11. DFT based orbital diagrams for compounds M2

Charge density plots of the first highest occupied molecular orbital and lowest unoccupied molecular orbital for M1 and M2 bound to CNT(5,5) are shown in figures 5.10 and 5.16. By comparing the topology of the HOMO and LUMO orbitals of M1 and M2 I see that the charge density is evenly distributed across the length of M1 for both the HOMO and LUMO orbital, whereas in M2, HOMO is delocalized. But for LUMO M2 is biased towards the left part and the LUMO+1 biased to the opposite side that is because of the degeneracy of the orbitals. This simple orbital analysis provides some insight into the mechanisms responsible for the rectification ratio.

5.4.3 Transmission coefficient

The electrical transport properties of the nanoscale systems M1 and M2 were calculated using Gollum [11] from the converged mean-field DFT Hamiltonian provided by SIESTA. Gollum is based upon equilibrium transport theory and is used to calculate the transmission coefficients T(E) for electrons of energy E. Once computed the zero-bias electrical conductance G is obtained from the Landauer formula.

$$G = G_0 \int_{-\infty}^{\infty} dE\, T(E) \left(-\frac{\partial f(E,T)}{\partial E} \right) \qquad 5.9$$

where $G_0 = \left(\frac{2e^2}{h}\right)$ is the quantum of conductance and f(E,T) is the Fermi distribution function defined as $f(E,T) = [e^{(E-E_F)/k_B T} + 1]^{-1}$ with k_B is Boltzmann constant.

Figure 5.10 shows the transmission coefficient of M1 and M2 molecules attached to CNT(5,5), from this curve we can see that the molecules show resonant behaviour, even in the case of a strongly bound system. The Fermi Energy (0eV) sits in the gap between the HOMO and LUMO resonances and the values of transmission are about 3.0e-7 for M2 and 6.5e-7 for M1 and the ratio is about 0.45 at Fermi energy. The value of M2 is higher due the smaller HOMO-LUMO gap.

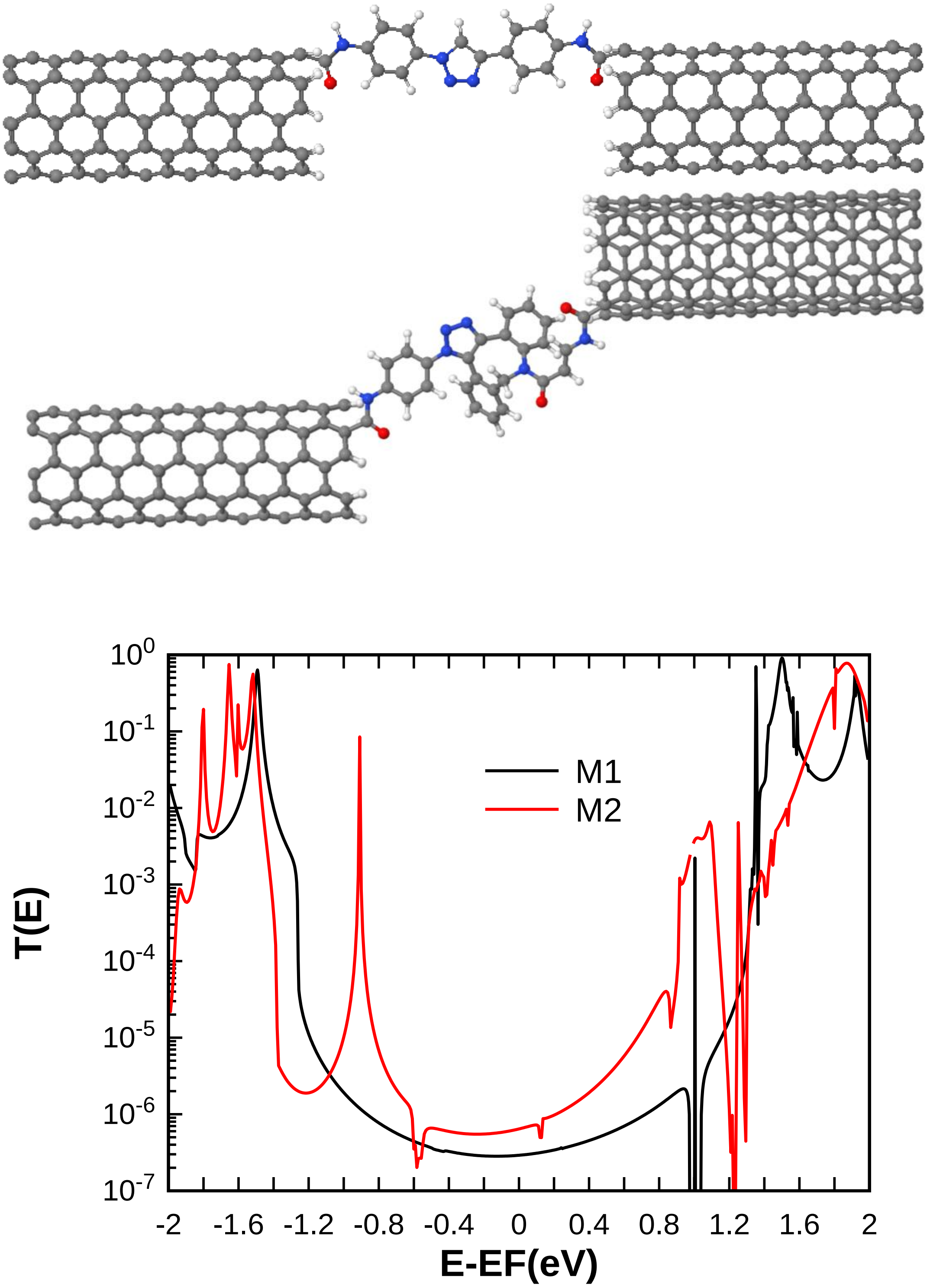

Figure 5.12Transmission coefficient T(E) against energy E(eV) for M1 and M2 attached to CNT (5,5) terminated by hydrogen atoms[25].

Using equation 5.9 I then calculate the conductance of these molecules at room temperature and the results are shown in Figure 5.11. Here we can see that there is thermal broadening of the transmission resonances and shows the value of the log of the conductance for M1 and M2 molecules, are -6.5 for M1 and -6.2 for M2 at $E_F=0$.

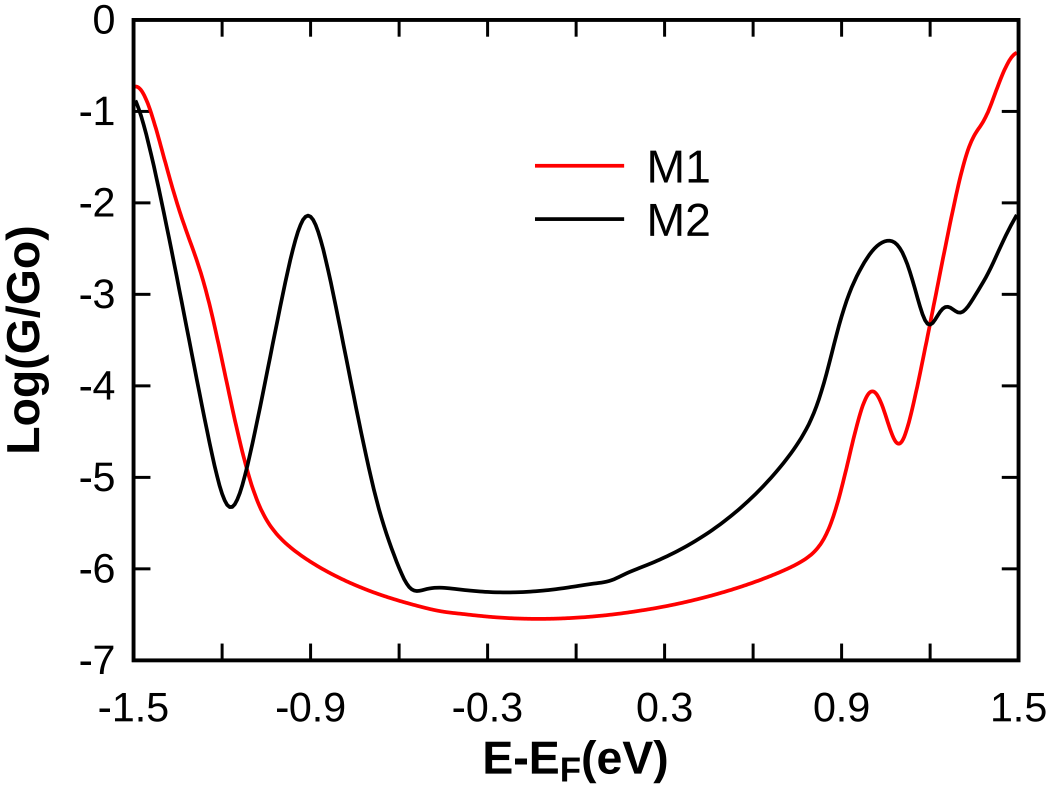

Figure 5.13 Conductance against energy E(eV) for M1 and M2

5.4.4 Current rectification

Molecular electronics aims to use molecules as active elements in nanoscale electronic circuits and it was born with the prediction that a single molecule could function as a diode [12]. Molecular rectification has been shown in many-molecule devices [13-16], in some cases the rectification ratios increasing from 2 to about 1500 [17-20], but often the current density is very low (fraction of the nano-amp). Single-molecule diodes have also been reported [21-23], but in all cases, they suffer from low rectification ratios (< 10). Recently J. Trasobares and co-worker [27], studied molecular diode junctions composed of a gold nanoelectrode and found that the current density increased by more than nine orders of magnitude compared with that of micrometre-scale molecular diodes with the same molecule [28,29]. To achieve a single-molecule rectification effect, we must provide a reliable and symmetric contact between an asymmetric molecule and two electrodes, and be able to determine and control the orientation of the molecule relative to the polarity of the applied bias voltage. The threshold bias voltage applied in the junction is about 1.8 V which was the value used by Tao's group [21].

Rectification of current is an essential parameter in fabricating any device for electronic purposes. Traditional MOFSET's can rectify current with a very low forward voltage drop, and also have the advantage of being able to switch at very high speeds. Therefore, molecular equivalents of diodes must exhibit properties of switching and rectification of the current.

The indication used to assess the suitability of a particular molecule for use as a diode is the rectification ratio (RR). This number is estimated from current-voltage characteristics, and is the ratio of the current at two equal but opposite voltages:

$$RR = \left|\frac{I(+V)}{I(-V)}\right| \qquad 5.10$$

In the Landauer formalism, the current in this model is given by

$$I = \left(\frac{2e}{h}\right)\int_{-\infty}^{\infty} dE\, T(E)\left[f_{left}(E) - f_{right}(E)\right] \qquad 5.11$$

where $e = |e|$ is the electronic charge, h is Planck's constant and T(E) is the transmission coefficient for electrons passing from one lead to the other via the molecule. Clearly $I = 0$ *when* $f_{left}(E) = f_{right}(E)$, because only differences in the distributions contribute to the net current.

Close to equilibrium, $f_{left}(E) = \left[e^{\beta\left(E-E_F^{left}\right)} + 1\right]^{-1}$ and $f_{right}(E) = \left[e^{\beta(E-E_F^{right})} + 1\right]^{-1}$

Where E_F^{left} and E_F^{right} is the fermi energy of the left and the right reservoir, and $\beta = \frac{1}{k_B T}$ where T is the temperature, If V is the voltage difference between the left and right reservoirs, then $E_F^{left} = E_F + \frac{V}{2}$ and $E_F^{right} = E_F - \frac{V}{2}$, This means that at zero temperature, but finite voltage

$$I = \left(\frac{2e}{h}\right)\int_{E_F-\frac{V}{2}}^{E_F+\frac{V}{2}} dE\, T(E,V) \qquad 5.12$$

Where $T(E,V)$ is the transmission coefficient at voltage V

In order to find IV curve of this system I applied a positive voltage on the left hand of the junction shown in the figure 5.14 bounded by the blue line and negative voltage on the right hand (yellow line). The rectification is dependent on this voltage profile, therefore in this study I pick two different paths for M1 as shown in 5.14(a,b), and for M2 just one path, figure 5.14c.

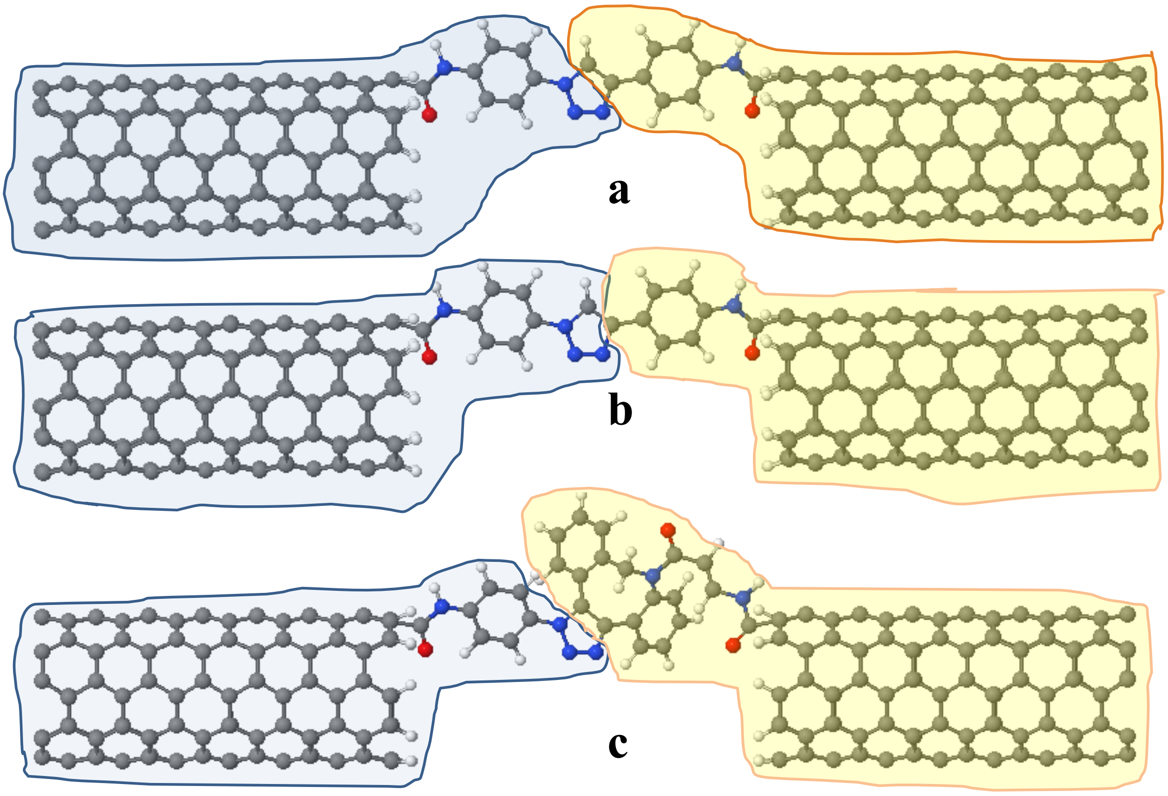

Figure 5.14 the molecules are coupled to the lead a-M1path 1 b- M1 path 2 c- M2

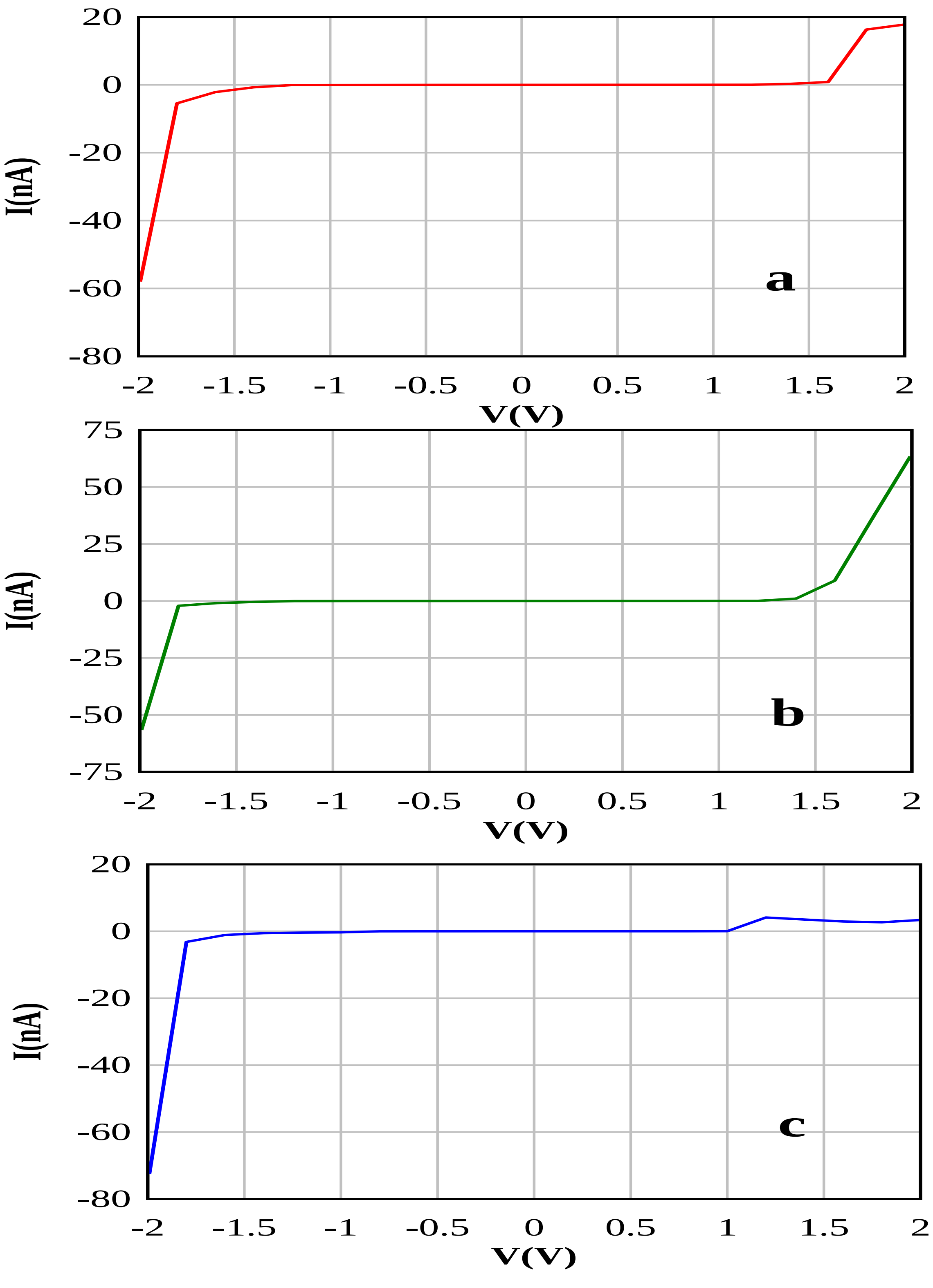

Figure 5.15 I-V characteristics acquired for a- M1 path 1 b- M1 path 2 c- M2

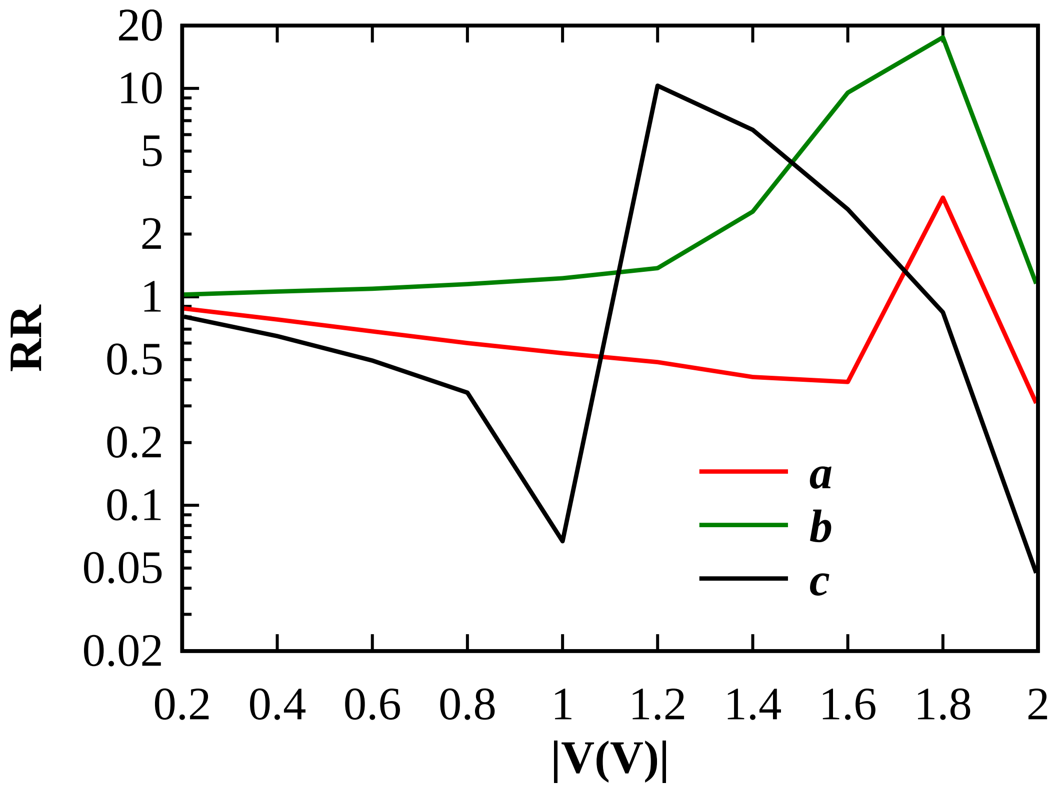

Figure 5.16 Rectification ratio as a function of applied voltage for CNT (5, 5) |molecule| CNT (5, 5) junctions.

The observed rectification can be compared for M1 and M2 by plotting the rectification ratio as a function of applied bias for the three paths of two molecules (figure 5.16). It is clear from this figure that the RR > 0 for both molecules, for M1 voltage profile 2 the magnitude of RR it is about 20 at 1.8(V) but for the same molecule it is reduced to 7 with a different voltage profile (figure 5.16 a,b). In the case M2, the maximum value of RR is at 1.2 (V) and has a value of about 10. In the end both these molecules have good rectification in comparison with previous work 2.5 [21]. This result is related to the asymmetry of molecule because the current encounter a wider tunneling barrier at reverse bias than at forward bias. Since tunneling current decreases exponentially with increasing width of the barrier [30]

For a functional diode, not only is a high rectification ratio needed but also a large enough current. In Figure 5.15 (a,b,c) , I observe that currents higher than 50 *nA* in the backward case (-V),but forward case it is about a couple of nA's.

Another method used to find the IV characteristics, is to apply an external electric field (which would be produced by an equivalent applied voltage) in the DFT calculation on the M1 and M2 molecule when attached to electrodes. Here, the voltage was varied between -1.8 to 1.8 (V) by using siesta code, as we can see from figure 5.17 the transmission coefficient are slightly different for both M1 and M2 with varied external electric field. For this reason, the forward current is almost the same as the reverse current (figure 5.18), therefore the rectification ratio is equal to one in both cases, and the magnitude of the current is about a fraction of a nano-amp. This is too low compared with the Gollum method. The reason for this is the voltage dropping at the contact between lead and molecule, on the contrary with Gollum method the dropping is on the path indicated by the figure 5.14.

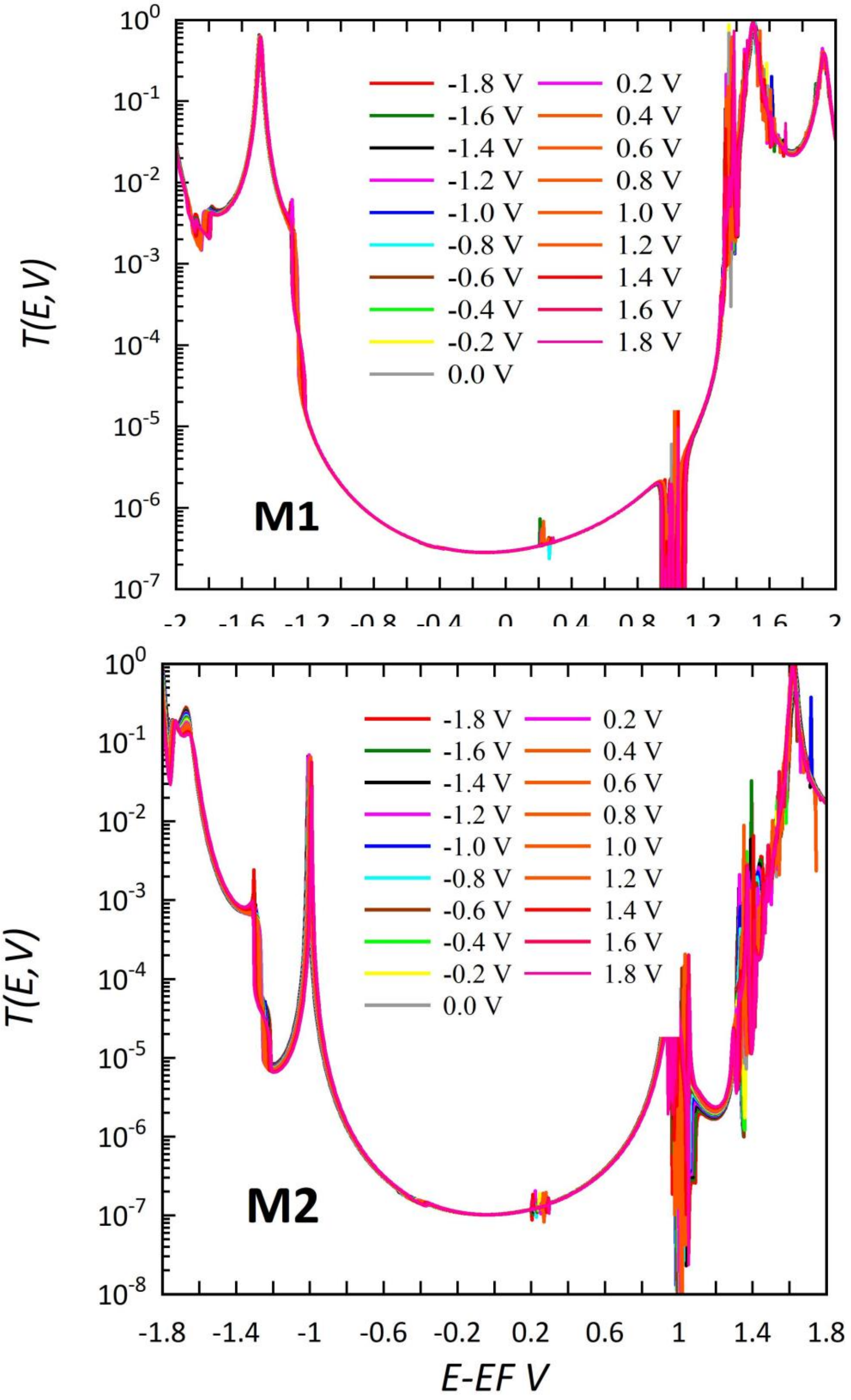

Figure 5.17Transmission coefficient T (E, V) against energy E(eV) for M1 and M2

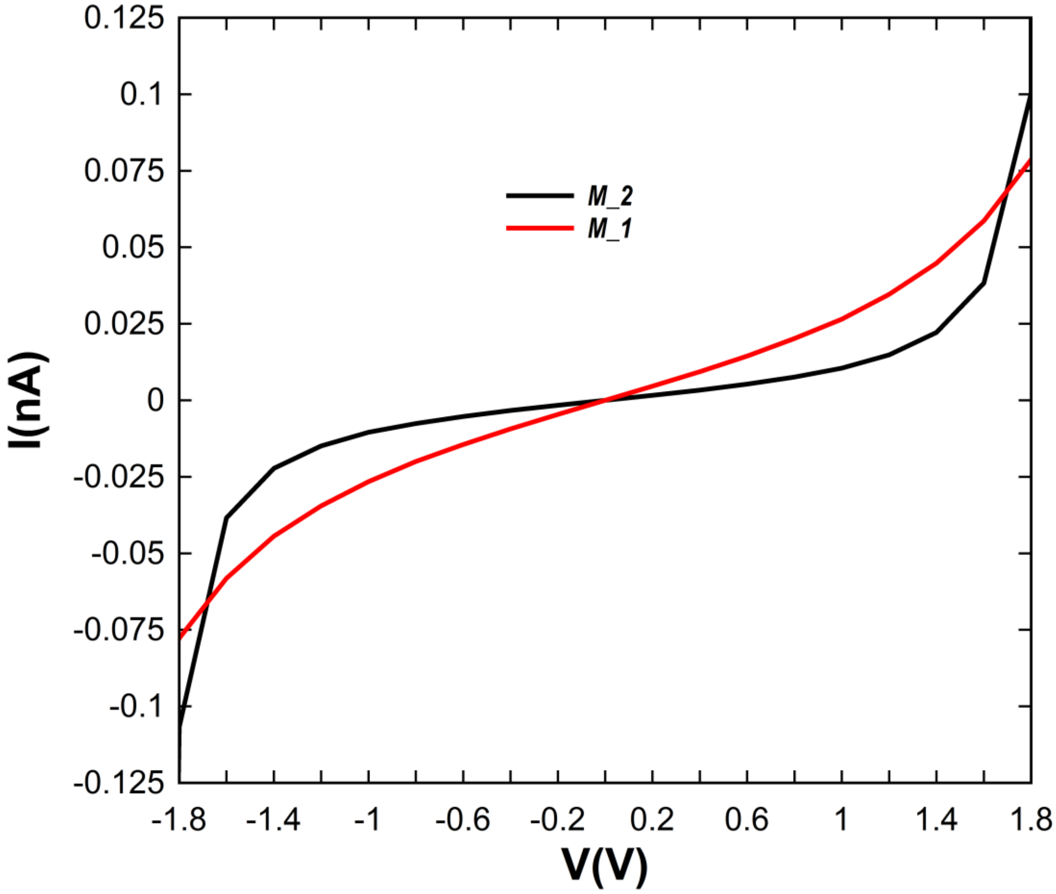

Figure 5.18 I-V characteristics acquired for M1 and M2 by using external electric field across the molecule

5.4.6 Conclusions

Most single molecule electronic studies are based on gold/molecule/gold junctions due to the wide range use of STM and break junction techniques. Here using a new experimental approach based on solution formed junctions as motivation, I have investigated the possibility of nanotube based molecular junctions. I have studied charge transport through asymmetric molecules attached to armchair carbon nanotubes. To do this I have calculated the I-V characteristics and rectification ratios. During this work I have investigated different types of CNT's for use as leads and have developed a four orbital tight binding model to use alongside DFT calculations with the aim of producing a deeper understanding of the transport calculations. I have shown that using a simple representation of a junction using just carbon atoms can give good agreement with DFT calculations for a full simulation.

The advantage of these carbon based junctions is that the molecules are strongly bound to the electrodes which should remove the large fluctuations in conductance present in molecule anchored to gold. Here I show that for these type of systems the transport is still determined by the nature of the energy levels of the molecule with the Fermi energy positioned in the HOMO-LUMO gap and the behaviour shown is similar to that produced on gold electrodes.

References

[1] Scheer, Elke. "Visions for a molecular future." Nature nanotechnology 8.6 (2013): 386.

[2 Yan, Haijun, Adam Johan Bergren, and Richard L. McCreery. "All-carbon molecular tunnel junctions." Journal of the American Chemical Society 133.47 (2011): 19168-19177.

[3] Zhu, Jingyuan, et al. "Solution-processable carbon nanoelectrodes for single-molecule investigations." Journal of the American Chemical Society 138.9 (2016): 2905-2908.

[4] Jia, Chuancheng, and Xuefeng Guo. "Molecule–electrode interfaces in molecular electronic devices." Chemical Society Reviews 42.13 (2013): 5642-5660.

[5] Iijima, S. Helical microtubules of graphitic carbon. Nature, (1991), 354(6348), 56.

[6] Slater, John C., and George F. Koster. "Simplified LCAO method for the periodic potential problem." Physical Review 94.6 (1954): 1498.

[7] Xu, C. H., et al. "A transferable tight-binding potential for carbon." Journal of Physics: Condensed Matter 4.28 (1992): 6047.

[8] C. J. Lambert , Basic concepts of quantum interference and electron transport in single-molecule electronics, Cite this: Chem. Soc. Rev., 2015, 44, 875.

[9] Soler, J. M. et al. The SIESTA method for ab initio order- N materials simulation. J. Phys. Condens. Matter 14, 2745 (2002).

[10] Langreth, D. C. & Perdew, J. P. Exchange-correlation energy of a metallic surface: Wave-vector analysis. Phys. Rev. B 15, 2884–2901 (1977).

[11] Ferrer, J. et al. GOLLUM: a next-generation simulation tool for electron, thermal and spin transport. New J. Phys. 16, 093029 (2014).

[12] Aviram, A. and Ratner. 1974 Molecular rectifiers Chem. Phys. Lett., 29 277

[13] Metzger, R. M., Chen, B., Hopfner, U., Lakshmikantham, M. V., Vuillaume, D., Kawai, T., X. Wu, Tachibana, H., T. V. Hughes, T. V., Sakurai, H., Baldwin, J. W.,

Hosch, C., Cava,M. P. , Brehmer, L., Ashwell, G. J. 1997 Unimolecular electrical rectification in hexadecylquinolinium tricyanoquinodimethanide J. Am. Chem. Soc. 119, 10455.

[14] Metzger, R. M. 2003 Unimolecular electrical rectifiers Chem. Rev. 103 3803

[15] Kushmerick, J., Holt, D., Yang, J., Naciri, J., Moore, M. and Shashidhar, R. 2002 Metal-molecule contacts and charge transport across monomolecular layers: Measurement and theory Phys. Rev. Lett. 89 086802.

[16] Guedon, C. M., Valkenier, H., Markussen, T., Thygesen, K. S., Hummelen, J. C. and van der Molen, S. J. 2012 Observation of quantum interference in molecular charge transport Nature Nanotech. 7 305.

[17] Ashwell, G. J., and Mohib, A. 2005 Improved molecular rectification from self-assembled monolayers of a sterically hindered dye J. Am. Chem. Soc. 127 16238.

[18] Nijhuis, C. A., Reus, W. F., Barber, J., Dickey, M. D. and Whitesides, G. M. 2010 Charge transport and rectification in arrays of SAM-based tunnelling junctions. Nano Lett. 10 3611.

[19] Nerngchamnong, N., Yuan, L., Qi, D. C., Li, J., Thompson, D., and Nijhuis, C. A. 2013, The role of van der Waals forces in the performance of molecular diodes. Nature Nanotech. 8 113.

[20] Elbing, M., Ochs, R., Koentopp, M., Fischer, M., von Hanisch, C., Weigend, F., Evers, F., Weber, H. B. and Mayor, M. 2005 A single-molecule diode Proc. Natl. Acad. Sci. U.S.A. 102 8815.

[21] Diez-Perez, I., Hihath, J., Lee, Y., Yu, L., Adamska, L., Kozhushner, M. A., Oleynik, I. I. and Tao, N.J. 2009 Rectification and stability of a single-molecule diode with controlled orientation. Nat. Chem. 1 635.

[22] Lortscher, E., Gotsmann, B., Lee, Y., Yu, L. P., Rettner, C. and Riel, H. 2012 Transport properties of a single-molecule diode. ACS Nano 6 4931.

[23] Batra, A., Darancet, P., Chen, Q., Meisner, J. S., Widawsky, J. R., Neaton, J. B., Nuckolls, C. and Venkataraman, L. 2014 Tuning rectification in single-molecular diodes. Nano Lett. 13 6233.

[24] Xiang, Limin, et al. Non-exponential Length Dependence of Conductance in Iodide-Terminated Oligothiophene Single-Molecule Tunneling Junctions. Journal of the American Chemical Society 138.2 (2016): 679-687.

[25] Zhu, Jingyuan, et al. Solution-Processable Carbon Nanoelectrodes for Single-Molecule Investigations. Journal of the American Chemical Society 138.9 (2016): 2905-2908.

[26] Venkataraman, Latha, et al. Dependence of single-molecule junction conductance on molecular conformation. Nature 442.7105 (2006): 904-907.

[27] Trasobares, Jorge, et al. "A 17 [thinsp] GHz molecular rectifier." Nature communications 7 (2016).

[28] Nerngchamnong, Nisachol, et al. "The role of van der Waals forces in the performance of molecular diodes." Nature nanotechnology 8.2 (2013): 113-118.

[29] Jeong, Hyunhak, et al. "Redox-Induced Asymmetric Electrical Characteristics of Ferrocene-Alkanethiolate Molecular Devices on Rigid and Flexible Substrates." Advanced Functional Materials 24.17 (2014): 2472-2480.

[30] Nijhuis, Christian A., William F. Reus, and George M. Whitesides. "Mechanism of rectification in tunneling junctions based on molecules with asymmetric potential drops." Journal of the American Chemical Society 132.51 (2010): 18386-18401.

Chapter 6

A comprehensive study of the electrical conductivity through flat stacked polycyclic aromatic hydrocarbons.

6.1 Introduction

Vertical devices, like the example shown in Fig 6.1a, which has a top contact deposited onto a self-assembled monolayer (SAM) formed on a metallic bottom contact are being studied experimentally with a view to developing this flat-stacked geometry as a tool to construct molecular electronic devices which will be scalable to industrial applications. An example of such a structure is a transparent top contact of graphene oxide is deposited onto a photo sensitive monolayer [1]. A more pertinent study [2] arranges π stacked aromatics within columnar coordination cages to obtain conductance measurements. In this work the SAM is made of polycyclic aromatic hydrocarbons (PAHs) and the electrical conductance is perpendicular to the plane (CPP) of the PAH attached to the electrodes is calculated as shown in figure 6.1a. Earlier work [3] focused upon the conductance in the plane (CIP), where the transport direction is from the bottom to the top contact, and in all cases, both experimental and theoretical the HOMO-LUMO gap is in the order of several electron volts. This work predicts that the through plane conductance is dependent upon the number of aromatic rings for the oligoacenes, where anthracene is semi-conducting, but tetracene is a conductor. In the case of PAHs the chemical structure plays an important role as structures above nine aromatic rings are predicted to have a high metallic conductance. These structures that will form the basis of this theoretical study are illustrated in Figure 6.2. The Fujita group has applied columnar coordination cages to efficiently and precisely assemble stacked π systems [4], and Takahashi group has measured the conductance for π -stacked aromatics figure 6.1b, where the π stack was sequentially increased from four to six stacked aromatic molecules and they show that the conductance decreases with the increasing number of π systems [5].

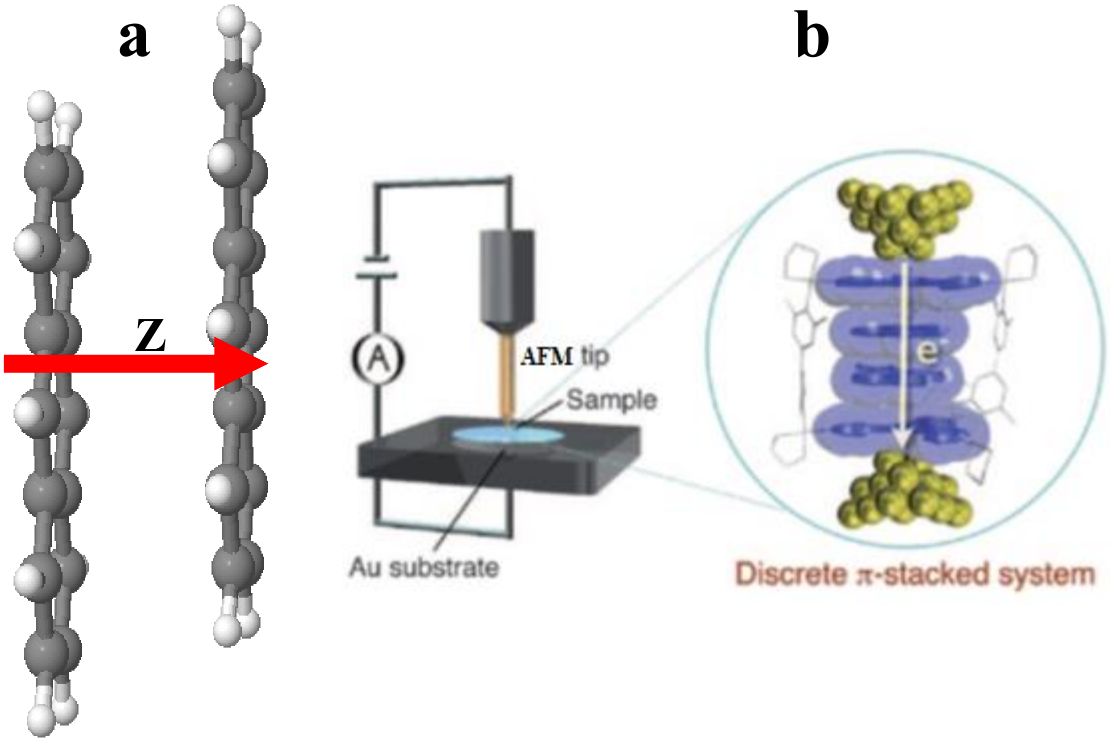

Figure 6.1. a- shows the orientation and model set-up for the electron transport calculations. In this case an infinite periodic chain of anthracene molecules are $\pi - \pi$ stacked at a separation of 0.22 nm, b- The experimental setup for the conductance measurement for pyrene $\pi - \pi$ stacked[5].

In this work I specifically focus on the electronic properties of π-π stacked aromatic systems, which are mainly determined by the π-π interaction in conjunction with charge transfer between the layers via electron donor/acceptors. Different types and size of molecules are presented in this chapter with varying surface patterning and bandgap energy. This π-π stacked system can be used as an electrode attached to a single molecule to replace the typical gold electrode in the case of a metallic system.

To calculate the electrical conductance through these stacks of molecules I assume a band transport model through an infinite stacked column of each PAH. For each structure, I evaluate the number of open channels as a function of the electron energy E passing through. This method is evaluated using two approaches. First, by obtaining the DFT Hamiltonian from SIESTA [6] and then applying equilibrium transport theory via Gollum [8] and secondly by constructing a tight binding nearest neighbor Hamiltonian from parameters for the hopping elements obtained from the band structures given by the DFT calculations.

6.2 Computational Details

The DFT calculations were carried out using the density functional package SIESTA [6] using the local density functional approximation (LDA) parameterised by the functional of Ceperley and Alder [7]. The systems were optimised to a force tolerance of less than 40 meV/Å using extended double zeta polarised basis sets of pseudo atomic orbitals with a real space grid defined with a plane wave cut off of 250 Ry. The electrical transport properties of the nanoscale system were calculated using Gollum [8] from the converged mean-field DFT Hamiltonian provided by SIESTA. Gollum is based upon equilibrium transport theory and is used to calculate the transmission coefficients T(E) and number of open channel for electrons of energy. Gas-phase optimizations were performed with the Gaussian 09 program package [9]. Using the B3LYP functional [10] and 6-31G**basis set. I have performed two types of DFT calculation by using LDA and VDW functionals and table 6.1 shows the energy gap and distance between the layer of dimer for both LDA and VDW methods for each molecule. As we can see the LDA energy gap is higher than VDW energy gap. This former is close to the experimental energy gap therefore I choose to use LDA functional.

Table 6.1 Shows the compared between LDA and VDW functional for isolated dimer system where Eg is the band gap, where D is the distance between two layers .

	LDA	VDW		D(A) LDA	D(A) VDW DZP	D(A) VDW Fix
		DZP	Fix			
	Eg	Eg	Eg			
Benzene	-4.61	-4.72	-4.55	3.30	3.4	3.45
Azulene	-1.92	-1.77	-1.74	3.20	3.33	3.44
Naphthalene	-3.19	-3.14	-3.05	3.25	3.33	3.44
Anthracene	-2.11	-2.0	-2.04	3.22	3.33	3.44
Tetracene	-1.44	-1.33	-1.39	3.20	3.30	3.44
Pyrene	-2.34	-2.28	-2.35	3.25	3.35	3.44
Anthanthrene	-1.62	-1.57	-1.63	3.20	3.35	3.44
Dibenzo coronene	-0.98	-1.08	-1.15	3.20	3.30	3.44

As an example of the model oligoacene structures used in the transport calculations Fig. 6.1 illustrates a section of the infinite $\pi - \pi$ stacked anthracene PAH chain. The direction of electron transport is illustrated by the arrow and is perpendicular to the plane of the PAH.

An important point to highlight is that the electron transport is now mediated through the $\pi - \pi$ interactions between the PAH layers and this results in an ordering of the size of the gap with the smallest PAH having the largest gap. Table 6.2 presents the results of the through plane electronic properties of the PAHs studied.

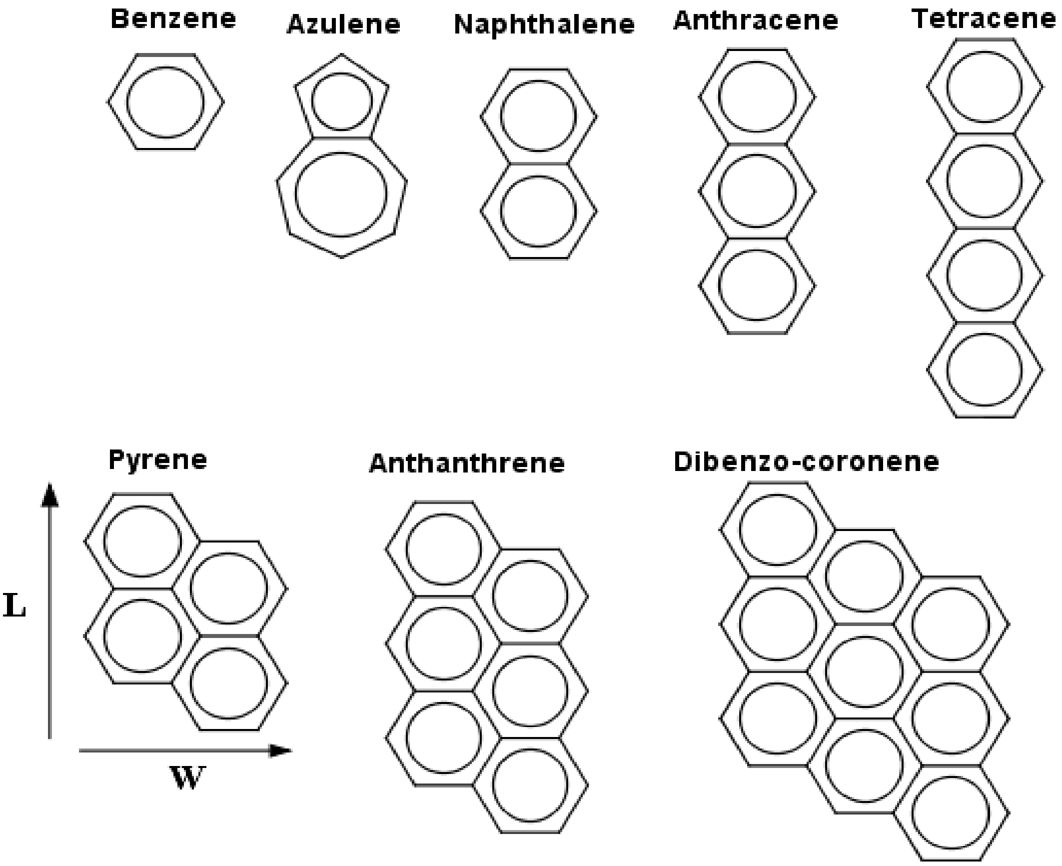

Figure 6.2. Shows the geometries of molecular where L and W denoted to the length and width of each molecule respectively.

6.3 Result

6.3.1 Number of open transmission channels

The number of open transmission channels for the systems shown in figure 6.2 are illustrated in figures 6.3 and 6.4. As we can see from those figures there is agreement between simple tight binding calculation (red line), which I will discuss later, and density function theory calculations (black line).

The first thing to note from these calculation, is that the band gap is decreasing with increase in the size of the molecule as shown more clearly in table 6.2. To define the size of the molecule, I introduce two parameters L and W, to denote the length and width. In the case of benzene which is 1 ring, L=1 and W=1, for naphthalene L=2 and W=1 etc. The band gap for the benzene molecule is 3.25 eV and this value decreases to 1.51 and 0.42 for Naphthalene (L=2,W=1) and Anthracene (L=3,W=1) respectively and the band gap disappears for Tetracene (L=4,W=1). While the same thing occurs for an increase in the width of the molecule. Anthracene (L=3, W=1) band gap = 0.42 eV, Anthanthrene (L=3,W=2) =0.18 eV and Dibenzocoronene (L=3, W=3) band gap = 0eV.

The symmetry and structure of the molecule also have a strong effect on the band gap, e.g. Azulene and Naphthalene have the same number of atoms (10) but there is a significant difference in their structure. This leads to big difference in the band gap as shown in the table 6.2 since the gap of Azulene is 0.39 eV this value is less than third of the naphthalene value.

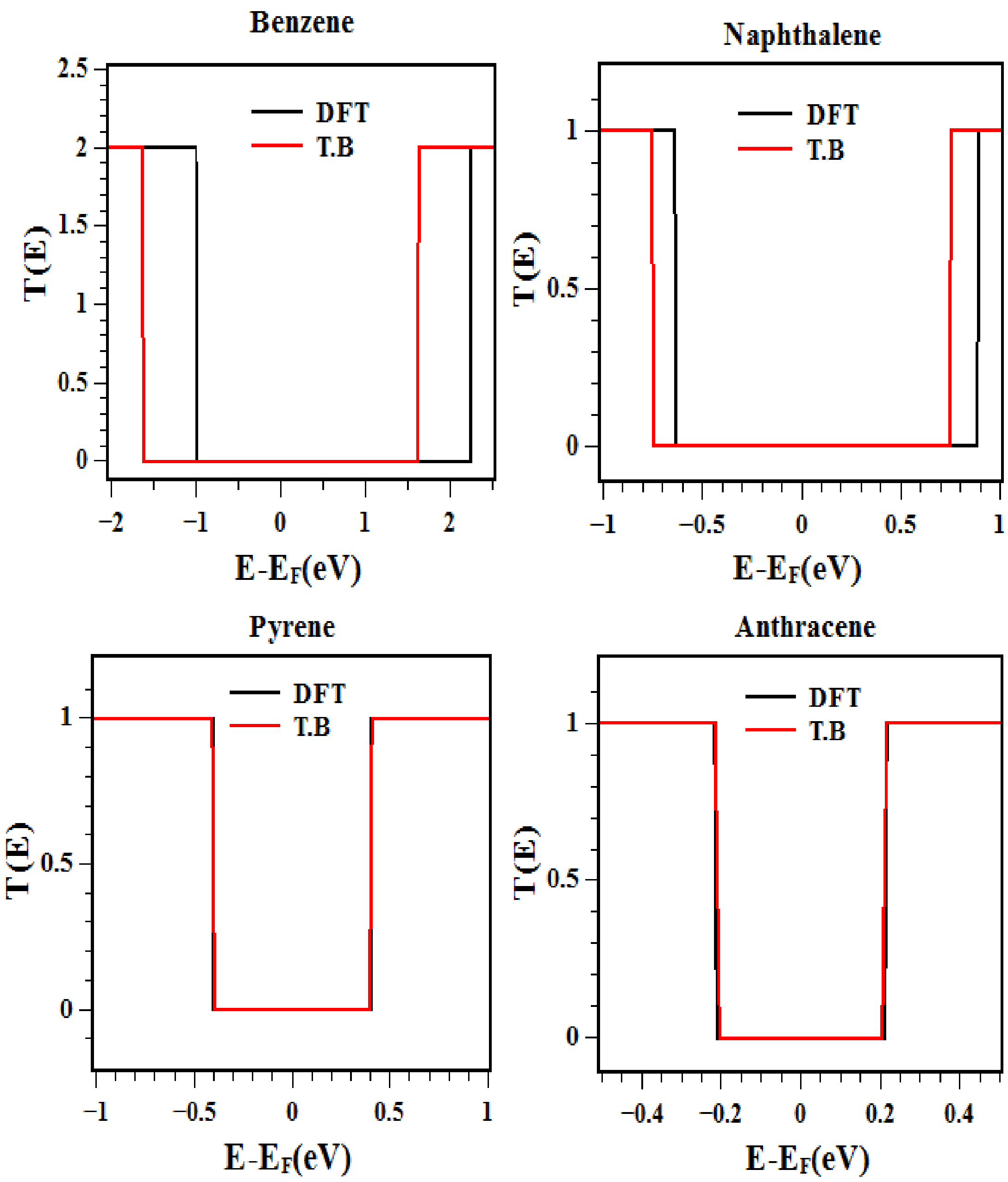

Figure 6.3. Show the number of open channel of the series of molecules, Benzene, Naphthalene, Pyrene and Anthracene.

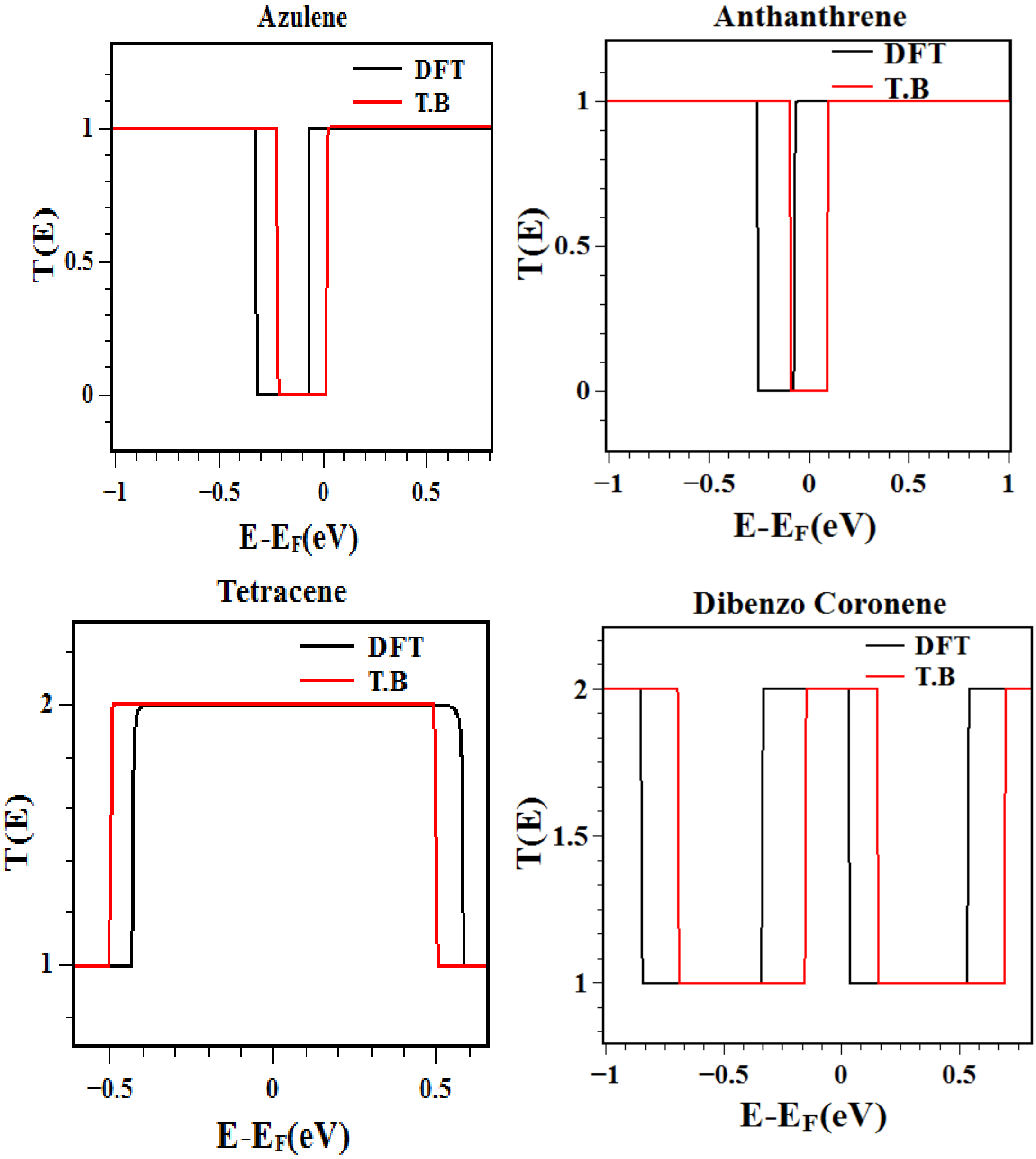

Figure 6.4 Show the number of open channel of the molecules Anthracene, Tetracene, Anthanthrene and Dibenzo coronene.

Table 6.2 shows the value of band gap for molecules in figure 6.2. The first two column are compared between T.B and DFT calculation for periodic system, and the next three column are compared between different ways for isolated monomer system.

	gap for periodic system		Gap for Isolated system		
Molecules	T.B	DFT (eV)	Exp.(eV)	DFT-B3LYP(eV)	DFT LDA(eV)
Benzene	3.24	3.25	6.2[12]	6.69	5.32
Naphthalene	1.49	1.51	4.51[12]	4.87	3.35
Pyrene	0.78	0.78	3.56[13]	3.89	2.55
Anthracene	0.41	0.42	3.31[12]	3.56	2.23
Azulene	0.4	0.39	2.48[14]	3.40	2.11
Anthanthrene	0.174	0.18	2.83[16]	2.88	1.84
Tetracene	---	---	2.49[15]	2.50	1.42
Dibenzocoronene	---	---		2.17	1.35

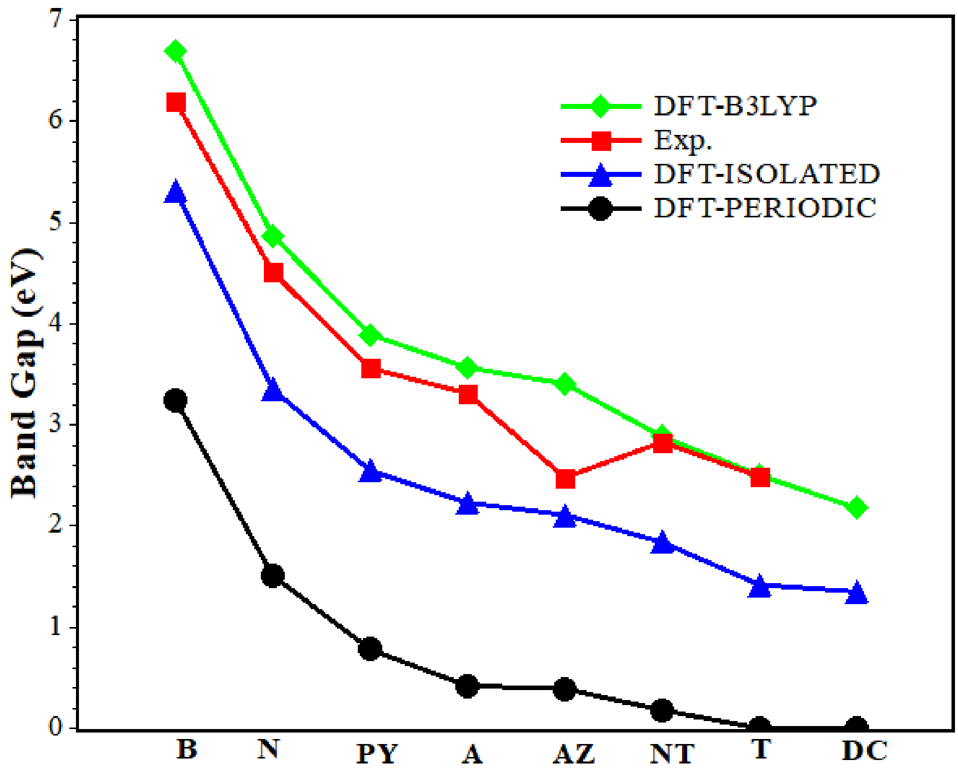

Figure 6.5 Show the comparison between different way DFT calculation and Experimental measurement

The last three columns of table 6.2 shows the comparison between the experimental and theoretical value for isolated molecules as we can see in the figure 6.5 the trend of band gap of the isolated molecules are same trend for periodic system but it is different in the value whereas the isolated system have band gap higher then periodic system.

6.3.2 Band Structure

Band structure calculation for transport perpendicular to the planes of the above columnar wires are shown in figure 6.6 and 6.7. where K is the wave vectors.

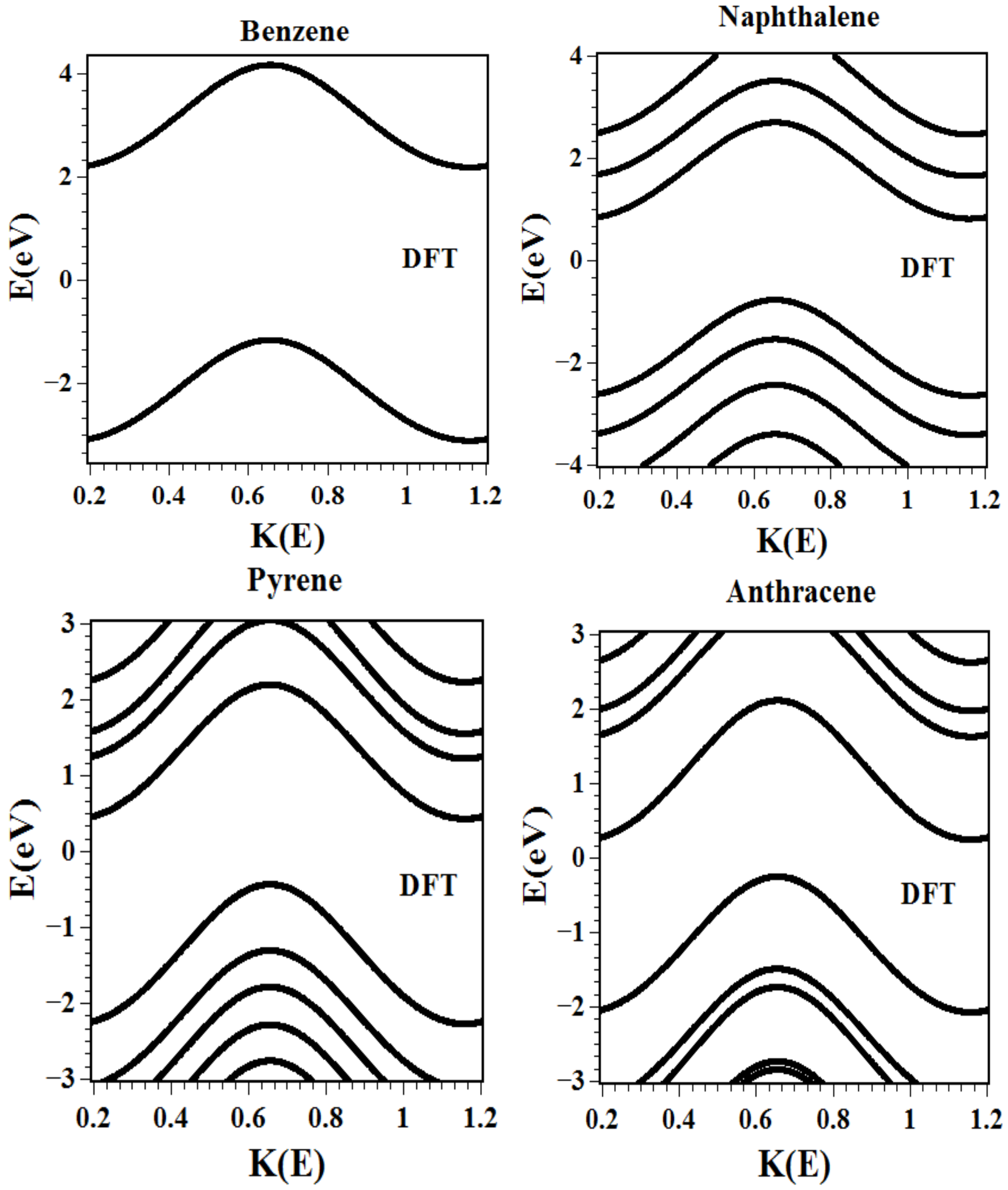

Figure 6.6. Show the series of molecule in the figure 6.2 Benzene, Naphthalene, Pyrene and Anthracene.

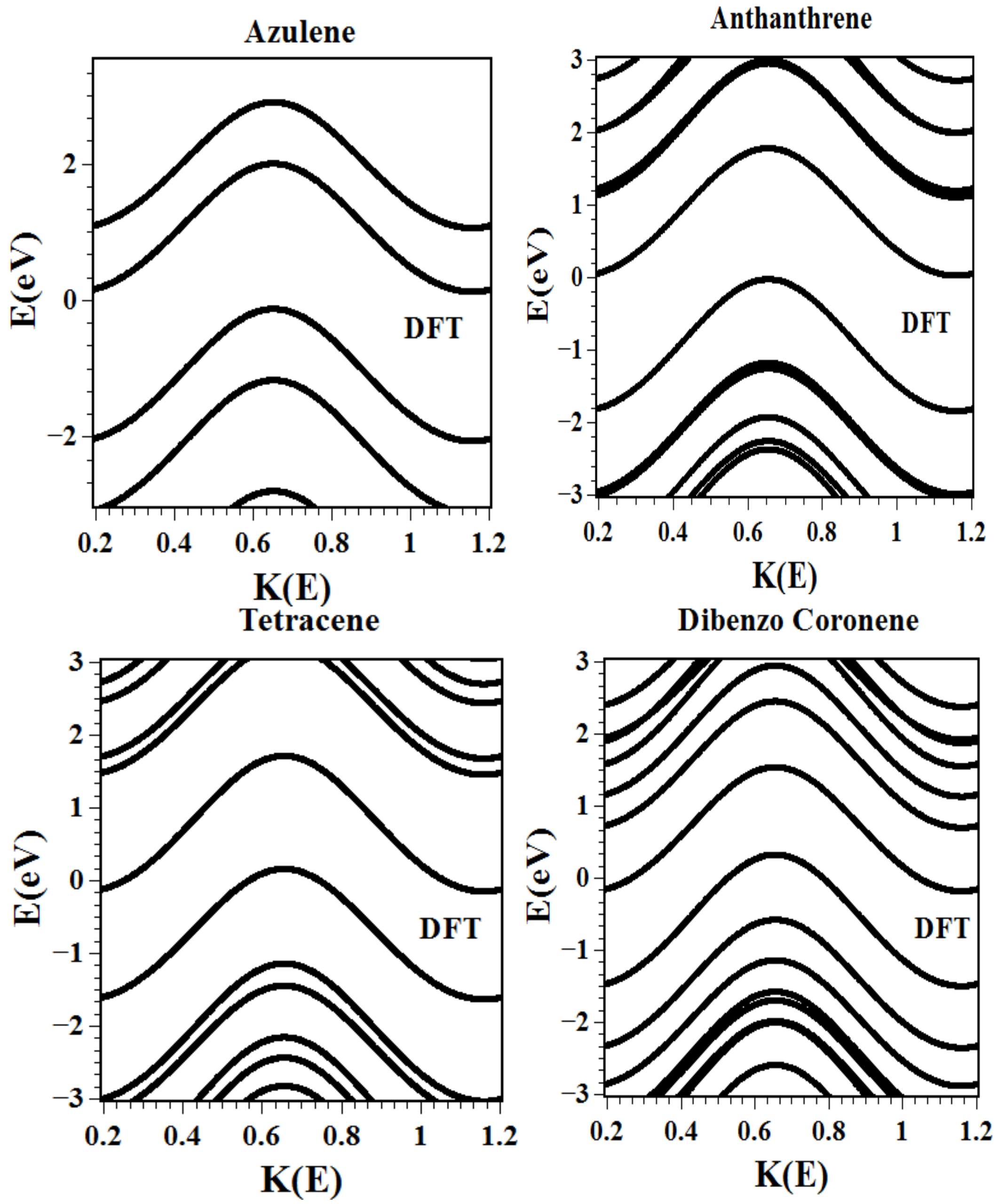

Figure 6.7 Show the band structure of the series of molecule in the figure 6.2 Azulene, Tetracene, Anthanthrene and Dibenzo coronene.

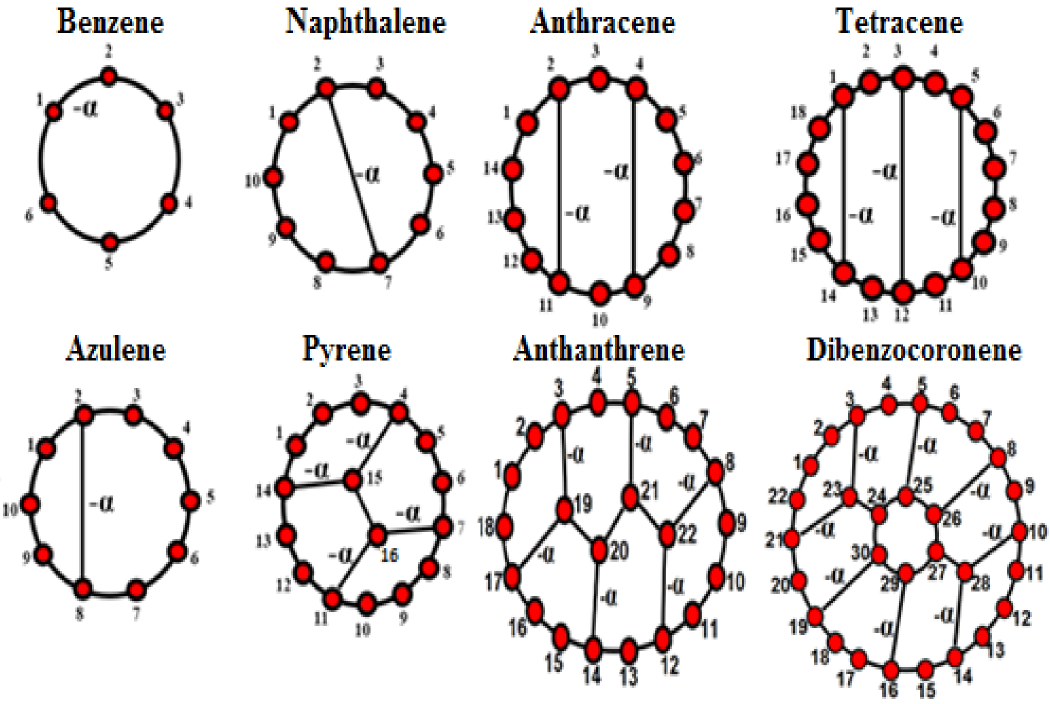
Benzene

Naphthalene

Anthracene

Tetracene

Azulene

Pyrene

Anthanthrene

Dibenzocoronene

Figure 6.8 Tight binding representation of the systems in figure 6.1 .

6.3.3 Eigenvalues

In order to understand the behavior of each molecular wire in this work, I have constructed a tight binding model for the isolated molecules shown in figure 6.2. As all molecules contain only carbon and hydrogen atoms I construct model of π – orbitals only by setting all couplings between carbons equal to -1 and set the on-site energy $\varepsilon_o=0$. This means that from the point of view of connectivity, the molecules in figure 6.2 are equivalent to the lattices shown in figure 6.8. The eigenvalues of the latter are presented in figure 6.9, from which the energy of the HOMO (E_H) and LUMO (E_L) are calculated, along with their difference $\Delta = E_L - E_H$ these are presented in table 6.3.

Table 6.3 the parameter using in tight binding calculation, where is γ coupling between C-C atoms in isolated molecular, τ' coupling between the layers and Δ Homo Lumo gap for isolated system.

Molecule	γ	$\acute{\tau}$	$\tau = \acute{\tau}/\gamma$	$4 \times \tau$	$\Delta = E_H - E_L$	$\Delta/4\tau$
Benzene	2.3	0.34	0.14	0.60	2	3.38
Naphthalene	2.12	0.28	0.13	0.52	1.23	2.34
Pyrene	1.9	0.22	0.11	0.46	0.89	1.92
Anthracene	2.23	0.36	0.16	0.64	0.82	1.28
Anthanthrene	2.39	0.3	0.12	0.50	0.58	1.16
Tetracene	2.45	0.61	0.24	0.99	0.59	0.59
Dibenzo coronene	2.4	0.3	0.12	0.50	0.37	0.74

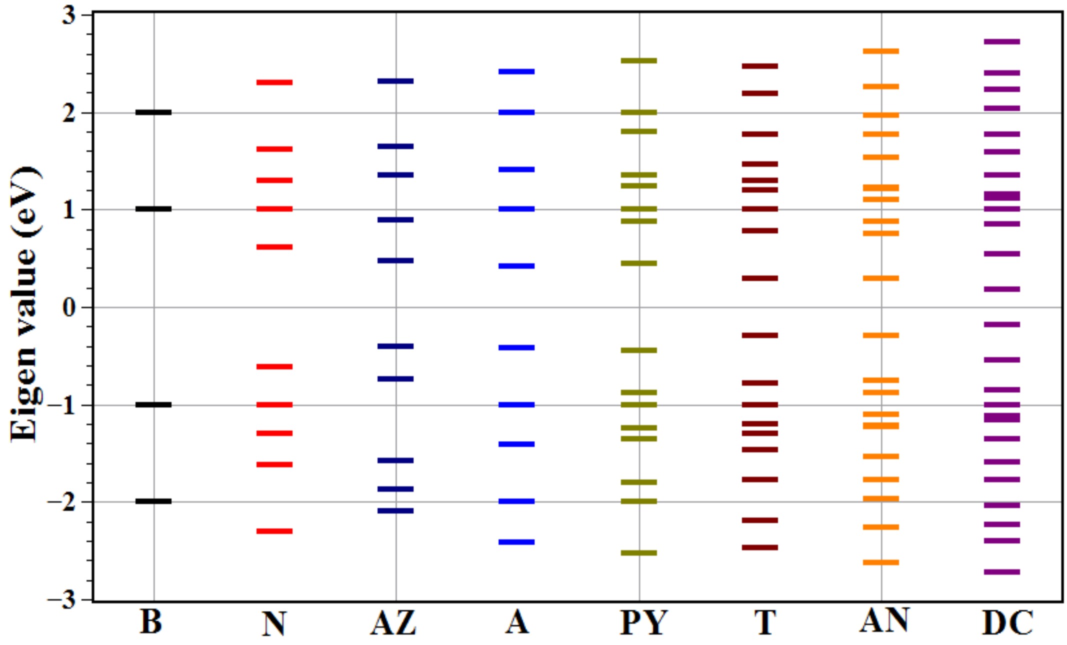

Figure 6.9 Tight binding eigenvalues of benzene (B), Naphthalene (N), Azulene(AZ), Anthracene(A), Pyrene(PY), Tetracene(T), Anthanthrene(AN) and Dibenzocoronene(DC). The tight binding Hamiltonian of each molecule was fixed with α=-1 and ε_o= 0.

For more clarity of these energy levels, it is useful to divide each structure in figure 6.8 , into two parts. The outside part (a ring) and the inside core, joined together by the coupling α as shown in Figure 6.8. Figure 6.10 and 6.11 show the eigenvalues for different values of α, with all other coupling fixed at -1 and ε_o=0 as mentioned above.

The evaluation of the eigenvalues can be understood by initial sitting α=0 and considering how they evolve toward $\alpha = \infty$.When α=0 all molecules become an isolated ring, where the eigenvalues can be calculated by the following equation

$$\varepsilon_{(n)} = \varepsilon_{O} - 2\gamma \cos\left(\frac{2\pi n}{N}\right) \quad where\, n = 1, \mp 2, \mp 3, \dots . N$$

Furthermore in some cases, such as pyrene, anthanthrene and dibenzocoronene, there are additional eigenvalues due to the isolated core. For the naphthalene molecule when α goes to infinity the atoms 2 and 7 are decoupled with others and for a dimer with bonding and anti-bonding levels at $\pm\infty$ in these limit, the remaining two groups of atoms (3,4,5,6) and (8,9,10,1) become a four atom chains whose eigenvalues do not depend on the value of α. Furthermore, for $\alpha = \infty$ there are individual atoms for instance in the Anthracene (3,10) and Tetracene (2,4,11,13) and these atoms cause vanishing eigenvalues.

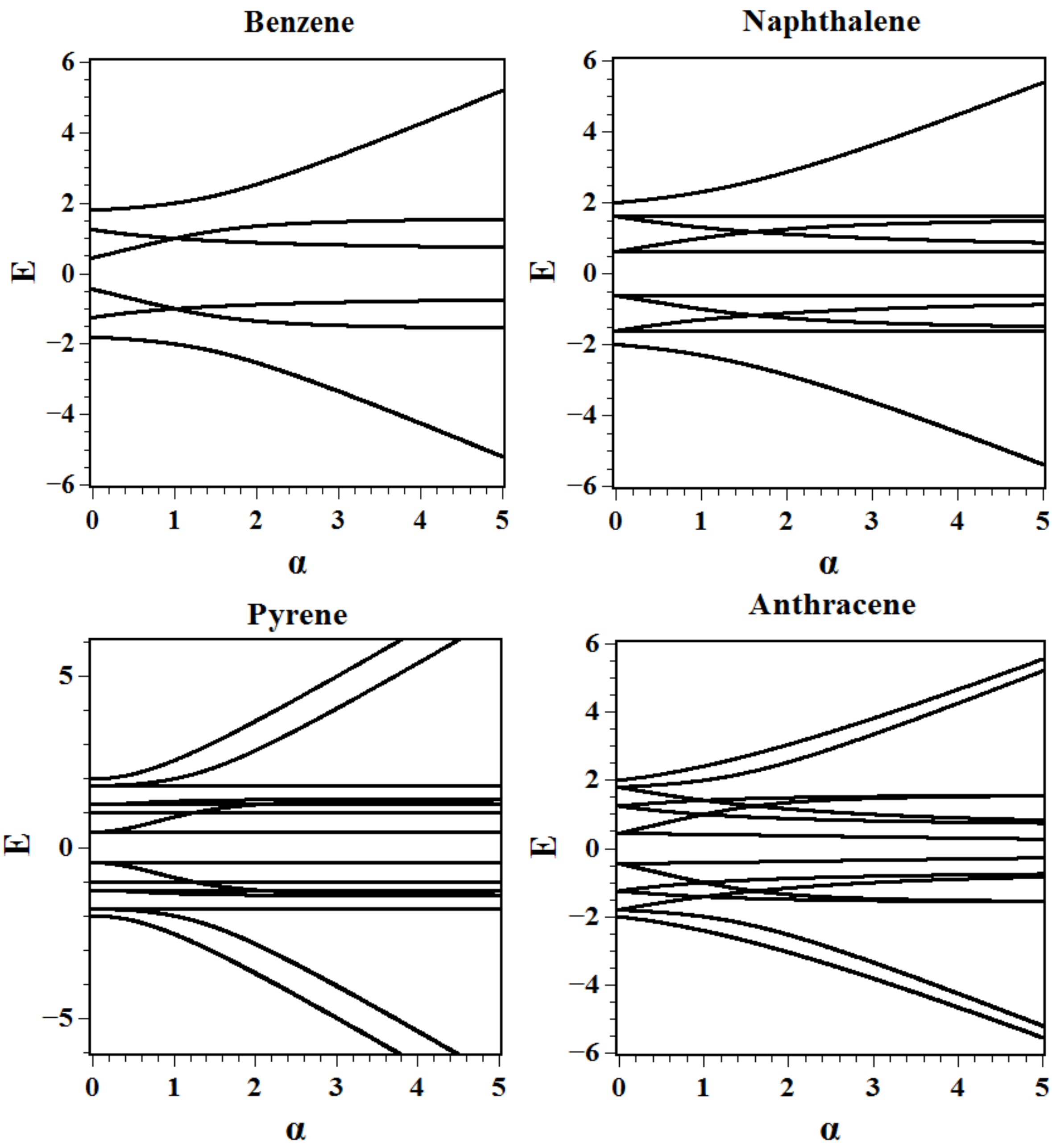

Figure 6.10 the Eigen value vs. α for Benzene, Naphthalene, Pyrene, and Anthracene

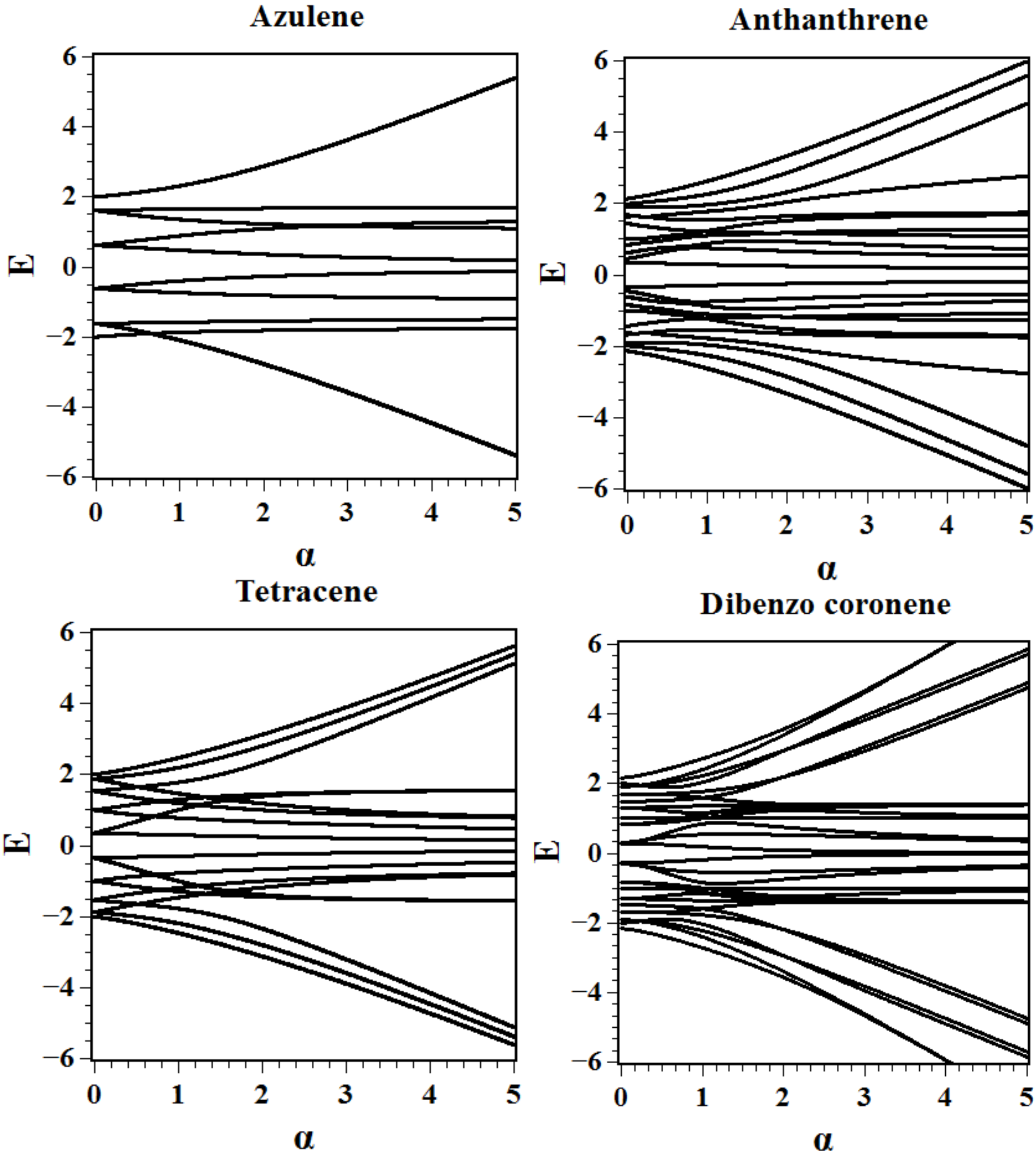

Figure 6.11 Eigen value vs. α for Azulene, Anthanthrene, Tetracene and Dibenzo coronene.

6.4 Analytical formula

When the above planar molecules are stacked in a column as in figure 6.12, with inter molecular couplings τ, each eigenvalue E_n of the isolated molecule form a band with dispersion relation.

$$E = E_n - 2\tau\cos(k)$$

Hence the energy gap between the HOMO band and the LUMO band is $(E_L - 2\tau) - (E_H + 2\tau) = \Delta - 4\tau$ which vanish when $\Delta/4\tau \leq 1$

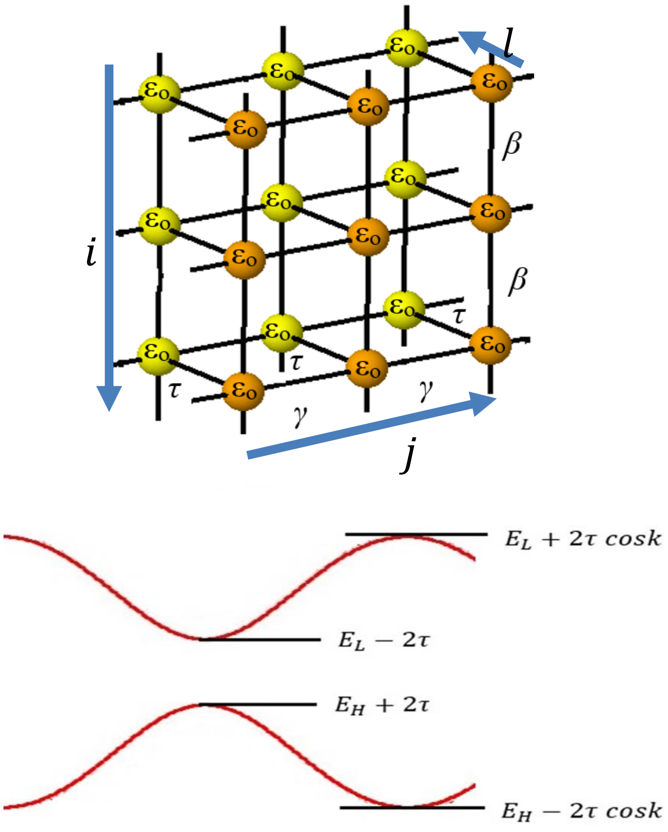

Figure 6.12 Three dimension chain, one more layer add to the 2d dimension system with l labelled and τ is the coupling between the layers.

The last column in the table 6.3 shows the values of $\Delta/4\tau$ which are less than 1 for tetracene and dibenzocoronene. All other molecular wires are semiconductors or isolators.

Conclusion

The calculations predict that by careful selection of larger pi stacked PAHs conducting wires could be prepared. The electrical properties of these wires would depend upon the details of the PAH construction where for example Pyrene would be semi-conducting but dibenzocoronene would be conducting. Furthermore from analytical formula can predict the system whether conductor or semiconductors dependent on the ratio of $\Delta/4\tau$, if it is less than one the system conductor otherwise semi-conductors.

References

[1]. Li, Tao, et al. "Ultrathin Reduced Graphene Oxide Films as Transparent Top-Contacts for Light Switchable Solid-State Molecular Junctions." *Advanced Materials* 25.30 (2013): 4164-4170

[2]. Malloci, G., et al. "Electronic and optical properties of families of polycyclic aromatic hydrocarbons: A systematic (time-dependent) density functional theory study." Chemical Physics 384.1 (2011): 19-27.

[3]. Karamitaheri, Hossein, et al. "Atomistic study of the lattice thermal conductivity of rough graphene nanoribbons." IEEE Transactions on Electron Devices 60.7 (2013): 2142-2147.

[4] Yamauchi, Yoshihiro, et al. "Engineering double to quintuple stacks of a polarized aromatic in confined cavities." Journal of the American Chemical Society 132.3 (2009): 960-966.

[5] Kiguchi, Manabu, et al. "Electron Transport through Single Molecules Comprising Aromatic Stacks Enclosed in Self-Assembled Cages." Angewandte Chemie 123.25 (2011): 5826-5829.

[6]. Soler, José M., et al. "The SIESTA method for ab initio order-N materials simulation." Journal of Physics: Condensed Matter 14.11 (2002): 2745.

[7]. Ceperley, David M., and B. J. Alder. "Ground state of the electron gas by a stochastic method." Physical Review Letters 45.7 (1980): 566.

[8]. Ferrer, Jaime, et al. "GOLLUM: a next-generation simulation tool for electron, thermal and spin transport." New Journal of Physics 16.9 (2014): 093029.

[9]. Frisch, M. J., et al. "Gaussian 09, Revision A, Gaussian." Inc., Wallingford CT (2009).

[10]. Stephens, P. J., et al. "Ab initio calculation of vibrational absorption and circular dichroism spectra using density functional force fields." The Journal of Physical Chemistry 98.45 (1994): 11623-11627.

[11]. Lambert, C. J. "Basic concepts of quantum interference and electron transport in single-molecule electronics." Chemical Society Reviews 44.4 (2015): 875-888.

[12]. Musa, A., et al. "Effects of delocalised π-electrons around the linear acenes ring (n= 1 to 7): an electronic properties through DFT and quantum chemical descriptors." Molecular Physics 113.11 (2015): 1347-1358.

[13]. Nayak, Pabitra K. "Exciton binding energy in small organic conjugated molecule." Synthetic Metals 174 (2013): 42-45.

[14]. Lete, Cecilia, Bhushan Gadgil, and Carita Kvarnström. "The electrochemistry of copolymer films based on azulene and 3 thiophene acetic acid." Journal of Electroanalytical Chemistry 742 (2015): 30-36.

[15]. Yin, Jun, et al. "Synthesis of functionalized tetracene dicarboxylic imides." Tetrahedron Letters 51.48 (2010): 6313-6315.

[16]. Shah, Bipin K., et al. "Photophysical properties of anthanthrene-based tunable blue emitters." The Journal of Physical Chemistry A 109.34 (2005): 7677-7681.

Chapter 7

7.1 Conclusion

The electric properties of different molecular devices have been studied in this thesis using density functional theory and the Green's function scattering formalism which are described in chapter 2 and 3 respectively.

In the chapter 4 I studied the single-molecule conductance of ten oligo (arylene-ethynylene) derivatives with five different core units (dibenzothiophene, carbazole, dibenzofuran, fluorene and biphenyl) attached to gold electrodes by pyridyl anchoring groups. Within the two series there is either para-para or meta-meta conjugation through the core unit. In all cases molecules with para connectivity present larger conductances than their meta isomers, regardless of the bridging unit. I have observed clear and distinct trends in the para and meta series. In the para series there is a clear correlation between aromaticity of the central ring and the single-molecule conductance values in the sequence dibenzofuran > carbazole > dibenzothiophene, in agreement with a previous experimental study on monocyclic core units (furan > thiophene). However, in the meta series the carbazole derivative is the most conductive: the sequence dibenzothiophene ≈ dibenzofuran < carbazole. It is concluded that the nitrogen lone pair facilitates transmission through the molecule. Overall, I find that constructive quantum interference in the para-connected molecules persists in the presence of bridging atoms and is partly masked by the presence of sigma channels, whereas bridging atoms alleviate destructive quantum interference in the meta-connected molecules. Our comprehensive study establishes that both quantum interference and heteroaromaticity in the molecular core units play important and inter-related roles in determining the conductance of single molecular junctions. These results should assist in future research in the development of new molecules for incorporation into nanoscale molecular circuits. In the second part of this chapter I considered a set of molecules with fix bridge atoms and different side groups formed from, 2H, 2Me, 2OMe, 2MF3 or crown ethers. The electrical conductance and Seebeck coefficient were almost the same for these molecules.

In the chapter 5 I studied charge transport through asymmetric molecules attached to armchair carbon nanotube (5, 5). The goal of these studies is to calculate the I-V characteristic and rectification ratio. During this project I studied different types of CNT's some of them metallic and others is semimetal.

Despite the different structures of these two systems, the conductance ratio between M1 and M2 was close to 0.45, and the calculated beta value for different lengths of phenyl rings almost agreed.

Finally in chapter 6 the calculations predict that by careful selection of larger PAHs pi stacked conducting wires could be prepared. The electrical properties of these wires would depend on the size of the PAH construction, where for example wires formed from stacked benzene rings would be semi-conducting but tetracene would be conducting.

7.2 Future Work

In this thesis, I have concentrated on electron and thermal transport through single molecules attached to either gold or carbon nanotube leads. For the future it would of interest to include the contribution from phonons to thermoelectricty [1,2] and examine more exotic forms of transport such as molecular-scale transport of quasi-particles associated with superconducting leads [3], spin-dependent transport in the presence of ferromagnetic leads or more complex metals[4,5], combinations of superconducting and ferromagnetic leads [6,7] and even more exotic effects such as current-induced forces [8]. In practice, for such complex structures, it may not be possible to obtain simple analytic results. Nevertheless such problems could be investigated numerically, using quantum transport codes such as the multiple-scattering code Gollum [9].

References

[1]. Kambili, A., et al. "Phonon-mediated thermal conductance of mesoscopic wires with rough edges." Physical Review B 60.23 (1999): 15593.

[2]. Fagas, G., et al. "Lattice dynamics of a disordered solid-solid interface." Physical Review B 60.9 (1999): 6459.

[3].Hui, V. C., and C. J. Lambert. "Andreev scattering, universal conductance fluctuations and phase periodic transport." EPL (Europhysics Letters) 23.3 (1993): 203.

[4]. García-Suárez, V. M., et al. "Optimized basis sets for the collinear and non-collinear phases of iron." Journal of Physics: Condensed Matter 16.30 (2004): 5453.

[5]. García-Suárez, V. M., et al. "Single-channel conductance of H 2 molecules attached to platinum or palladium electrodes." Physical Review B 72.4 (2005): 045437.

[6].Fal'Ko, V. I., C. J. Lambert, and A. F. Volkov. "Andreev reflections and magnetoresistance in ferromagnet-superconductor mesoscopic structures." Journal of Experimental and Theoretical Physics Letters 69.7 (1999): 532-538.

[7].Taddei, F., et al. "Suppression of Giant Magnetoresistance by a superconducting contact." Physical review letters 82.24 (1999): 4938.

[8].Bailey, S. W. D., I. Amanatidis, and C. J. Lambert. "Carbon nanotube electron windmills: A novel design for nanomotors." Physical review letters 100.25 (2008): 256802.

[9].Ferrer, Jaime, et al. "GOLLUM: a next-generation simulation tool for electron, thermal and spin transport." New Journal of Physics 16.9 (2014): 093029.